SELECTIVE AREA GROWTH AND CHARACTERIZATION OF GAN BASED NANOSTRUCTURES BY METAL ORGANIC VAPOR PHASE EPITAXY

A Thesis
Presented to
The Academic Faculty

by

Wui Hean Goh

In Partial Fulfillment
of the Requirements for the Degree
Doctor of Philosophy in the
School of Electrical and Computer Engineering

Georgia Institute of Technology
May 2013

SELECTIVE AREA GROWTH AND CHARACTERIZATION OF GAN BASED NANOSTRUCTURES BY METAL ORGANIC VAPOR PHASE EPITAXY

Approved by:

Professor Paul Voss, Committee Chair
School of Electrical and Computer Engineering
Georgia Institute of Technology

Professor Jeff Davis
School of Electrical and Computer Engineering
Georgia Institute of Technology

Professor Abdallah Ougazzaden, Advisor
School of Electrical and Computer Engineering
Georgia Institute of Technology

Professor Mohammed Cherkaoui
School of Mechanical Engineering
Georgia Institute of Technology

Professor Ali Adibi
School of Electrical and Computer Engineering
Georgia Institute of Technology

Date Approved: 30 November 2012

To my family.

ACKNOWLEDGEMENTS

There are many people who have given me precious guidance for reaching this point of my research career. I would like to express my sincere gratitude to those who have helped make this work possible. First, I would like to thank my advisor, Professor Abdallah Ougazzaden, for his invaluable guidance, encouragement, and support. His endless knowledge and ability to relate many ideas together has made this work possible. I would like to express my appreciation for my dissertation reading committee for their guidance and feedback: Professor Ali Adibi and Professor Paul Voss.

I appreciate the great opportunity I had to enjoy with my friends and colleagues, Jerome, Mohamed, Vinod, Konstanstino, and Peter, in different aspects of life and research. I am deeply grateful to Simon, Tarik, Nabila and Gaelle for teaching me everything I know about experimental characterization and for their professional manners and research ethics. I would like to express my gratitude to all my colleagues in Georgia Tech: Renaud, Zheshen, Wei, Sarah, David, Jeramy, Ning, Youssef, Mohammad, Qing, Audric, and Fred for their friendship and for their help and support. I would especially like to thank Josayne for a fantastic job at administrative works.

I would also like to acknowledge the help from outside Georgia Tech who provided assistance in many ways. Specific thanks go to Dr. Sirenko for discussion in synchrotron-based X-ray diffraction results, Dr. Ould-Saad for characterization in micro Raman spectrometry, Dr. Martinez and Dr. Ramdane for mask fabrication and device processing, David and Ali for transmission electron microscopy sample preparation and Gilles for characterization in transmission electron microscopy.

Finally and most importantly, I would like to thank my family. Without their love and support I would not be here.

TABLE OF CONTENTS

DEDICATION . . . . . **iii**

ACKNOWLEDGEMENTS . . . . . **iv**

LIST OF TABLES . . . . . **viii**

LIST OF FIGURES . . . . . **ix**

I INTRODUCTION **1**

1.1 Group III-nitride semiconductor structure and characteristic 3

1.1.1 Structural properties 3

1.1.2 Electron bandstructure properties 4

1.2 Heteroepitaial GaN 7

1.2.1 Introduction 7

1.2.2 Lattice mismatch 8

1.2.3 Critical thickness 9

1.2.4 Coefficient of thermal expansion mismatch 10

1.2.5 Defects in the GaN heteroepitaxy 11

1.3 Reduction of the threading dislocation density by various growth techniques 13

1.3.1 Improved buffer layers with Si_xN_y interlayer 13

1.3.2 Selective area growth 14

1.3.3 Epitaxial lateral overgrowth 15

1.3.4 Nano selective area growth (approach chosen for our study) . 18

II GROWTH AND CHARACTERIZATION OF GAN **24**

2.1 Metalorganic vapor phase epitaxy 25

2.1.1 Home-made T-shaped MOVPE system 27

2.1.2 Reflectometer 29

2.2 Nomarski DIC microscope 31

2.3 Scanning electron microscope 32

2.4 Transmission electron microscope 34
2.5 Atomic force microscope 36
2.6 Synchrotron based X-ray diffraction 38
2.7 Cathodoluminescence 42

III MICRO SELECTIVE AREA GROWTH 44

3.1 Experimental procedures 44
3.2 Optimization of the growth condition 47
3.3 Study of growth rate enhancement 48
3.4 Model of selective area growth 50
3.5 Summary 52

IV NANO SELECTIVE AREA GROWTH 54

4.1 Nano selective area growth on GaN template 54
4.1.1 Experimental procedures 54
4.1.2 Growth and characterization of nanostructures 56
4.2 Nano selective area growth on highly lattice mismatched materials, nanoheteroepitaxy 58
4.2.1 Experimental procedures 59
4.2.2 GaN nanostructures on AlN template 59
4.2.3 GaN nanostructures on SiC 64
4.3 Analysis of strain relaxation in GaN nanostructures using submicron beam X-ray diffraction 69
4.3.1 Experimental procedures 70
4.3.2 Results and discussion 71
4.4 III-nitride nanodots, nanowires and multi quantum wells 75
4.4.1 Experimental procedures 76
4.4.2 Optical and structural properties of III-nitride nanodots, nanowires and multi quantum wells 77
4.5 Summary 82

V GROWTH AND FABRICATION OF III-NITRIDE LIGHT EMITTING DIODES 85

5.1 Introduction 85

5.2 Epitaxial Growth Development and Characterization 86

5.3 Light Emitting Diode Device Data 94

5.4 Summary 96

VI CONCLUSIONS AND FUTURE WORK 98

LIST OF TABLES

1 Lattice parameters of the group-III nitrides 5

2 Band structure parameters for wurtzite nitride binaries [1] 6

3 Physical properties of the potential substrates for GaN epitaxy 10

4 Properties of group III precursors 27

5 Parametric study of SAG on the width of the mask (Wm) and the width of the opening (Wo). 48

6 E_2 mode frequency and biaxial stress measured in GaN thin film grown in the nanostripe opening and on the planar SiC substrate at low and high growth pressure. 69

7 Growth conditions and measured strains for the samples. 71

LIST OF FIGURES

1 Crystal structures of III-nitrides (a) zinc blende and (b) wurtzite. . . 4

2 Bravais-Miller index of wurtzite GaN structure. 4

3 III-nitrides lattice parameter vs. bandgap energy. 5

4 Lattice mismatch between the substrate and the epilayer: a) the epilayer is in tension, $a_e < a_s$ and, b) the epilayer is in compression, $a_e > a_s$. 8

5 Misfit dislocations at the GaN/sapphire interface (figure reprinted from [5]). 11

6 Schematic diagram of GaN/sapphire subgrains with tilt and twist. . . 12

7 Unit cell of GaN with Burger vector of three types of dislocation: a type, c type, and $a + c$ type. 13

8 A cross-section TEM image showing dislocation reduction by SiN interlayer and AlGaN intermediate layers (figure reprinted from [9]). . . 14

9 Schematic of the SAG: left figure shows a substrate patterned with dielectric mask; right figure shows the diffusion of reactive species to the exposed area. 15

10 Selective area growth of GaN. After filling these openings, lateral growth starts and produces pyramids with {1-101} facets (figure reprinted from [16]). 16

11 Morphological changes in ELO GaN for different reactor pressures and growth temperatures (figure reprinted from [23]). 17

12 Schematic representation of the different stages of ELO: (a) a GaN template substrate, (b) dielectric mask is patterned on the GaN template, (c) one-step growth ELO, and (d) two-step growth ELO. 18

13 The difference of stress relaxation between (a) the conventional growth and (b) nano selective area growth. The epilayer grown by the conventional epitaxial growth can only relax in the vertical direction while the epilayer grown by NSAG can relax in both vertical and lateral direction. 19

14 Total strain energy stored in the system versus the thickness of the epilayer grown by (a) conventional growth and (b) nano selective area growth. 19

15 Illustration of the discontinuous boundary value problem for epitaxial growth occurs on seed pads with no adhesion of the film between the pads. The strain energy profile, $\omega(0,z)$, for the pad mid cross-section is shown on the left[24]. 21

16 Schematic illustration of GaN epitaxial growth. 26

17 Home-made T-shaped MOVPE system. 28

18 Simplified schematic of the gas panel used. 29

19 Principle of the reflectometry. 30

20 Influence of surface roughness on the intensity of reflected light: a) roughness increase, and b) smooth surface. 31

21 Schematic illustration of a Nomarski DIC microscope. 33

22 Schematic illustration of a SEM (figure reprinted from [32]). 34

23 Schematic illustration of a TEM (figure reprinted from [33]). 36

24 Schematic illustration of AFM. 38

25 X-ray diffraction at the Bragg angle. 40

26 Depth of penetration of the electron beam on GaN layer. 43

27 Process for micro mask preparation by optical lithography. 45

28 Optical images show the influences of growth condition of the selective area growth with (a) high growth rate and (b) low growth rate. . . . 46

29 Optical images of the micro-SAG on the GaN template with masks of different dimensions. 47

30 Morphological studies of GaN structure grown by SAG, (a) AFM micrograph, (b) height profile, and (c) surface scan of the top surface. . 49

31 The growth rate enhancement R is plotted against (a) the width of the mask, Wm, and (b) the width of the opening between the masks, Wo. 50

32 Schematic of the computational domain and boundaries conditions used in the three-dimensional dimensions VPD. 51

33 Cross-section normalized thickness profiles (measured and calculated) for two different mask patterns, (a) Wm = 140 μm, Wo = 40 μm, and (b) Wm = 120 μm, Wo = 60 μm. In both cases, D/k is set to 13 μm. 53

34 Process for nano mask preparation by e-beam lithography. 55

35 SEM image of the patterned mask on GaN template. 55

36 SEM image of GaN grown by NSAG (a) before removing the mask and (b) after removing the mask. 57

37 (a) SEM image of GaN nanodots grown by NSAG. (b) AFM image GaN nanodots after removing the mask. 58

38 AFM profile measurement of NSAG across the dielectric mask with (a) 200 nm nominal thickness and (b) 400 nm nominal thickness. 58

39 SEM images of the patterned mask on AlN/Al_2O_3 template (a) before and (b) after the growth of the GaN nanostructures. The dashed lines in (b) show the windows of the nanostripes that are filled by the GaN crystal. Inset shows the magnified view of the nanostripe structures with jagged sidewall. 60

40 AFM images of the lateral growth nanostripes: (a) plan view of the nanostripes with various crystallographic planes; (b) height profile measurement across the nanostripes in the horizontal direction (dashed line in Figure 39a) and (c) height profile measurement across the nanostripes in the vertical direction (solid line in Figure 39a). 61

41 SEM angle views of GaN nanodots array after removing the mask. The thicknesses of the GaN layer on the unpatterned area are (a) 200 nm and (b) 1000 nm. 62

42 AFM images of (a) a single nanodot structure and (b) height distribution profile of 16 nanodots grown by NSAG. The thickness of the unpatterned layer is 1000 nm. 63

43 Schematic diagram of a proposed growth evolution of the GaN nanodot. 64

44 (a) SEM image of the mask before growth; (b) SEM image of the nanostructures grown on SiC substrate at 100 Torr; (c) High magnification SEM angle view image of the nanostructures and the growth on the non-masked area; (d) SEM planar view image compares NSAG grown structures in the mask openings and the step bunching effect for GaN grown on the planar 6H-SiC substrate. 65

45 SEM images of GaN nanostructures on SiC substrate at (a) 100 Torr and (b) 450 Torr. 67

46 Raman spectra of GaN grown in the stripe opening and on the unpatterned are at 100 Torr (red) and 450 Torr (blue). The symbols are experimental obtained data while the lines are curve fit of the experimental results. 68

47 Experimental setup. Si(1 1 1) mono-silicon monochromator; BS-gold beam stop; PZP-phase zone plate; OSA-order sorting aperture; XFlash-fluorescence detector. 71

48 (a) SEM image of sample 3. (b) X-Y map of the diffracted intensity collected from the nanodots region. Background is subtracted and θ is optimized for the rightmost nanodot. (c) SEM image of sample 2. (d) AFM image of sample 1. 72

49 (a) Diffraction signal distribution for different positions on the field, nanodots, and ridges for the high-pressure sample 1. (b) The same measurements for the low-pressure sample 2. (c) Qualitative reconstruction of the planar tilting. Numbers (1-5) correspond to different segments of the experimental dependencies of the experimental χ signals in (a) and each describes a distinct continuum of planar tilting. . 74

50 (a) Iso-intensity surfaces at the level of 99.9% of the maximum intensity of the 3D signal distribution for the nanodots (green) and nanoridges (blue). Data represents an average for signal from all nanostructures of that type measured per sample. For the ridges, only signal from the untilted planes is considered. The Δq axes are relative to the 00.4 reciprocal lattice point of theoretical bulk GaN. (b) Iso-intensity surface at the level of 50% of the maximum intensity of the 3D signal distribution for a position on a nanoridge of sample 2. (i) is the main signal from the substrate-aligned (0 0 0 1) planes, and (ii) is the secondary signal from the tilted (0 0 0 1) planes. (c) The position on the nanoridges where the signal in (b) was collected. 75

51 SEM images of a hexagonal nano-pyramid and several <1 1 -2 0> oriented nano-ridges grown by NSAG. 78

52 (a) Cross-sectional bright field TEM image of AlGaN/GaN grown on a nano-ridge showing absence of threading dislocations in the nanostructure. (b) Cross-sectional HAADF TEM image near the nano-opening showing the growth evolution of the nanostructure by NSAG. 79

53 Cross-sectional HAADF TEM image of AlGaN/GaN layers grown on a nano-ridge showing sharp interfaces between the AlGaN and GaN epilayers and uniform growth. Inset shows a nanowire grown at the apex of a nano-ridge. The height and width of the nanowire is estimated to be 2.5 nm and 6 nm, respectively. 80

54 (10.5) reciprocal space mapping of a AlGaN nano-ridge structure grown by NSAG. The strong peak in the center of the map corresponds to the GaN substrate. The signal from AlGaN consists of a weaker layer peak (right above the GaN peak) and the thickness fringes. The incorporation of aluminum on the nanostructure has been estimated from the separation in reciprocal space between GaN and AlGaN peaks to be 5%. 81

55 (a) Cross-sectional HAADF TEM image of five-period InGaN/GaN MQWs grown on a semi-polar facet of the nano-pyramid. No clear evidence of quantum dots is observed at the top of the nano-pyramid. (b) Cross-sectional HAADF TEM image of InGaN/GaN MQWs showing change of growth facet close to the top of the nano-ridge. Inset shows the place where the intersection occurs. EDX analysis shows higher indium mole fraction at the intersection of the growth facets compared to the average value for the MQWs. 82

56 Room temperature CL spectra of InGaN/GaN MQWs grown on the nano-ridges and on the unpatterned area. The InGaN MQWs grown on the nanostructure show higher CL intensity and ∼14 nm blueshift of luminescence peak wavelength from the MQWs grown on the unpatterned area. 83

57 Epitaxial structure of a *p-i-n* GaN-based light emitting diode (control LED). 86

58 Epitaxial structure of a *p-i-n* GaN-based nano-diode. 87

59 *In-situ* reflectance measurement during *p-i-n* GaN based LED growth on GaN template. 88

60 (a) AFM image of a LED structure grown with H_2 carrier gas. (b) SEM image of a LED structure grown with H_2 carrier gas. (c) SEM image of a LED structure grown with N_2 carrier gas. The pit density and surface roughness are reduced significantly by switching from N_2 to H_2 carrier gas. 89

61 (a) SEM image of a nano-diode structure. (b) Magnified SEM image in the center of the nano-diode showing well-shaped nanoridges. (c) Magnified SEM image at the edges of the nano-diode showing unfilled mask openings. 90

62 (a) ω scan of GaN peak at (00.4). (b) ω scan of InGaN peak at (00.4). The FWHM of GaN and InGaN peaks are 292 and 312 arcsec, respectively. 91

63 (a) $\omega/2\theta$ scan at (00.2). (b) $\omega/2\theta$ scan at (00.4). The blue curves represent experimental results while the red curves represent simulated fit results. The simulation shows about 6% Indium incorporation at the MQWs. 91

64 Room temperature CL spectra of nano-diode at various electron accelerating voltage. Note that the CL peak does not change with the electron accelerating voltage. 92

65 Room temperature CL spectra of nano-diode and control LED. The nano-diode shows enhanced CL emission as compared to the control LED, which is grown on the unpatterned area. 92

66 Optical image of a fabricated 100 x 100 μm^2 GaN/InGaN *p-i-n* nano-diode with control probe pad. 94

67 The I-V curve for the control LED. 95

68 The EL spectra of the control LED at various injection currents. Inset shows the emission at an injection current of 10 mA during testing. . 96

69 The I-V curve for the nano-diode. 97

CHAPTER I

INTRODUCTION

Within the past ten years, a wide variety of gallium nitride (GaN) based optoelectronic and electronic devices have opened a new era in the field of semiconductor research. Unlike silicon and gallium arsenide, GaN based devices can operate at high temperature and in hostile environments. The band gap of binary and ternary alloys of (Al,Ga,In)N can be engineered from 0.7 to 6.2 eV, which covers the ultra-violet (UV) and the whole visible spectrum. Furthermore, the GaN based transistor is a potential candidate to overcome the limiting performance of the Si based transistor in maximum frequency, power density, and breakdown voltage. However, the development of high performance GaN based devices has been limited by the lack of native substrates. The high melting temperature of GaN makes conventional bulk growth techniques like Czochralski or Bridgeman impossible.

Since the bulk GaN substrates are expensive and limited in size, GaN epitaxial layers are typically grown on a hetero-substrate such as sapphire, silicon carbide (SiC), or silicon. The lattice parameters and thermal expansion coefficients of GaN are mismatched with those of these hetero-substrates, leading to epitaxial growth with high densities of defects and poor surface morphology. These extended defects have a deleterious effect on the optical and transport properties of epitaxial growth. Numerous growth methods such as epitaxial lateral overgrowth and selective area growth have been developed to reduce the dislocation density, but the quality of the epitaxial growth has yet to be enough for high performance and high efficiency devices. The main focus of this dissertation is the growth, characterization, fabrication and testing of a high quality GaN based light emitting diodes (LEDs) grown by nano

selective area growth (NSAG).

This chapter presents background information on the III-nitrides material system including material properties, growth challenges, and description of the major growth methods used to reduce the density of dislocation in epitaxial growth. In particular, the theoretical study of stress relaxation in the nanostructure will be presented.

An introduction to the principle of metalorganic vapor phase epitaxy (MOVPE) system used in this research is presented in Chapter 2. The fabrication of nanomask, experimental GaN growth procedure and the description of the various characterization tools used are described in this chapter as well.

Chapter 3 of this dissertation focuses on the perfect selective area growth challenges of GaN microstructure. The growth rate enhancement of GaN microstructure is reported in conjunction with vapor phase diffusion model to verify the validity of the model.

Chapter 4 covers a complete discussion of III-nitrides nanostructures grown by NSAG and their optical and structural characterizations. The chapter starts with the homoepitaxy of GaN nanostructures, then to heteroepitaxy of GaN nanostructures on highly mismatched substrates. The demonstrated structural and optical characterization shows that a high quality and dislocation free GaN nanostructures can be obtained by this method. Structural properties in GaN nanostructures are analyzed by using submicron beam X-ray diffraction. At the end of this chapter, the growth of InGaN/GaN multi quantum wells (MQW) nanostructures and their optical and structural characterizations are presented.

The attempt to develop a GaN based LEDs grown by using NSAG is presented in Chapter 5.

Finally, this dissertation concludes with Chapter 6, a summary of results and a discussion of potential future research work.

1.1 Group III-nitride semiconductor structure and characteristic

1.1.1 Structural properties

Group III nitrides are compound semiconductor consist of element(s) from column III (B, Al, Ga, In) and element N from column V. While other compound semiconductor such as GaAs and InP exist in the zinc blende (cubic) crystal structure, nitride based semiconductors exist in both zinc blende and wurtzite (hexagonal) crystal structure (Figure 1). However, the wurtzite phase is the dominant state in terms of thermodynamic. Wurtzite phase possess unique material properties such as built-in electric fields due to piezoelectric and spontaneous polarization. The wurtzite structure has a hexagonal unit with lattice constant of a and c. The wurtzite structure is formed by two interpenetrating hexagonal close-packed sub-lattices with stacking sequence of $ABABABAB$ in the c-direction. In this structure, A atoms are surrounded by four B atoms in tetrahedral configuration. The space grouping of the wurtize structure is $P6_3mc$. The primitive vectors of the hexagonal structure are:

$$\vec{a_1} = \frac{1}{2}a\hat{x} - \frac{\sqrt{3}}{2}a\hat{y} \tag{1.1a}$$

$$\vec{a_2} = \frac{1}{2}a\hat{x} + \frac{\sqrt{3}}{2}a\hat{y} \tag{1.1b}$$

$$\vec{a_3} = c\hat{z} \tag{1.1c}$$

In the hexagonal system, Bravais-Miller index ($hkil$) are often used to denote the direction and crystallographic plane. In this notation, $i = -(h + k)$ because of the basis of vectors have an angle of 120° as shown in Figure 2. With this characteristic, it is possible to use Miller index of (hkl) to denote the hexagonal system by omitting i.

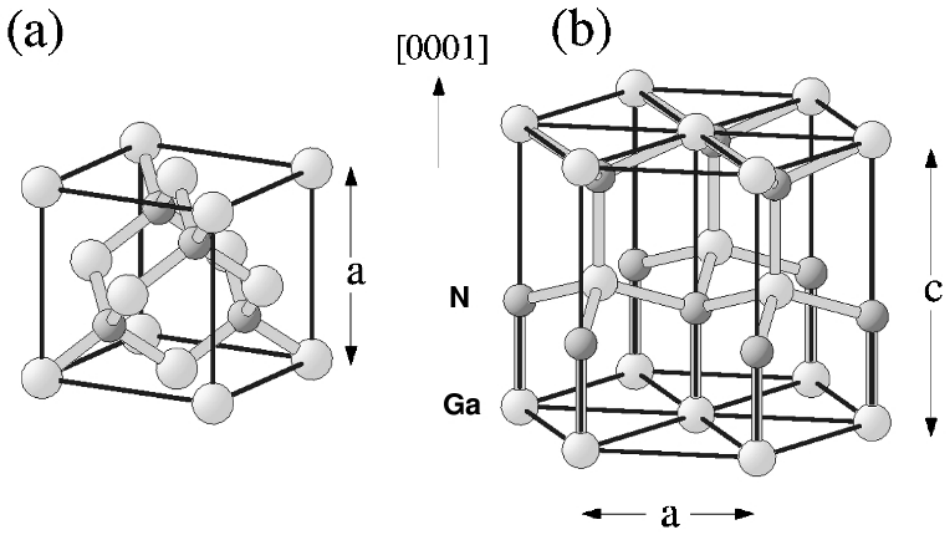

Figure 1: Crystal structures of III-nitrides (a) zinc blende and (b) wurtzite.

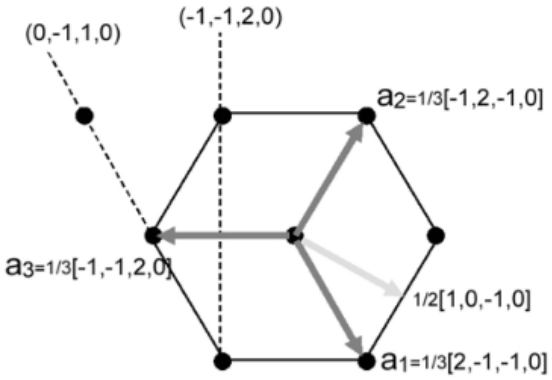

Figure 2: Bravais-Miller index of wurtzite GaN structure.

The lattice parameters of the group-III nitrides are as shown in the Table 1.

1.1.2 Electron bandstructure properties

Energy gaps (E_g) for the wurtzite III-nitride compound semiconductors covers from 0.7 eV (near infra-red) to 6.2 eV (ultraviolet) as shown in Figure 3. The temperature dependence of the energy gap in the Varshni form is:

$$E_g(T) = E_g(T=0) - \frac{\alpha T^2}{T+\beta} \tag{1.2}$$

Table 1: Lattice parameters of the group-III nitrides

Wurtzite(300K)	AlN	GaN	InN
a (Å)	3.112	3.189	3.54
c (Å)	4.982	5.185	5.707
$(c/a)_{calc}$	1.6190	1.6336	1.6270
$(c/a)_{est}$	1.6010	1.6259	1.6116

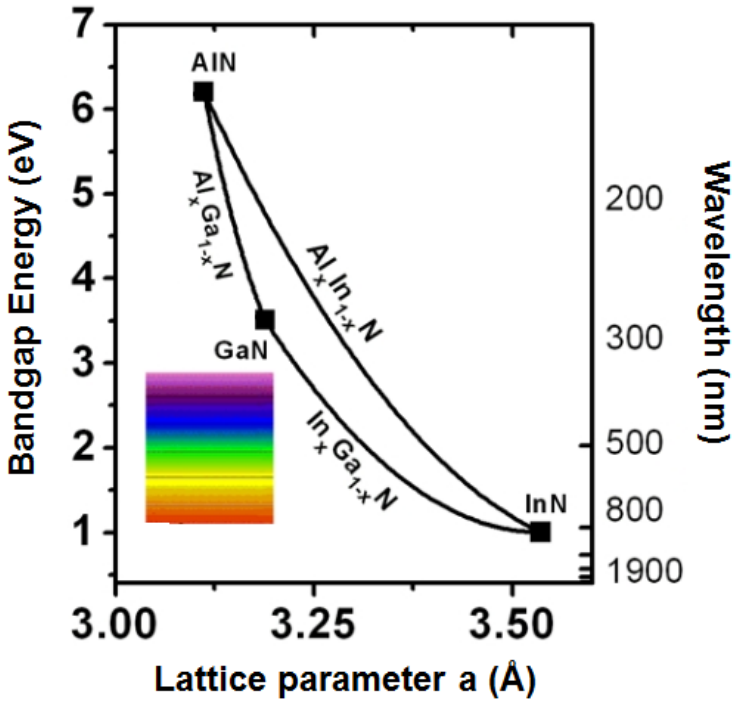

Figure 3: III-nitrides lattice parameter vs. bandgap energy.

Equation 1.2 shown above are accurate to within a few meV for bulk nitride materials. For a heteroepitaxial layer, other parameters such as interband deformation potentials a_1 and a_2, valence-band deformation potentials D_1 - D_6, elastic constants C_{11}, C_{12}, C_{13}, C_{33}, and C_{44}, valence-bad parameters A_1 - A_7, piezoelectric moduli d_{13}, d_{33}, and d_{15}, crystal-field splitting Δ_{cr}, spin-orbit splitting Δ_{so}, and spontaneous polarization P_{sp} has to be taken in account for. Table 2 list all the band structure parameters for wurtzite nitride binaries compiled by Vurgaftman *et al.*[1].

Table 2: Band structure parameters for wurtzite nitride binaries [1]

Parameters	GaN	AlN	InN
E_g(eV)	3.510	6.25	0.78
α (meV/K)	0.909	1.799	0.245
β (K)	830	1462	624
a_1 (eV)	-4.9	-3.4	-3.5
a_2 (eV)	-11.3	-11.8	-3.5
D_1 (eV)	-3.7	-17.1	-3.7
D_2 (eV)	4.5	7.9	4.5
D_3 (eV)	8.2	8.8	8.2
D_4 (eV)	-4.1	-3.9	-4.1
D_5 (eV)	-4.0	-3.4	-4.0
D_6 (eV)	-5.5	-3.4	-5.5
D_1 (eV)	-3.7	-17.1	-3.7
C_{11} (GPa)	390	396	223
C_{12} (GPa)	145	137	115
C_{13} (GPa)	106	108	92
C_{33} (GPa)	398	373	224
C_{44} (GPa)	105	116	48
A_1	-7.21	-3.86	-8.21
A_2	-0.44	-0.25	-0.68
A_3	6.68	3.58	7.57
A_4	-3.46	-1.32	-5.23
A_5	-3.40	-1.47	-5.11
A_6	-4.90	-1.64	-5.96
A_7 (eV Å)	0.00937	0	0
d_{13} (pm/V)	-1.6	-2.1	-3.5
d_{33} (pm/V)	3.1	5.4	7.6
d_{15} (pm/V)	3.1	3.6	5.5
Δ_{cr} (eV)	0.010	-0.169	0.040
Δ_{so} (eV)	0.017	0.019	0.005
P_{sp} (C/m^2)	-0.034	-0.090	-0.042

For an unstrained ternary alloy, the composition dependencies of the energy gaps can be calculated with simple Vegard's law as show in the following:

$$E_g(A_{1-x}B_x) = (1-x)E_g(A) + xE_g(B) - x(1-x)C \tag{1.3}$$

The parameter, C, is the bowing parameter where it accounts for the deviation from a linear interpolation between two binary points. The bowing parameter is always positive and reflects a reduction of the alloy energy gaps.

1.2 Heteroepitaial GaN

1.2.1 Introduction

Due to the high melting temperature of GaN and its associated high vapor pressure, it cannot be manufactured by conventional method such as Czochralski. Currently, the growth of GaN is in the form of epitaxial layers on a substrate of different nature by MOVPE, halid vapor phase epitaxy (HVPE), or molecular beam epitaxy (MBE). The lattice constant and the thermal expansion coefficient of the substrate are the two most important criteria to determine its suitability for GaN epitaxy. Today, the most common substrate used for GaN epitaxy are single crystalline sapphire (Al_2O_3), silicon carbide (SiC), silicon, GaN template and AlN template. Table 3 shows the physical properties of the potential substrates for GaN epitaxy.

The defect density of GaN heteroepitaxy layer on sapphire and silicon carbide are typically between 10^8 - 10^{10} cm^{-2} [2]. These defects create non-radiative recombination centers that introduce energy state in the forbidden band, reduce the carrier lifetime, decrease the optical efficiency as well as reduce the device lifetime. Therefore, new improved techniques are required to achieve heteroepitaxial layer with low threading dislocations (TD) for better device performance.

1.2.2 Lattice mismatch

III-nitride semiconductors are grown by heteroepitaxy. In heteroepitaxy, the epilayer is grown on a substrate of different material. As a result of lattice mismatch between the epilayer and the substrate, epilayer is strained to match lattice parameter of the substrate at an early stage of the growth. Figure 4 depicts the deformation of locally strained epilayer. The epilayer is under biaxial compression if the lateral lattice parameter of the epilayer, a_e is greater than the lateral lattice parameter of the substrate, a_s, and vice versa. According to the Poisson's effect, when a material is compressed in one direction, the material will tend to expand in the other two directions perpendicular to the direction of compresssion, as shown in Figure 4. The crystal lattices are deformed in three different directions, one in the growth directions (c-axis), while the other two lie in the plane parallel to the substrate (a-axis). Stress and stain in the crystal lattice are related by the stiffness tensor, C_{mn}, defined by the Hooke's Law.

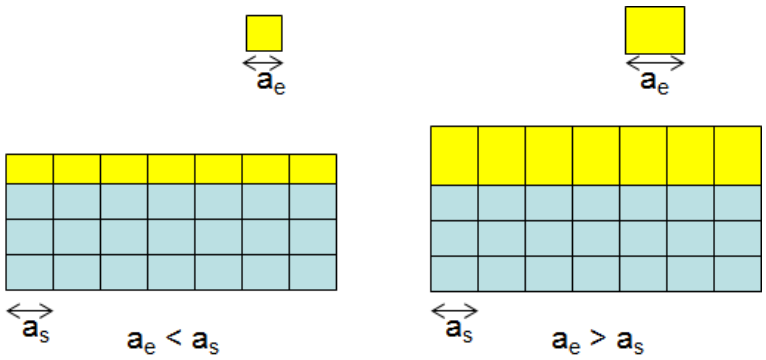

Figure 4: Lattice mismatch between the substrate and the epilayer: a) the epilayer is in tension, $a_e < a_s$ and, b) the epilayer is in compression, $a_e > a_s$.

Relative elongation in the crystal lattice is expressed in the following form:

$$\varepsilon_{xx} = \varepsilon_{yy} = \frac{a - a_o}{a_o} \; and \; \varepsilon_{zz} = \frac{c - c_o}{c_o} \tag{1.4}$$

The tensor expression of generalized Hooke's Law is written as

$$\begin{bmatrix} \sigma_{xx} \\ \sigma_{yy} \\ \sigma_{zz} \\ \sigma_{yz} \\ \sigma_{xz} \\ \sigma_{xy} \end{bmatrix} = \begin{bmatrix} C_{11} & C_{12} & C_{13} & 0 & 0 & 0 \\ C_{12} & C_{11} & C_{13} & 0 & 0 & 0 \\ C_{13} & C_{13} & C_{33} & 0 & 0 & 0 \\ 0 & 0 & 0 & C_{44} & 0 & 0 \\ 0 & 0 & 0 & 0 & C_{44} & 0 \\ 0 & 0 & 0 & 0 & 0 & \frac{1}{2}(C_{11} - C_{12}) \end{bmatrix} \begin{bmatrix} \epsilon_{xx} \\ \epsilon_{yy} \\ \epsilon_{zz} \\ \epsilon_{yz} \\ \epsilon_{xz} \\ \epsilon_{xy} \end{bmatrix} \tag{1.5}$$

Since the biaxial stress imposed by the lattice mismatch is in the growth plane (a-axis) only, the following can be deduced:

$$\sigma_{zz} = C_{13}\varepsilon_{xx} + C_{13}\varepsilon_{yy} + C_{33}\varepsilon_{zz} = 0 \tag{1.6}$$

After rearranging the terms,

$$\varepsilon_{zz} = -\frac{C_{13}\varepsilon_{xx} + C_{13}\varepsilon_{yy}}{C_{33}} \tag{1.7}$$

The equation can be further simplified due to symmetry of crystal structure in the growth plane, ε_{xx}=ε_{yy},

$$\varepsilon_{zz} = -\frac{2C_{13}}{C_{33}}\varepsilon_{xx} \tag{1.8}$$

The relationship between the elongation in the direction parallel (a-axis) and perpendicular (c-axis) to the growth plane is explicitly obtained in equation 1.8. The constant $-\frac{2C_{13}}{C_{33}}$ is called the Poisson's ratio.

1.2.3 Critical thickness

As the thickness of epilayer increases, the lattice mismatch induced strain energy increases as well. At one point, the strain energy becomes sufficiently large to generate

Table 3: Physical properties of the potential substrates for GaN epitaxy

Characteristic	Al_2O_3	6H-SiC	Si(111)	GaN	AlN
Lattice parameter a at 300K (Å)	4.76	3.08	5.43	3.19	3.11
Young's Modulus (GPa)	470	440	130	324	331
Thermal expansion coefficient (x $10^{-6}K^{-1}$)	4.3	10.3	2.5	3.17	1.58
Poisson's ratio	0.25	0.22	0.28	0.18	0.21
Thermal conductivity ($W.cm^{-1}.K^{-1}$)	0.5	4.9	1.5	1.3-1.8	1.7

plastic deformation in the epilayer. This thickness is generally known as the critical thickness, h_c. Below the critical thickness, the deposited atomic layers are elastically strained to match the lateral lattice parameter of the substrate; beyond the critical thickness, the material relaxes with formation of dislocation. The calculation for critical thickness is proposed by People and Bean [3, 4] with assumption that the epilayer is deposited on a very thick substrate relative to the epilayer. The critical thickness is,

$$h_c \simeq \frac{1-\upsilon}{1+\upsilon}\frac{1}{16\pi\sqrt{2}}\frac{b^2}{a(x)}\frac{1}{f^2}ln\frac{h_c}{b}, \tag{1.9}$$

where υ is the Poisson's ratio of the material, b is the slip distance, $a(x)$ is the bulk lattice constant of the film, and f is the lattice mismatch.

1.2.4 Coefficient of thermal expansion mismatch

The coefficient of thermal expansion is the relationship between the change of volume in a matter to a change of temperature. In heteroepitaxy, the substrate and epilayer are different materials and therefore, have different coefficients of thermal expansion. In the process of heating/cooling, both the substrate and epilayer expand/contract at a different rate. As the typical growth temperature of GaN is quite high (around 1000°C), the coefficient of thermal expansion mismatch plays an important role in determining the quality of the epilayer grown. Post growth cooling generate additional stress between the epilayer and the substrate, which often lead to formation of

dislocations or cracks. It is thus very crucial to choose a substrate with an acceptable coefficient of thermal mismatch to obtain high quality epitaxial growth. Table 3 lists the coefficient of thermal expansion for III-nitrides and some common substrates.

1.2.5 Defects in the GaN heteroepitaxy

GaN heteroepitaxy is subjected to many constraints as discussed in the previous sections. For a highly lattice mismatched system, such as GaN on sapphire, it is impossible to strain the epilayer to match the substrate perfectly. In this case, at an early stage of the growth, every seven GaN units match with eight {1 1 -2 0} sapphire units to form a locally coherent subgrain (Figure 5)[5]. Threading dislocations are generated with these locally coherent matched subgrains, whereas pure edge dislocations are formed from the coalescence of these subgrains. A large fraction of these dislocations recombine and vanish after a few tens of nanometer. A schematic structure of GaN/sapphire subgrains with tilt and twist characteristics is shown in Figure 6.

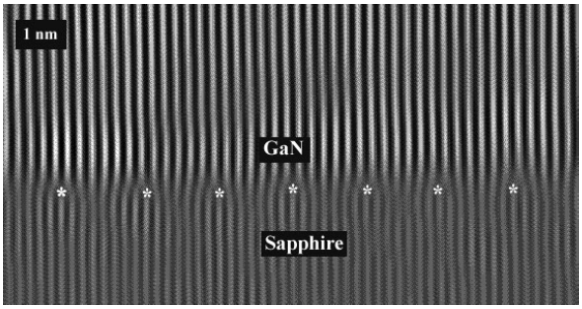

Figure 5: Misfit dislocations at the GaN/sapphire interface (figure reprinted from [5]).

There are three types of threading dislocations in heteroepitaxial GaN, which can be distinguished by the relative Burger vector **b** direction to the propagation vector, **u**, along the dislocation line. They are defined as,

- type a, edge dislocation, **b** is normal to **u**

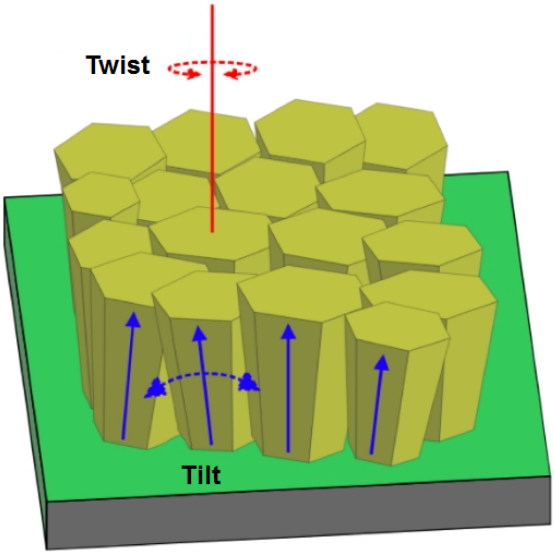

Figure 6: Schematic diagram of GaN/sapphire subgrains with tilt and twist.

- type c, screw dislocation, **b** is parallel to **u**
- type a + c, mixed dislocation, **b** is neither normal nor parallel to **u**, consisting of both edge and screw characteristics

The difference between each type of threading dislocations are depicted in Figure 7. The Burger vector for each type of dislocations are: **b** = <0 0 0 1> for screw dislocation, **b** = 1/3 <1 1 2 0> for edge dislocation, and **b** = 1/3 <1 1 2 3> for mixed dislocation. Threading dislocations formed by the "tilt" characteristic are made of mixed dislocation, while threading dislocations formed by the "twist" characteristic are made of edge dislocation.

In heteroepitaxial of GaN, the threading dislocation density is typically in the order of 10^7 - 10^9 cm^{-2}. With such a high density of threading dislocations, it is very challenging to obtain high efficient and high performance devices. In the following sections, various growth techniques to reduce the threading dislocation density are presented.

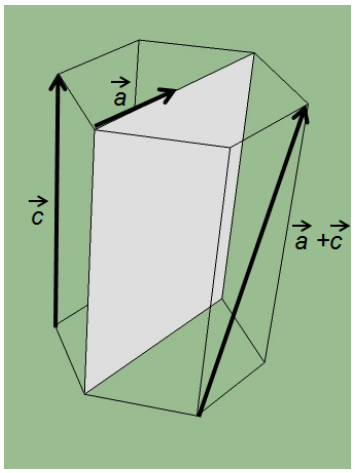

Figure 7: Unit cell of GaN with Burger vector of three types of dislocation: a type, c type, and $a + c$ type.

1.3 Reduction of the threading dislocation density by various growth techniques

1.3.1 Improved buffer layers with Si_xN_y interlayer

The use of Si_xN_y as a micromask to reduce TD density in GaN structures was first reported by Vennegues *et al.* [6]. It has been shown that the density of defects in the epitaxial growth can be reduced to mid 10^7 cm^{-2} by using Si_xN_y as a micromask [7]. In contrast to traditional two-dimensional growth mode, the growth with Si_xN_y exhibits a three-dimensional growth mode. Transition to this three-dimensional growth mode (aka Volmer-Weber growth mode) is explained by a reduction of sticking coefficient of the Ga precursors on the Si_xN_y. The Si_xN_y interlayer forms a mask which prevents crystallization of GaN on top of it. Hence, the growth of GaN occurs only on the parts of the substrate that are absent of Si_xN_y micromask. If the growth is continued, the GaN islands will laterally overgrow the Si_xN_y micromask and coalesce to form a single layer.

Cheng *et al.* has reported growth of GaN layers on silicon (111) substrate with a dislocation density of 3.0 x 10^8 cm^{-2} using a combination of AlGaN intermediate layers and a Si_xN_y interlayer [9]. Transmission electron microscopy (TEM) images

reveal that many TD are terminated by a Si_xN_y interlayer and AlGaN intermediate layers, as shown in Figure 8. After reaching the AlGaN intermediate layers and Si_xN_y interlayer, the TD bend in the (0001) plane, where they annihilate with dislocations of oppositive Burgers vectors.

One of the advantages of this method is that the Si_xN_y layer is grown *in situ* and therefore no additional lithography process is required to prepare the mask.

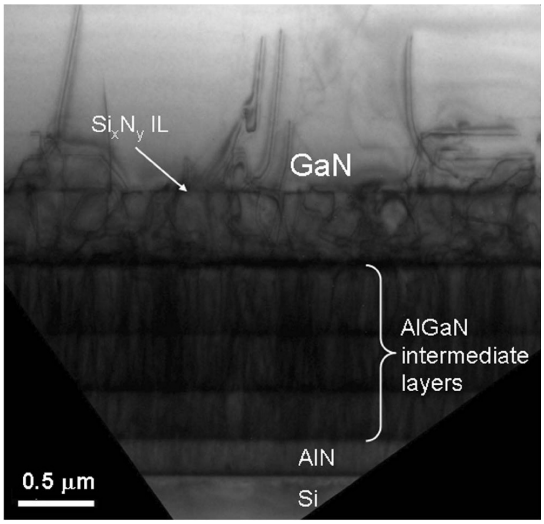

Figure 8: A cross-section TEM image showing dislocation reduction by SiN interlayer and AlGaN intermediate layers (figure reprinted from [9]).

1.3.2 Selective area growth

Kato *et al.* [10] was first to report selective area growth (SAG) of GaN on sapphire using MOVPE. Currently, MOVPE SAG is one of the main technology platforms for production of conventional monolithically integrated optoelectronic devices [11]. The main advantage of SAG is that it allows spatially controlled growth of the epitaxial layer through openings in a patterned substrate. SAG is a growth technique that combines both lithography and MOVPE growth. The process of SAG begins with deposition of dielectric masks on the substrate by a photolithography process. The purpose of these dielectric masks is to introduce a "no growth zone" on the substrate during the MOVPE process. Therefore, the reactive precursors arriving from the

gas phase to the wafer surface will not crystallize on the dielectric mask; they will, however, diffuse to the exposed region of the wafer, where the epitaxy process will take place. The exposed regions between the dielectric mask pads accumulate more materials (high growth rate) comparing to the regions that are far away from these masks (low growth rate). This process is shown in Figure 9.

The diffusion of reactive species can be categorized into three distinct types: vertical vapor-phase diffusion, lateral vapor-phase diffusion, and surface migration from the mask region. The effective lateral diffusion length D/k of the reactive species can be obtained by modeling the concentration profile, which uses the law of conservation of mass while taking into account the exchange process between the vapor phase and the surface [12]. D and k represent the diffusion coefficient in the vapor phase and the reaction constant on the wafer, respectively.

A perfect SAG is obtained when the growth takes place on the exposed region only and no polycrystals deposit on the mask. A perfect selective growth depends primarily on the growth conditions, specifically temperature [13], pressure [14], and molar fraction of the reactive species [15]. Figure 10 shows an example of SAG of GaN.

1.3.3 Epitaxial lateral overgrowth

Epitaxial lateral overgrowth (ELO) is currently the most widely used method for dislocation density reduction. It is reported that ELO reduces the dislocation density

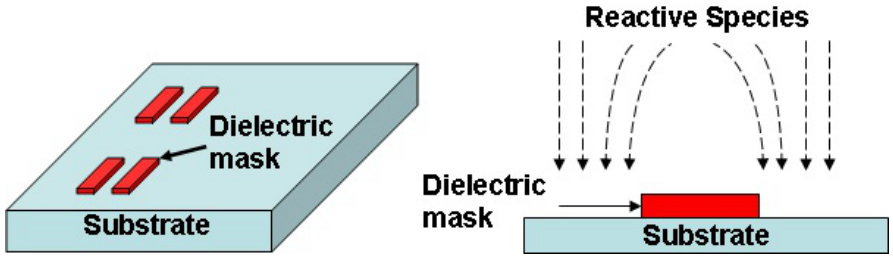

Figure 9: Schematic of the SAG: left figure shows a substrate patterned with dielectric mask; right figure shows the diffusion of reactive species to the exposed area.

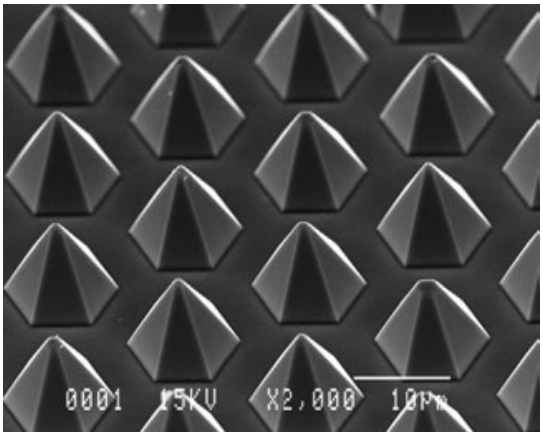

Figure 10: Selective area growth of GaN. After filling these openings, lateral growth starts and produces pyramids with {1-101} facets (figure reprinted from [16]).

to 10^6 cm^{-2} [17] and increases the lifetime of a laser diode to 10 000h [18]. The principle of ELO stems from the combined effect of SAG and growth anisotropy on different crystallographic planes. The growth anisotropy occurs as a result of incorporation of reactive species that are preferential on different crystallographic planes during the growth. Basically, the process starts with SAG to fill the exposed region, and then lateral overgrowth above the mask. The process continues until a smooth epitaxial layer is obtained. It is worthwhile to note that ELO can be implemented in MOVPE [19, 20] and HVPE [21] but not in MBE [22].

Hiramatsu *et al.* reported that the morphology of structures grown by ELO are strongly related to the reactor pressure and the growth temperature [23]. The changes in the growth morphology with the growth conditions are represented in Figure 11. For a growth temperature lower than 925°C (zone I), the surface appears to be rough and the structure has a triangular shape. However, when the temperature is increased, the surface becomes smoother and the structure becomes a truncated pyramid. On the other hand, if the pressure is lowered from 500 Torr to 40 Torr, the structure changes from a triangular shape into a trapezoid shape. By optimizing the growth conditions, a fast lateral overgrowth can be obtained.

There are two main ELO technologies: one-step growth ELO and two-step growth

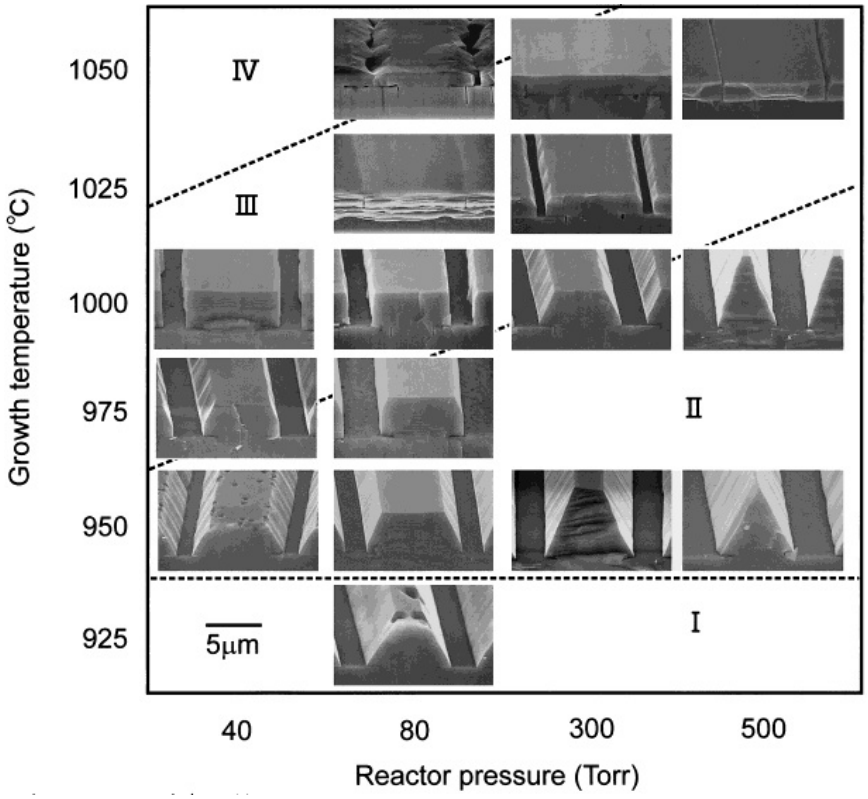

Figure 11: Morphological changes in ELO GaN for different reactor pressures and growth temperatures (figure reprinted from [23]).

ELO. In the one-step growth ELO, the growth in the opening is coherent with the substrate underneath, whereas the GaN over the mask extends laterally and coalesces when two wings meet each other. There are two highly defective regions in this method. One is the opening (coherent) regions and the other is the coalescence regions. In the two-step growth ELO, the growth conditions of the first step are tuned to form a pyramid structure. In the pyramid structure, it is energetically favorable for the dislocations to bend 90° and extend parallel to the surface of substrate. In the second step, the growth conditions are tuned to achieve full coalescence. In the two-step growth ELO, only the coalescence region is highly defective. The device structure is then grown on the less defective region. Figure 12 illustrates the different stages of ELO.

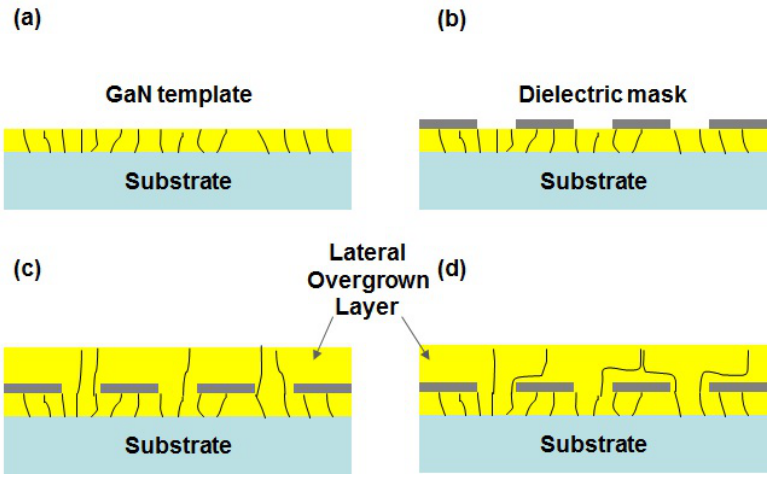

Figure 12: Schematic representation of the different stages of ELO: (a) a GaN template substrate, (b) dielectric mask is patterned on the GaN template, (c) one-step growth ELO, and (d) two-step growth ELO.

1.3.4 Nano selective area growth (approach chosen for our study)

Nano selective area growth (NSAG) is an extension of SAG to the level of the nano scale. The dielectric mask on the substrate contains nano openings (10-100 nm typically) where the nanostructures will be selectively grown. Due to its small size, a nanostructure possesses unique mechanical properties. In the conventional epitaxial growth, the epitaxial layer can only relax in the vertical direction (parallel to the growth direction) while the biaxial lattices are constrained to the substrate. Nanostructures, on the other hand, can relax in both the vertical and the lateral direction. The difference of stress relaxation between the conventional epitaxy growth and the NSAG is illustrated in Figure 13.

The theoretical study of stress relaxation in the nanostructure was pioneered by Luryi *et al.* in 1986 [24]. According to Luryi *et al.*, the critical thickness strongly depends on the lateral dimension of the epitaxial layer for a given lattice mismatch. It is therefore possible to obtain dislocation free growth of lattice mismatched materials when the lateral dimension of the epilayer is smaller than a critical length. In conventional epitaxy, the total strain energy stored in the system increases linearly

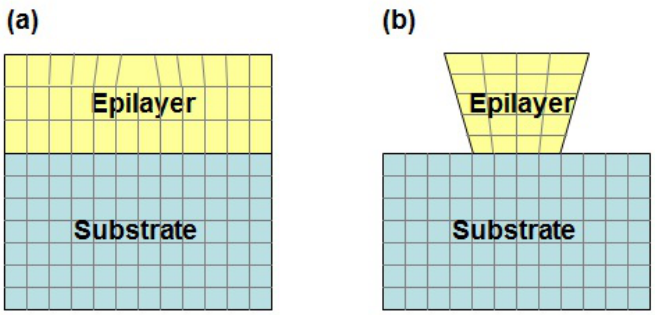

Figure 13: The difference of stress relaxation between (a) the conventional growth and (b) nano selective area growth. The epilayer grown by the conventional epitaxial growth can only relax in the vertical direction while the epilayer grown by NSAG can relax in both vertical and lateral direction.

(blue line in Figure 14) with the thickness of epitaxial growth until a dislocation is created. On the other hand, the total strain energy stored in the nanostructure does not increase linearly but saturates at after a certain height (red line in Figure 14) due to complete relaxation beyond that height. In theory, if the total energy at the saturation level is less than the amount of energy required to form a dislocation, a complete dislocation free epilayer can be grown regardless of the thickness.

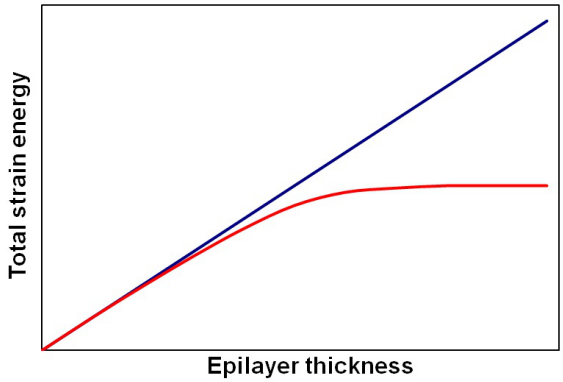

Figure 14: Total strain energy stored in the system versus the thickness of the epilayer grown by (a) conventional growth and (b) nano selective area growth.

1.3.4.1 A theoretical approach to nanoheteroepitaxy

Luryi *et al.* describe the discontinuous boundary value problem for epitaxial growth occurs on seed pads with no adhesion of the film between the pads, as illustrated in

Figure 15. Epitaxial growth of germanium is selectively deposited on pre-patterned silicon seed pads with length (along x-axis) assumed to be infinite and width (along y-axis) of 2L in value. The film is assumed to be free from dislocation and plastic deformation. The strain energy profile (ω) for this type of boundary value problem typically has an exponentially decaying dependence on the distance z from the source plane, with a characteristic length h_e of the decay. The epitaxial growth on top of the seed pads suffers misfit strain f along segment $(-l, l)$ in y direction, and the normal stress $\sigma_y = \sigma(y, z)$ can be approximately expressed in the following form.

$$\sigma(y,z) = f\frac{E}{1-\nu}\chi(y,z)e^{\frac{-z\pi}{2l}}, \tag{1.10}$$

where ν is the Poisson ratio and the E is the Young modulus of the epitaxial growth. The misfit strain is defined as

$$f = 2\frac{a_f - a_s}{a_s}, \tag{1.11}$$

where a_f and a_s are the lattice parameters of the epitaxial layer and the substrate, respectively. The lateral stress distribution is characterized by χ and it is in the form

$$\chi(y,z) = \begin{cases} 1 - \frac{coshky}{coshkl} & z \le h_e \\ 1 & z \ge h_e \end{cases} \tag{1.12}$$

The maximum strain energy density occurs at y = 0. The ω per unit area in the plane y = 0 is in the form

The interfacial compliance parameter k can be estimated by the following:

$$k = (\frac{3}{2}\frac{1-\nu}{1+\nu})^{1/2}\frac{1}{h_e} = \frac{\zeta(\nu)}{h_e}. \tag{1.13}$$

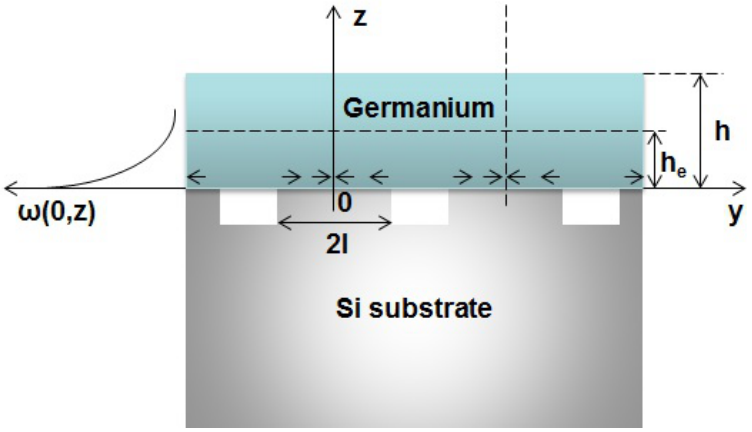

Figure 15: Illustration of the discontinuous boundary value problem for epitaxial growth occurs on seed pads with no adhesion of the film between the pads. The strain energy profile, ω(0,z), for the pad mid cross-section is shown on the left[24].

The strain energy density per unit volume, ω, and the maximum strain energy per unit volume, ϵ_s, are given by

$$\omega(y,z) = \frac{1-\nu}{E}\sigma^2. \tag{1.14}$$

$$\epsilon_s = \int_0^h w(0,z)dz = \frac{E}{1-\nu}f^2 h_e. \tag{1.15}$$

The integral of equation 1.15 can be extended by substituting the form of χ with z $\leq h_e$ to all values of z, since the range of z $\geq h_e$, gives a negligible contribution to the integral. Solving equation 1.15 gives h_e

$$h_e = h[(1 - sech\frac{l\zeta}{h_e})^2(1 - e^{\frac{-h\pi}{l}})\frac{l}{h\pi}] \equiv h[\phi(\frac{l}{h})]^2, \tag{1.16}$$

where the function $\phi(l/h)$ characterizes the reduction factor. For $l \ll$ h, $\phi \propto (1/h)^{1/2}$, and for $l \gg$ h, ϕ approaches 1 asymptotically. For $l \leq$ h, h_e in equation 1.16 becomes

$$h_e \approx \frac{l}{h}[1 - sech(\zeta\pi)]^2 \equiv \frac{l\xi^2}{\pi} \qquad h \geq l. \tag{1.17}$$

The areal energy density ϵ_D associated with a linear dislocation located at a distance h from the free surface of the film is compared with equation 1.15 [3]

$$\epsilon_D = \frac{Gb^2}{10a\pi\sqrt{2}} ln \frac{h}{b}, \tag{1.18}$$

where b is the Burgers vector of the linear dislocation, a is the bulk lattice parameter of the film and G is the shear modulus of the film. In the regime of (h $\gg l$), l arises as the integration cutoff in the divergent integral if the length of dislocation is less than the distance h from the free surface. Therefore, by substituting l for h in equation 1.18, replacing h_e in equation 1.15 with equation 1.17, and equating ϵ_s in equation 1.15 with ϵ_D in equation 1.18, we obtain

$$\frac{(f\xi)^2}{\pi} l = \frac{1-\nu}{1+\nu} \frac{1}{20\pi\sqrt{2}} \frac{b^2}{a} ln \frac{l}{b}, \tag{1.19}$$

where ξ = [1-sech($\xi\pi$)]^2. Solving l gives the minimum lateral dimension of the seed pad that is required for a defect-free epitaxial growth. The explicit form of l_{min} is

$$l_{min} = h_c \frac{\xi}{\sqrt{\pi}}. \tag{1.20}$$

This theoretical result shows that dislocation free germanium film can be epitaxially grown on a silicon seed pad, provided that $l \leq l_{min} \approx 10$ nm [24].

1.3.4.2 State of the art

Hersee *et al.* first demonstrated a three-dimensional stress relief mechanism in the GaN nanostructure grown on Si and SiC substrate [25, 26]. They later introduced pulsed growth into the selective MOVPE system to fabricate GaN nanowire LED [27].

On the other hand, Zang *et al.* demonstrated a GaN layer with dislocation density less than 10^8 cm^{-2} grown on Si by nano epitaxial lateral overgrowth [28].

CHAPTER II

GROWTH AND CHARACTERIZATION OF GAN

Numerous techniques can be used to epitaxially grow III-nitride materials. Currently, molecular beam epitaxy (MBE) and metalorganic vapor phase epitaxy (MOVPE) are the two most common growth techniques. Almost all of the reported high quality III-nitrides thin films are grown by one of these two techniques. MBE was invented by Cho *et al*. at Bell Laboratory in 1960 [29]. The advantages of MBE are precise control of the beam fluxes, good uniformity, compatibility with $in-situ$ surface analysis, and clean growth environment. However, the drawbacks of the this technique are low growth rate and expensive equipment.

Manasevit was the first to demonstrate the deposition of gallium arsenide on insulating substrates by MOVPE [30]. Currently, MOVPE is extensively used to grow device structures such as, LEDs, laser, transistors, photodetectors, and solar cells. The advantages of MOVPE are higher available growth rates, suitability for large scale production, excellent control and uniformity, and capability to grow complex structures. The downsides of MOVPE are toxicity and flammability of the reactive precursors. All materials and device structures in this study were grown utilizing MOVPE.

This chapter will discuss the basic principle of MOVPE and the different techniques that were used to characterize the structural and optical properties of the nanostructures grown by nano selective area growth (NSAG). The main characterization tools used are Nomarski optical microscopy, scanning electron microscopy, transmission electron microscopy, atomic force microscopy, synchrotron based X-ray diffraction, and cathodoluminescence.

2.1 Metalorganic vapor phase epitaxy

Metalorganic vapor phase epitaxy is a growth technique which involves two or more materials in gaseous form. These reactive species react with each other to form an epitaxial layer on a substrate. The whole MOVPE growth process can be categorized into four processes,

1. gas input - Two or more precursors in gaseous form are introduced into the reactor chamber.

2. pyrolisis - The precursors breakdown into smaller atoms or molecules.

3. diffusion and adsorption - The precursors diffuse and adsorb onto the substrate.

4. surface reaction and by-product output - The precursors react with each other to form an epitaxial layer on the substrate, and the by-product formed during the epitaxial growth are pumped away.

Figure 16 shows the schematic illustration of GaN epitaxial growth. The precursors used in MOVPE usually consist of alkyls of the group III elements and the hydrides of the group V elements. The general chemical reaction of this process can be expressed by the following equation.

$$R_3M + NH_3 \rightarrow MN + 3RH \tag{2.1}$$

In the first term, M represents the group III elements such as Al, Ga, or In, while R represents an alkyl group such as methyl (CH_3) or ethyl (C_2H_5). R_3M is a metalorganic compound, in which a metal element, M, is attached to an alkyl group, R_3. In the second term, N represents the group V elements such as P, As, N, or Sb, and H is hydrogen. Accordingly, the formation of GaN and AlN using trimethylgallium

(TMG), trimethylaluminium (TMAl), and ammonia (NH_3) can be described by the following:

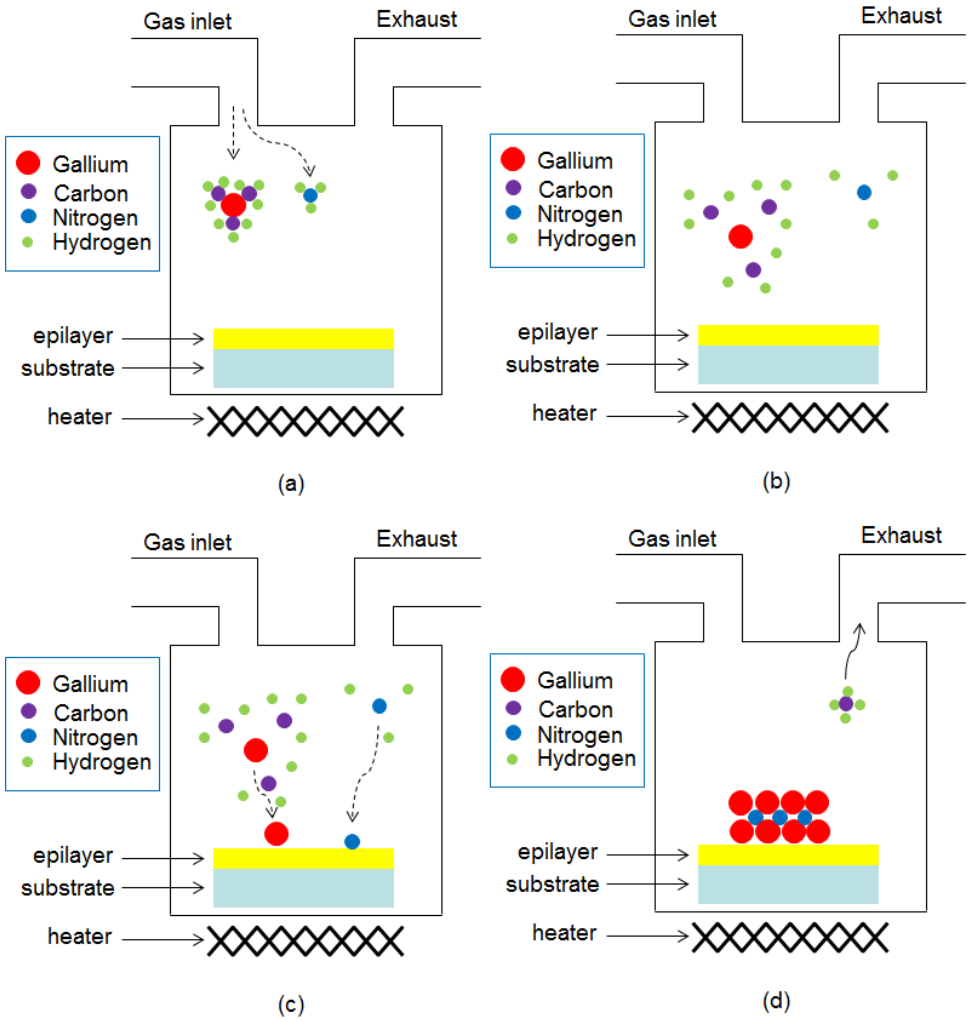

Figure 16: Schematic illustration of GaN epitaxial growth.

$$(CH_3)_3Ga + NH_3 \rightarrow GaN + 3CH_4 \tag{2.2a}$$

$$(CH_3)_3Al + NH_3 \rightarrow AlN + 3CH_4 \tag{2.2b}$$

Note that the above equations are a simplified form of the reaction and do not show the intermediate steps that may occur.

Table 4: Properties of group III precursors

Precursors	Melting point (°)	Boiling point(°)	a	b
Trimethylaluminium (TMAl)	15	125	8.22	2135
Trimethylgallium (TMGa)	-15	56	8.07	1703
Trimethylindium (TMIn)	88	134	10.52	3014

A carrier gas such as hydrogen or nitrogen is used to carry the metalorganics into the reaction chamber. The metalorganic precursors are stored in a bubbler in either solid or liquid form. The molar quantity of metalorganic precursor entering the reaction chamber is determined by the bubbler pressure, bubbler temperature, and the flow rate of carrier gas through the bubbler. Equation 2.3 shows the relationship between the equilibrium vapor pressure of metalorganic precursor and the bubbler temperature.

$$P_{sat} = 10^{a-\frac{b}{T}} \frac{1013.25}{760} mbar, \tag{2.3}$$

where a and b are the metalorganic precursor vapor pressure parameters, and T is the bubbler temperature. The values of vapor pressure parameters and melting and boiling temperature for different metalorganic precursors are given in Table 4.

2.1.1 Home-made T-shaped MOVPE system

The epitaxial growth of all the samples in this study was done using a homemade T-shaped reactor [31], as shown in Figure 17. The main components of the MOVPE system consist of a gas delivery system, sources and precursors, a reaction chamber, and an exhaust system. A simplified schematic version of the gas delivery system is shown in Figure 18. The gas lines for group III and group V are separated to avoid any premature mixing and gas phase reaction. In addition, the pressure of these lines are always kept in balance to avoid contamination from backfilling. The manifold in the gas delivery system diverts the flow of precursor into the reactor chamber or to

the exhaust system at the user's discretion.

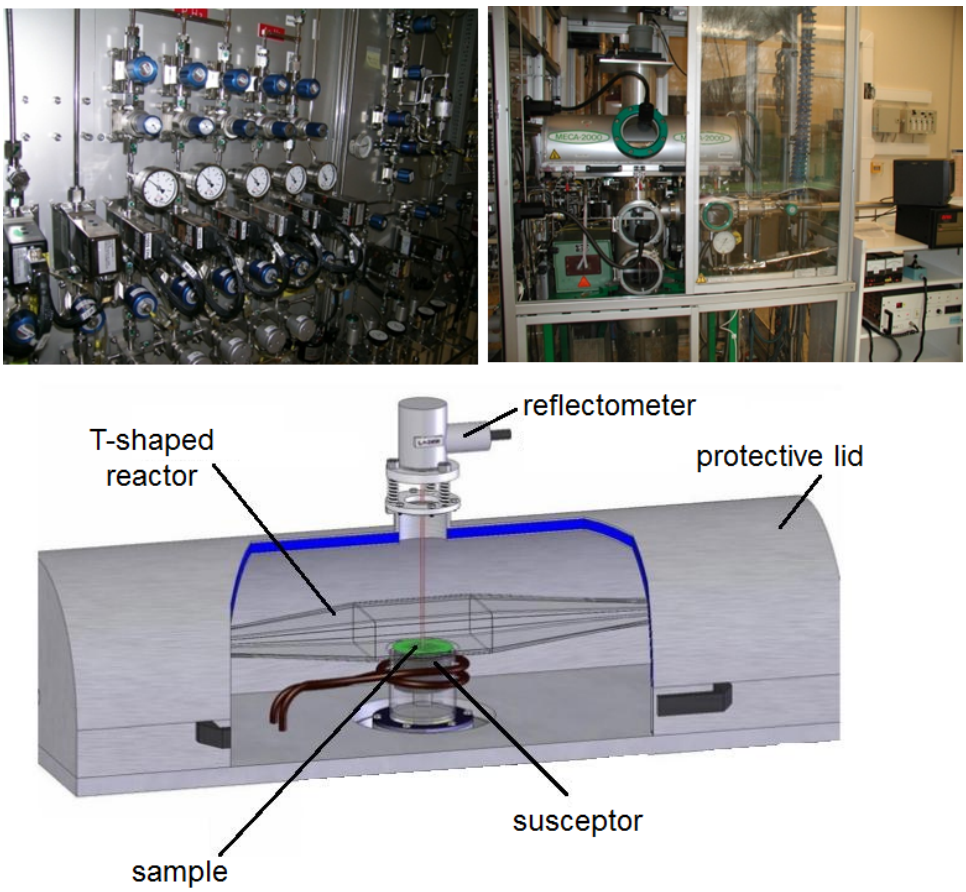

Figure 17: Home-made T-shaped MOVPE system.

Trimethylgallium, trimethylaluminium, trimethylindium and ammonia are used as the sources for group III and group V elements, while hydrogen and nitrogen are used as the carrier gases in this study. For p-type and n-type doping, biscyclopentadienyl magnesium (CpMg) and disilane (Si_2H_6) are used as the precursors for Mg and Si, respectively. In the process of doping, Mg will replace the group III element in the lattice and become an acceptor, while Si will claim the group V element site and become a donor. The growth temperature used in this study varies from 800 - 1000 °C, while the growth pressure varies between 75 and 750 Torr. Different substrates such as sapphire, silicon carbide, GaN templates, and AlN templates are used in this study.

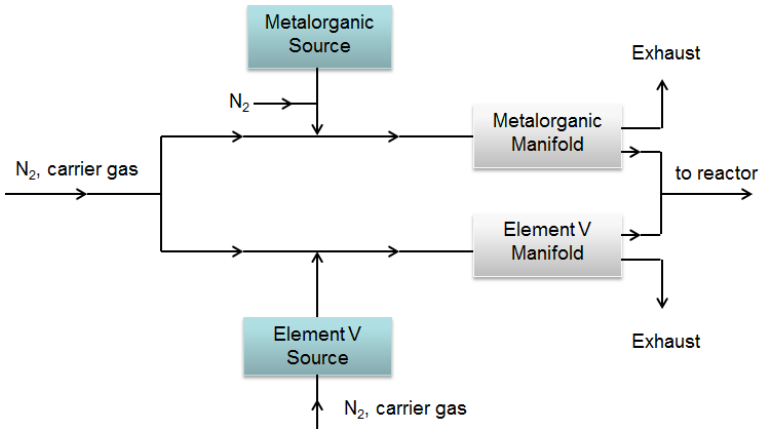

Figure 18: Simplified schematic of the gas panel used.

2.1.2 Reflectometer

The home-made T-shaped MOVPE system is equipped with an $in-situ$ reflectometer. The $in-situ$ reflectance measurement can be used to study the growth rate, surface roughness, and layer thickness. The principle of the reflectometer is illustrated on Figure 19. A laser beam of a chosen wavelength is illuminated on the surface of the epitaxial layer. Part of the light is reflected on the interface between air and the epitaxial layer while the remaining part is transmitted into the epitaxial layer. The light that is transmitted into the epitaxial layer will undergo multiple reflections in the cavity, which is formed by the structure air/epitaxy to epitaxy/substrate, before being reflected towards a detector that records the intensity of the reflected beam. The overall intensity of the reflected light is determined by the superposition of all of the reflected beams. When the phase difference between the reflected beams is just right, constructive or destructive interference will occur. The interference of reflected light forms an intensity modulation which is known as Fabry-Pérot oscillations.

The factors that govern the phase difference and the intensity of the reflected light are the refractive index of the material, the wavelength of the light, and the thickness of the epitaxial layer. The light source used in our study is a laser with an emission wavelength of 670 nm. The phase difference of the reflected light continues to vary

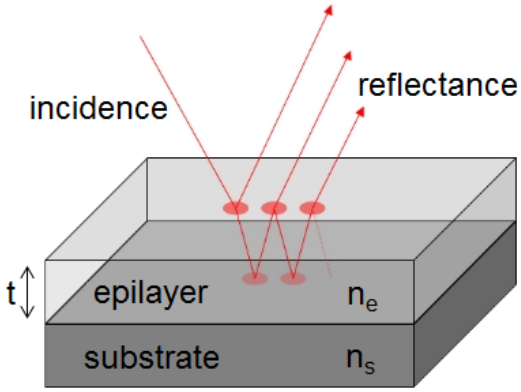

Figure 19: Principle of the reflectometry.

with the thickness of the growing epitaxial layer. When the phase difference between two beams is equal, as described in equation 2.4a, constructive interference, and therefore maximum intensity of reflectance, will occur. On the other hand, destructive interference, a minimum intensity of reflectance, will occur when the phase difference of the reflective beams is defined in equation 2.4b.

$$nd = m\frac{\lambda}{2}, \tag{2.4a}$$

$$nd = (m + \frac{1}{2})\frac{\lambda}{2}, \tag{2.4b}$$

where d is the thickness of growing layer, λ is the laser wavelength, n is the refractive index of a material at the growth temperature, and m is an even number. The growth rate can be determined by comparing the maximum or minimum of Fabry-Pérot oscillations,

$$Growth\ rate = \frac{\lambda}{2n\Delta t}, \tag{2.5}$$

where Δt is the period for one oscillation.

It should be noted that the intensity of the reflectance measurement can also be affected by the surface morphology. A reduction of reflected intensity can be caused by scattering effects if the surface of the growing layer is rough. This phenomenon can be used to characterize the surface roughness of the epitaxy growth. Figure 20 shows the influence of surface roughness on the intensity of reflected light.

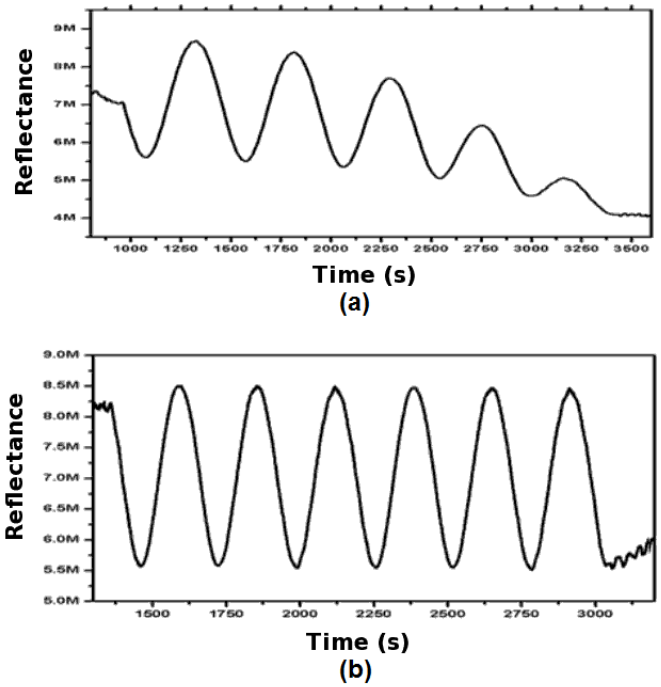

Figure 20: Influence of surface roughness on the intensity of reflected light: a) roughness increase, and b) smooth surface.

2.2 Nomarski DIC microscope

After the epitaxial growth, the samples are first characterized by Nomarski differential interference contrast (DIC) microscope before any other more sophisticated characterization tools. Optical microscopy is used to investigate the layer morphology, defects, and degree of selectivity of SAG. Although a smooth layer does not necessarily guarantee a high quality growth, a rough surface is often found to be highly defective. Likewise, a perfect selective growth does not necessarily guarantee a desired epilayer characteristic, but a non-selective growth is often undesirable in a

device structure.

A Nomarski DIC microscope is composed of a light source, a polarizer, a DIC prism, a condenser, a movable sample stage, an objective, a DIC slider, and an analyzer, as shown in Figure 21. Nomarski DIC amplifies contrast by using the principle of interferometry of polarized light. First, the light emitted from the light source is polarized by the polarizer. The polarized light is then separated into two signals that are perpendicular to each other by the DIC prism. When the separated signals pass through the sample of different refractive indexes, one of the light is delayed. Finally the two signals are combined by the DIC slider and analyzer. It is the phase difference between the two signals that produces an interference contrast in the image.

The theoretical resolution, R, of an optical microscope is given by the equation 2.6:

$$R = \frac{0.61\lambda}{NA} \tag{2.6}$$

where R is the smallest resolvable distance between two objects, NA is the microscope numerical aperture, and λ is the wavelength of the light source.

2.3 Scanning electron microscope

The scanning electron microscope (SEM) is an electron microscope that can produce a very high resolution image, revealing details down to the level of the nanometer scale. The SEM is commonly used to investigate the surface morphology of as-grown samples or fabricated devices. However, it can be also used to study the chemical composition and electrical conductivity.

In a typical SEM, electrons are accelerated to a high kinetic energy before they come into contact with the sample. Equation 2.7 shows the relationship between the

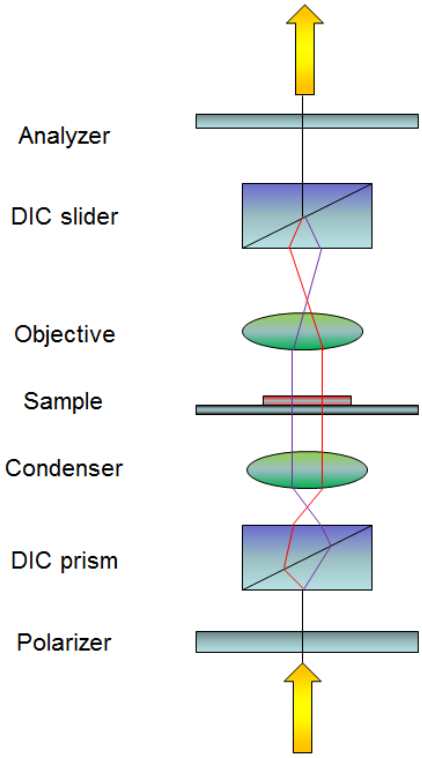

Figure 21: Schematic illustration of a Nomarski DIC microscope.

wavelength of accelerated electrons (λ) and their kinetic energy based on relativistic theory.

$$\lambda = \frac{h}{\sqrt{2m_e eV}\sqrt{1+\frac{eV}{2m_e c^2}}}, \tag{2.7}$$

where h is the Planck constant (4.13610^{-15} eVs), m_e is the electron mass (9.10910^{-28} g), e is the electron charge (1.60210^{-19} C), V is the potential difference, and c is the speed of light in vacuum (2.99810^{8} m/s).

The electron beam follows a vertical path in a vacuum chamber, through electromagnetic fields and magnetic lenses, which focus the beam toward the sample. The electrons interact with the atoms of the sample producing signals that contain information including surface topology, crystallographic structure, chemical composition, and electrical conductivity. The types of signal produced by a SEM are secondary

electrons, backscattered electrons, transmitted electrons, characteristic X-rays, and lights. These signals are collected by detectors and sent to a TV scanner to be analyzed. The schematic illustration of a SEM is shown in Figure 22 [32].

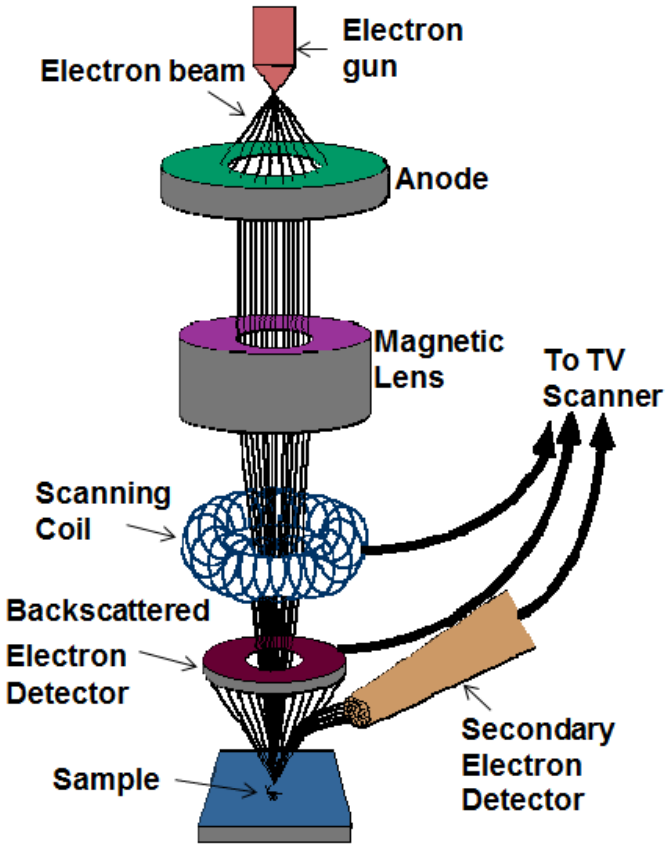

Figure 22: Schematic illustration of a SEM (figure reprinted from [32]).

2.4 Transmission electron microscope

The transmission electron microscope (TEM) utilizes the same basic principles as the optical microscope, except it uses focused beams of highly energized electrons, rather than photons, to magnify a sample. Equation 2.6 used for estimating the resolution for optical microscope, can also be applied to TEM. However, the smallest resolvable distance between two objects for TEM can be down to 2 Å, owing to the small de Broglie wavelength of electrons. Beside being widely used for high resolution imaging,

with additional add-ons such as X-ray detectors and electron energy loss detectors, the TEM can also be used to study chemical composition, structural and crystallographic properties of materials down to the atomic level.

A TEM produces a high resolution image from the interaction between the electrons transmitted through the sample in a vacuum chamber. The image can be manipulated by adjusting the amount of energy and hence, the electromagnetic wavelength, of the electron beams interacting with the specimen. If the voltage difference of the electron gun is increased, the electron beams are accelerated; the faster electrons move, the greater the quality and the details of the image. There are several types of interactions that can occur between the electron beams and the atoms of the specimen. If the electron does not come in contact with the atoms of the sample, it will penetrate through the sample and arrive at the detector unaffected. This reveals information about the density and/or thickness of the sample, as brighter areas of the image represent places where more electron pass through, while darker areas of the image represent places with fewer electrons pass through. On the other hand, if an electron does come in contact with the atoms of the sample, it can either make an elastic collision or inelastic collision. An inelastic collision occurs when part of the energy is lost to the atom to form phonons. The amount of energy loss in an inelastic collision is random and unpredictable. Therefore, this type of interaction between electron and sample does not bear any useful information, but rather random noise. Conversely, an elastic collision occurs when there is no loss in kinetic energy in the collision. The assumption of conservation of kinetic energy makes possible the calculation of the direction where the electron will be reflected. Therefore, the diffraction contrast, which arises from the interference between electrons from different angles, can be analyzed to reveal information about the sample on the atomic level. Diffraction contrast can be used to reveal information such as sample thickness, density, chemical composition, lattice defects, and more. The schematic illustration

of a TEM is shown in Figure 23 [33].

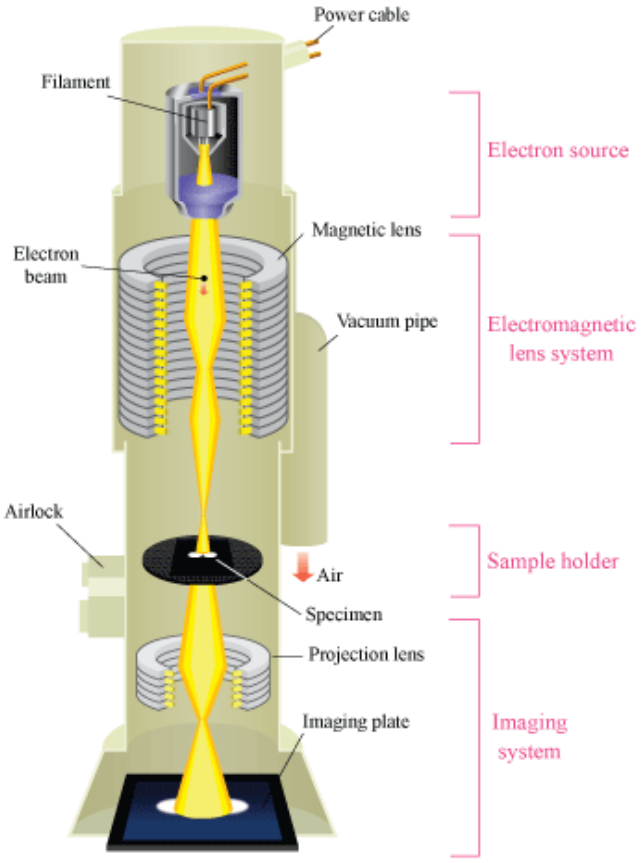

Figure 23: Schematic illustration of a TEM (figure reprinted from [33]).

2.5 Atomic force microscope

The atomic force microscope (AFM) is a very high resolution type of microscopy that forms images of surfaces using a physical probe that scans the surface of the specimen, revealing details down to the level of the nanometer scale. Unlike optical microscopy, the AFM has the ability to provide a high resolution map of the surface morphology both in lateral and vertical dimensions. It is a very useful non-destructive measurement technique to determine the surface roughness and defect density of a sample as well as the sizes and depths of the grain defects and nanostructures [34, 35].

The principle of AFM is based on the measurement of the displacement of the

tip and cantilever using reflected laser light and a detector. During a AFM scan, the tip, which is mounted at the end of a cantilever, sweeps horizontally across the sample surface at a steady rate. The cantilever flexes in response to the force between the tip and the sample surface. The amount of force between the tip and sample is dependant on the distance between the tip and the sample surface and the stiffness of the cantilever. It can be described using Hooke's Law:

$$F = -kx, \tag{2.8}$$

where F represents force, k is the stiffness of the cantilever and x is the distance between the tip and the sample surface. The difference between the incoming signal and the reflected signal from the cantilever, in response to the surface roughness, leads to an accurate measurement of the surface topography.

There are three distinct modes that can be used to study a sample surface:

- Contact mode: In contact mode, as its name implies, the tip is kept in contact with the surface and dragged across it. Contact mode maintains a constant deflection to keep the force between the tip and the surface constant.

- Non-contact mode: In non-contact mode, the tip is kept a constant distance from the surface. The force required to maintain a constant distance from the surface is used to measure the surface topography.

- Tapping mode: In tapping mode, the tip is kept close enough to the sample for short-range forces to become detectable while preventing the tip from contacting the surface. This allows the cantilever to oscillate at its resonant frequency, with an increase in sensitivity by several orders of magnitude.

The AFM tool used in this study was a Veeco Dimension 3100. All the measurements were performed using the tapping mode. The AFM is used to investigate the

selectivity of the sample, surface topography of the micro- and nanostructures, as well as the surface roughness of the microstructures. The schematic illustration of AFM is shown in Figure 24.

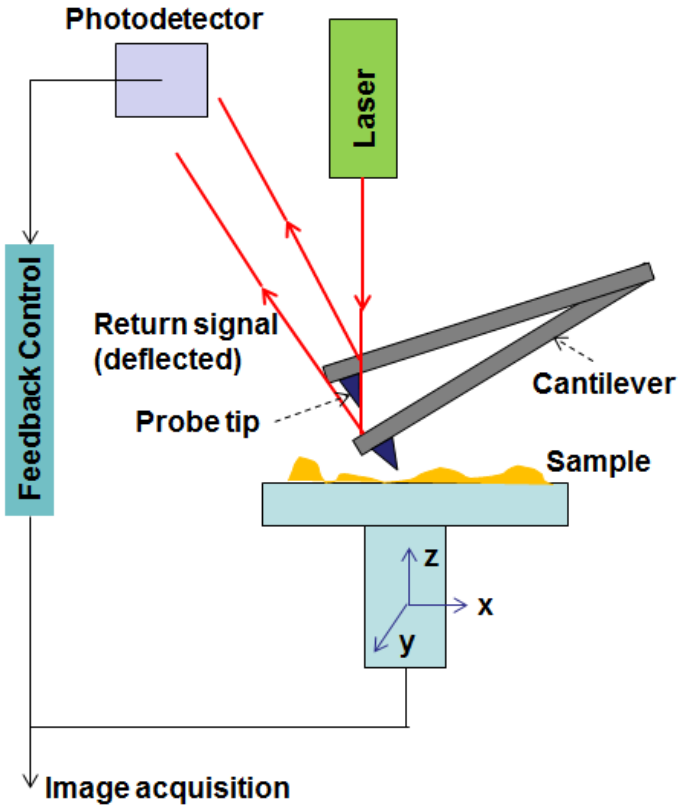

Figure 24: Schematic illustration of AFM.

2.6 Synchrotron based X-ray diffraction

X-ray diffraction (XRD) is an extremely important tool for studying semiconductor materials, especially heterostructures. The basic principle of X-ray diffraction is described by the dynamical theory of diffraction [36]. X-ray characterizations are non destructive and no sample preparation is required. The prime purpose of the XRD measurement is to determine the lattice constants of the epitaxial layers. Using these values, an accurate calculation can be made of the compositions, uniformity, strains, relaxations, and thicknesses of the epitaxial layers [37]. Furthermore, information on

dislocation density, interface quality, and tilt can also be obtained.

To study the structural properties of a nanostructure, a synchrotron based X-ray diffraction system is necessary. Conventional XRD systems do not have the capability to characterize structures at the level of submicron scale because they do not have enough excitation power when the beam size is reduced to the submicron scale. However, synchrotron-based X-ray sources circumvent this limitation by supplying ultra-high-intensity light. In a synchrotron, electrons are accelerated to high speeds in several stages to achieve a final energy that is typically in the gigaelectronvolt range. The electrons are forced to travel in a closed path by strong magnetic fields. Relativistic speed changes the observed frequency by a factor of γ due to the Doppler effect.

The principle of X-ray diffraction is based on Bragg diffraction formed by the interaction of X-rays and the electron cloud surrounding each atom in the crystal. Bragg diffraction occurs when monochromatic X-rays with a wavelength comparable to the atomic spacings of a crystalline sample are specularly reflected from the crystal planes, and interfere in a constructive manner. This can be described by Bragg's Law, as shown in equation 2.9.

$$n\lambda = 2d_{hkl}sin(\theta_B), \tag{2.9}$$

where d_{hkl} is the spacing between the lattice planes with miller indexex hkl, θ_B is the angle of incidence, λ is the wavelength of the X-ray source, and n is an integer known as the order of diffraction of the corresponding Bragg reflection. Constructive interference occurs when the path difference between two reflected X-rays is equivalent to $2d_{hkl}\sin(\theta_B)$, as shown in Figure 25.

The spacing between the lattice planes, d_{hkl}, can be related to hexagonal lattice

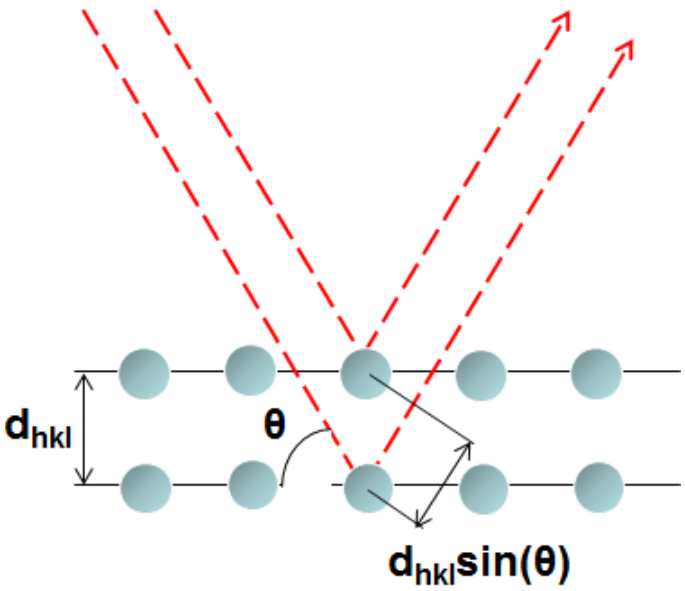

Figure 25: X-ray diffraction at the Bragg angle.

constants c and a by the equation 2.10:

$$d_{hkl} = \frac{1}{\sqrt{\frac{4}{3a^2}(h^2 + k^2 + hk) + \frac{l^2}{c^2}}} \tag{2.10}$$

There are two unknowns, a and c, in equation 2.10. Thus, at least two d_{hkl} measurements are needed to determine the value of a and c. The value of c can be easily obtained by searching for θ_B for planes with symmetric miller indexes, e.g., 001. By combining the equation 2.9 with 2.10, we obtain

$$c = \frac{nl\lambda}{2sin(\theta_B)} \tag{2.11}$$

The value of a can then be determined by performing a high angle asymmetric scan, e.g., searching for θ_B for the 105 reflection, and then using the value of c found previously and the equation 2.9 and 2.10.

In a perfect crystal with no defects or strain, a θ-scan gives a line characteristic

at the Bragg angle. However, in reality, crystal growths are never perfect, and they suffer from structural defects, dislocations, unintentional dopants, and strain. These imperfections result in crystal deformation and lead to peak broadening at the Bragg angle. Consequently, the full width half maximum of the diffraction peak can be used to compare the quality of different samples.

If an uniform epilayer with good surface quality is grown, interference fringes can be observed in a symmetric XRD scan. It is possible to determine the layer thickness from the separation of adjacent maxima by using equation 2.12 [37]:

$$t = \frac{n_i - n_{i+1}\lambda}{2(sin\theta_{ni} - sin\theta_{n(i+1)})}, \tag{2.12}$$

where λ is the radiation wavelength, n_i is the order of the fringe, and θ_{ni} is the angular position of the adjacent maxima.

If the material is assumed to be unstrained or the strain due to defects can be neglected, the composition of ternary compounds can be determined by Vegard's law. Vegard's law assumes that the lattice parameters of an alloy will vary linearly with the concentrations of each constituent element. Equation 2.13 shows the composition of a AlGaN alloy, x, can be determined using Vegard's law [38, 39]:

$$x = \frac{c_{AlGaN} - c_{GaN}}{c_{AlN} - c_{GaN}} \tag{2.13}$$

On the other hand, if the thin film is fully strained, the elastic deformation of the unit cell has to be taken in account. With a simple modification to equation 2.13, the composition, x, of a fully strained ternary alloy can be approximated by equation 2.14 [38, 40]:

$$x = \frac{1 - \upsilon}{1 + \upsilon} \frac{c_{AlGaN} - c_{GaN}}{c_{AlN} - c_{GaN}}, \tag{2.14}$$

where υ is the Poisson's ratio of the alloy, which can be approximated by linear interpolation between the values for each constituent element.

2.7 Cathodoluminescence

Cathodoluminescence (CL) is a process that measures the spontaneous emission spectrum of a direct bandgap semiconductor that is being excited by a electron beam. CL is an important characterization technique for determining the bandgap, material composition, relative material quality, stress distribution, and nature of defects present in a material.

The principle of CL is based on the radiative recombination of electron-hole pairs (EHPs). EHPs are created due to excitation of carriers to a higher energy state by the electron beam. These EHPs are unstable and will return to a lower energy state by either a radiative or non-radiative recombination. The time between creation and recombination of EHPs is typically in the order of nanoseconds. When EHPs recombine via radiative recombination, the event gives off a characteristic photon, which can be used to determine the bandgap of the material. Furthermore, the photon spectrum also provides information about the defect states within the material system. The relationship between the bandgap of a material and the corresponding characteristic wavelength is described by equation 2.15:

$$E_g = \frac{hc}{\lambda}, \tag{2.15}$$

where Eg is the bandgap energy of a material, h is Plank's constant, c is speed of light, and λ is the wavelength.

CL can also be used to perform depth-resolved measurement. Unlike photoluminescence which can only characterize the optical properties on the surface, CL

allows characterization of the optical properties underneath the surface. This can be achieved by changing the accelerating voltage, which in turn controls the electron penetration depth. The electron gun used in our setup can provide accelerating voltages in the range $0.1 < V < 30.0$ kV, probe currents in the range $4 < I < 10$ pA, and magnifications in the range $12X < M < 900{,}000X$. Figure 26 shows a graph of maximum range of depth versus the maximum energy loss of incident electron energy on a GaN layer.

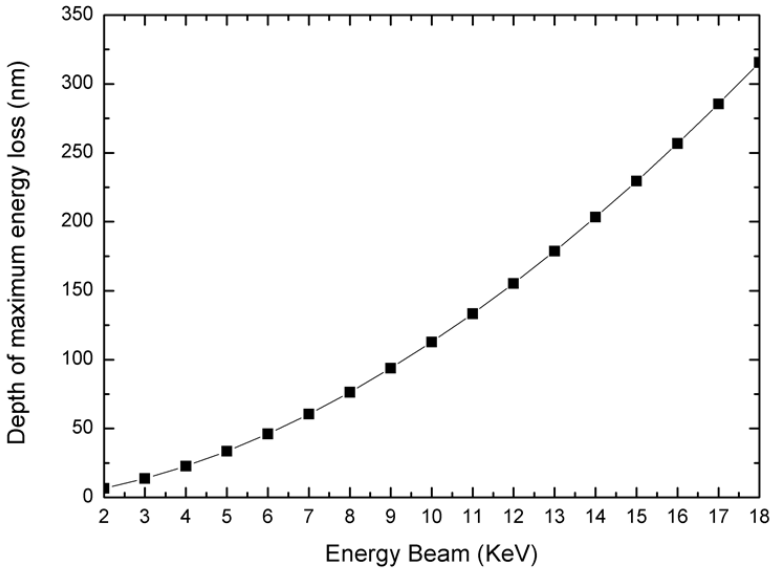

Figure 26: Depth of penetration of the electron beam on GaN layer.

CHAPTER III

MICRO SELECTIVE AREA GROWTH

The preliminary research work was focused on the selective area growth of GaN micro- and nanostructures as well as the characterization of these materials. Our preliminary work can be divided into three phases. In the first phase, we studied and optimized the selective area growth (SAG) of GaN microstructures. Following the success in achieving perfect SAG at the micrometer scale, we continued to grow GaN nanostructures by nano selective area growth (NSAG). Finally, we studied NSAG of GaN on highly lattice mismatched materials. Toward this end, both micro and nano selective area growth of GaN were grown on sapphire, SiC, GaN and AlN templates successfully.

This chapter covers the study of selective area growth of GaN layers at the micrometer scale. Selective area growth of GaN micostructures were grown on a pre-patterned GaN template substrates with oxide masks of various geometrical dimensions. The selectivity and morphological properties were characterized by atomic force microscopy (AFM) and white light interferometric measurements were used to characterize the thickness profiles of the GaN layers to obtain the growth enhancement due to SAG. The vapor phase diffusion coefficient D/k for the Ga precursor was obtained by numerical simulation of the experimental thickness profiles of GaN layers using a three-dimensional vapor phase diffusion model.

3.1 Experimental procedures

To study the SAG of GaN, the (0001)-oriented GaN template substrates are covered by pairs of rectangular masks with various geometries. The patterns are defined in the mask by conventional photolithography and reactive ion etching. Figure 27 shows

the process for micro mask preparation by optical lithography used in this study. In the first step, a silicon dioxide layer is deposited on the wafer by plasma enhanced chemical vapor deposition. A layer of negative photoresist is subsequently spin coated on top of the silicon dioxide layer. The photoresist is illuminated by the UV light with the desired pattern in the third step. The portion of the negative photoresist that is exposed to light becomes insoluble to the photoresist developer. Therefore, only the unexposed portion of the photoresist is dissolved by the photoresist developer. Reactive ion etching is used to remove the silicon dioxide layer to expose the GaN layer underneath. Finally the photoresist is remove by acetone bath. Two important characteristic dimensions of the mask are defined by Wm and Wo as shown in Figure 28. Both Wm and Wo are varied from 20 to 220 μm and from 20 to 60 μm respectively.

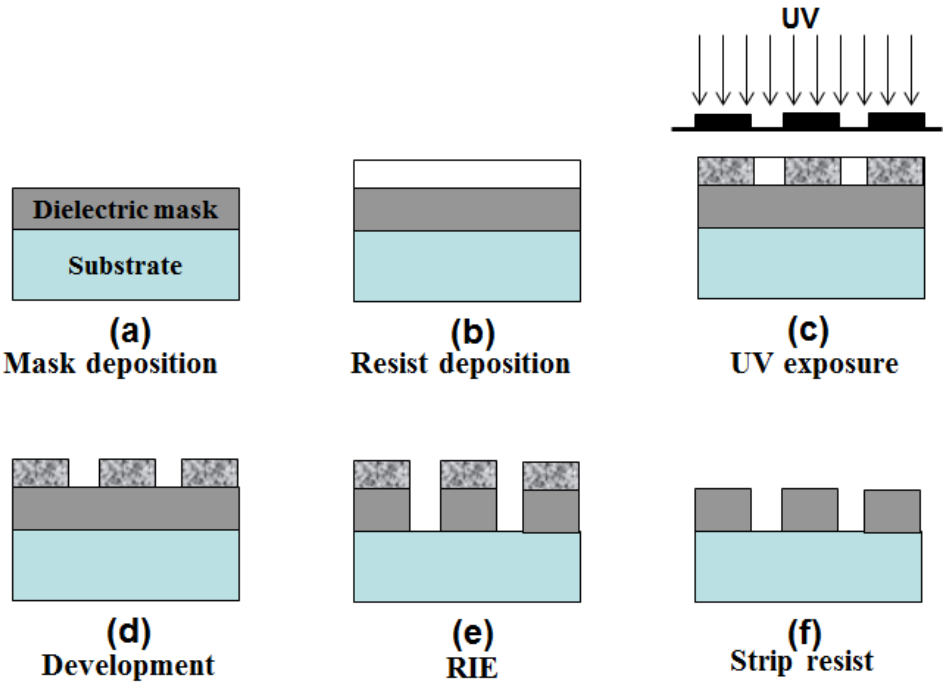

Figure 27: Process for micro mask preparation by optical lithography.

As the wafers have undergone photolithography process to prepare mask, a cleaning process is required to remove any impurities on the surface of the wafers. The sample cleaning procedure is described in the following:

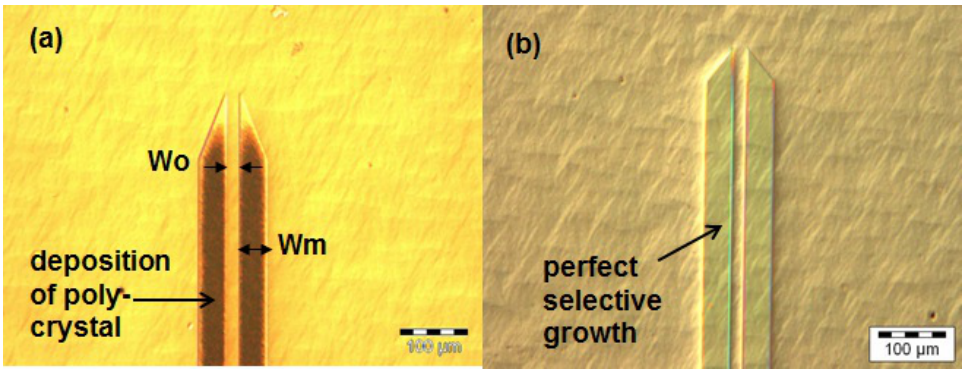

Figure 28: Optical images show the influences of growth condition of the selective area growth with (a) high growth rate and (b) low growth rate.

- Put the sample in a beaker full of acetone and ultrasonic bath for 5 mins. Take the sample out and rinse with DI water.
- Put the sample in a beaker full of ethanol and ultrasonic bath for 5 mins. Take the sample out and rinse with DI water.
- Put the sample in a beaker full of DI water and ultrasonic bath for 5 mins.
- Put the sample in a beaker filled with acid sulphuric for 30 seconds. Subsequently thoroughly rinse with DI water.
- Put the sample on a filter paper and blow dry with N_2

The epitaxial growths were performed by MOVPE in a T-shaped reactor [31] using 100% nitrogen as carrier gas. Trimethylgallium (TMGa) and ammonia were used as the sources of gallium and nitrogen, respectively. The growth temperature of the GaN was 1000°C and the pressure in the growth chamber 133 x 10^2 Pa (100 Torr). The V/III molar ratio in this study was fixed at 4500. The growth rate was kept relatively low (< 1 μm/h) to ensure a good selectivity. The nominal (i.e. far from the dielectric masks) thicknesses of the grown GaN layer were 200 nm. $In-situ$ reflectometry was utilized to measure the nominal growth speed and layer thicknesses.

3.2 Optimization of the growth condition

Figure 29 shows optical images of SAG on GaN template. In Figure 29a, deposition of GaN polycrystal was found on the mask. After optimizing the growth conditions, a perfect selective growth was obtained as shown in Figure 29b. The most important parameters for the growth conditions to achieve perfect selective growth are:

- high temperature, >1000°C
- low growth rate, <1 μm/h

High temperature is favorable for selective area growth due to the increase of effective diffusion length with temperature [12]. Lower growth rate correspond to lower limiting reactive species (TMGa in our study) flow rate reduces the probability of polycrystal deposit on the mask.

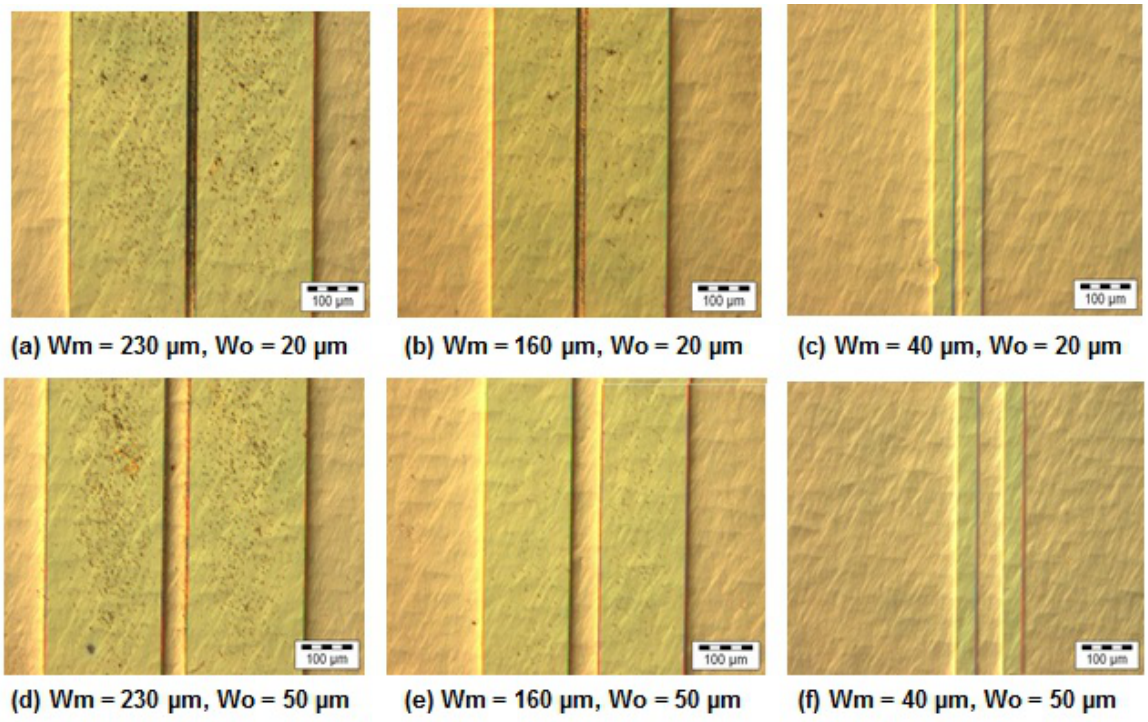

Figure 29: Optical images of the micro-SAG on the GaN template with masks of different dimensions.

Table 5: Parametric study of SAG on the width of the mask (Wm) and the width of the opening (Wo).

20 - 60	20 - 50	20 - 40	20 - 30	20 – 20	9
40 – 60	40 – 50	40 – 40	40 - 30	40 - 20	8
60 – 60	60 – 50	60 – 40	60 - 30	60 - 20	7
80 – 60	80 – 50	80 – 40	80 - 30	80 - 20	6
100 – 60	100 – 50	100 – 40	100 - 30	100 - 20	5
120 – 60	120 – 50	120 – 40	120 - 30	120 - 20	4
140 – 60	140 – 50	140 – 40	140 - 30	140 - 20	3
160 – 60	160 – 50	160 – 40	160 - 30	160 - 20	2
220 – 60	220 – 50	220 - 40	220 - 30	220 - 20	1
5	4	3	2	1	

Perfect Selectivity
Few Deposition
Many Deposition

Width of mask (μm)

Width of opening (μm)

The influence of the mask dimension (Wm and Wo) on the selective area growth was studied. Figure 29 shows the optical images of SAG on GaN template with masks of different dimensions. Many polycrystals were found deposited on the mask with 230 μm width; however, perfect selective growth was achieved on the mask with 40 μm width. This phenomenon can be attributed to the correlation between the diffusion length and the width of the mask (Wm). If Wm is larger than the diffusion length of the reactive species, the reactive species will deposit on the mask. Table 5 shows a parametric study of SAG on the Wm and Wo. A perfect selectivity was found for the values of Wm less than or equal to 60 μm.

3.3 Study of growth rate enhancement

In the following we will discuss the properties of the SAG structure with perfect selective growth and good surface morphology (Wm $<$ 60 μm). AFM is used to characterize the profile of the layers and the surface roughness. Figure 30a shows an AFM scan of GaN SAG on the pattern with Wm = 60 μm and Wo = 40 μm. The deposited layer resembles a ribbon in shape, with smooth vertical facets. The profile

of this ribbon shape layer is shown in Figure 30b. The difference in height between the edge and the middle of the ribbon is 170 nm. An AFM scan performed at the top surface of the GaN ribbon is shown in Figure 30c. The surface rms roughness is 0.4 nm. The hexagonal pits shown in Figure 30c are the threading dislocations propagated from the substrate. The threading dislocations density is estimated to be 1.6 x 10^8 cm^{-2}, which is about the same of the threading dislocations density of the substrate.

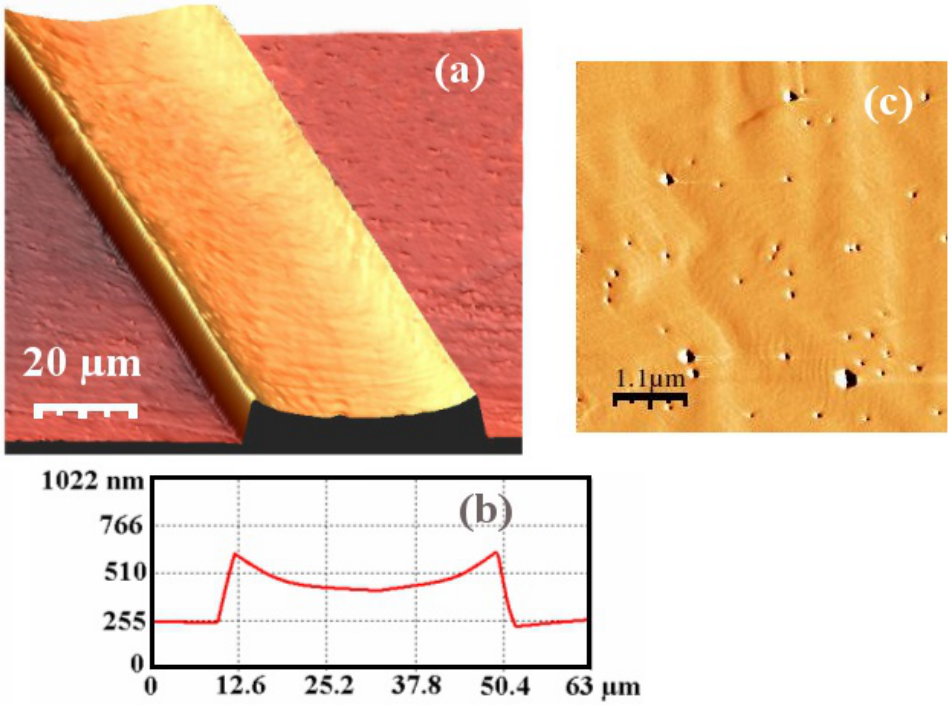

Figure 30: Morphological studies of GaN structure grown by SAG, (a) AFM micrograph, (b) height profile, and (c) surface scan of the top surface.

The dielectric mask is removed and the relationship between growth rate enhancement and the Wm and Wo parameters is studied. White light interferometry is used to measure the height of each pattern. The growth rate enhancement ratio R is defined as the ratio between of the height in the middle of the GaN ribbon with respect to the nominal thickness. Figure 31a shows the dependencies of R versus Wm for the SAG structures with Wo of 20, 30 and 40 μm. The obtained quasi-linear relationship

is similar to that reported by Gibbon *et al.* [12] for selective growth of InP-based compound semiconductors using similar mask geometry. For a fixed value of Wo, R increases with Wm because of the additional supply of the growth species desorbed from the mask surface. In Figure 31b, R is plotted against Wo for three values of Wm (60, 80 and 100 μm). The growth rate enhancement decreases with Wo for fixed Wm. This observation can be explained as follows: for a given diffusion length, the supply of extra species reaching the center of the stripe decreases for large Wo.

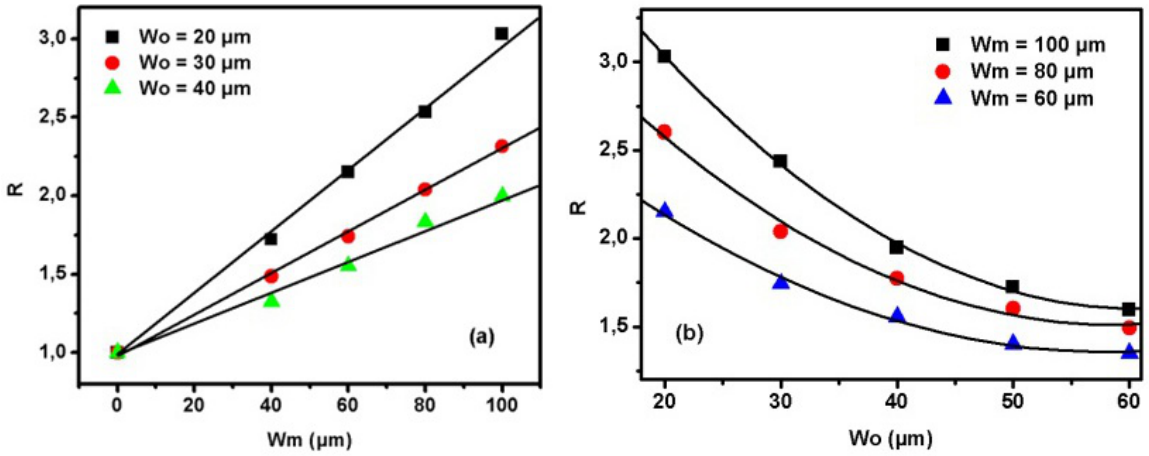

Figure 31: The growth rate enhancement R is plotted against (a) the width of the mask, Wm, and (b) the width of the opening between the masks, Wo.

3.4 Model of selective area growth

In this study a mathematical model, which predicts the shape of the selectively grown GaN microstructures as a function of D/k ratio is presented. A comparison is made between experimental results and the theoretical calculated profiles. The model is based on the vapor phase diffusion (VPD) model [12]. In this model, laminar flow is assumed and there exists a stagnant layer above the wafer surface. Gas phase diffusion of precursor molecules occurs vertically and laterally and leads to a growth rate enhancement in the vicinity of the masked area. The species concentration $C(x,y,z)$ around the mask is obtained by numerically solving the diffusion equation

in three dimensions.

$$D\nabla^2 C = 0 \tag{2.1}$$

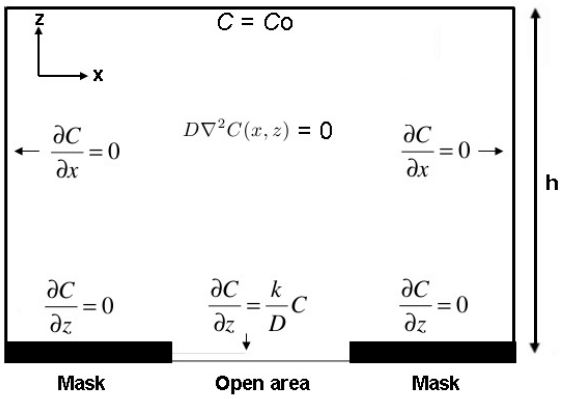

Figure 32: Schematic of the computational domain and boundaries conditions used in the three-dimensional dimensions VPD.

Figure 32 presents a schematic of the computational domain, governing equations and boundary conditions. At the top of the stagnant layer (h), the concentration of species is constant (infinite diffusion source)

$$C(h) = C_0 \tag{2.2}$$

The periodicity of the domain leads to the following condition for left and right boundaries:

$$(\frac{\partial C}{\partial x})_0 = 0 \tag{2.3}$$

Since there is no growth occurring on the mask, the flow is set to 0:

$$(\frac{\partial C}{\partial z})_0 = 0 \tag{2.4}$$

Finally on the wafer, the equilibrium between the reaction on the wafer and incident flow leads to the following mixed condition:

$$D(\frac{\partial C}{\partial z})_0 = kC_s \tag{2.5}$$

where k is the rate constant for the heterogeneous surface reaction, C_s is the gas-phase concentration of the reactant species at the interface with the surface, D is the diffusion coefficient in the vapor phase, C is the gas-phase concentration of the reactant species, x is the lateral dimension, and z is height above the surface. The ratio of effective diffusion length, D/k is the only adjustable parameter in the model. The best fit for GaN thickness profile is obtained when the D/k of Ga is set to be 13$\pm$1 μm. This value is comparable to 11.4 μm calculated by Coltrin *et al.* [41, 42]. Figure 33 shows the experimental and the simulation thickness profile on two different mask patterns, by using D/k = 13 μm as the simulation parameter. In this figure, the thickness profile is normalized with the reference thickness (far from any masked area).

The obtained value of D/k = 13$\pm$1 μm for Ga precursor is at least one order of magnitude less than typical D/k values reported for Ga used in selective growth of InGaAsP- and GaAs-based compound semiconductors [43]. We attribute this difference to a significant increase of the reaction coefficient k for formation of Ga-N bond at the (0 0 0 1) plane of GaN compared to that for Ga-As and Ga-P reaction rate for (0 0 1) plane of compound semiconductors.

3.5 Summary

In this chapter, we studied and optimized the growth conditions for GaN structures at the micrometer scale. A perfect selectivity on the SiO_2 masks has been obtained for mask widths less than or equal to 60 μm. The AFM shows a ribbon-shaped GaN

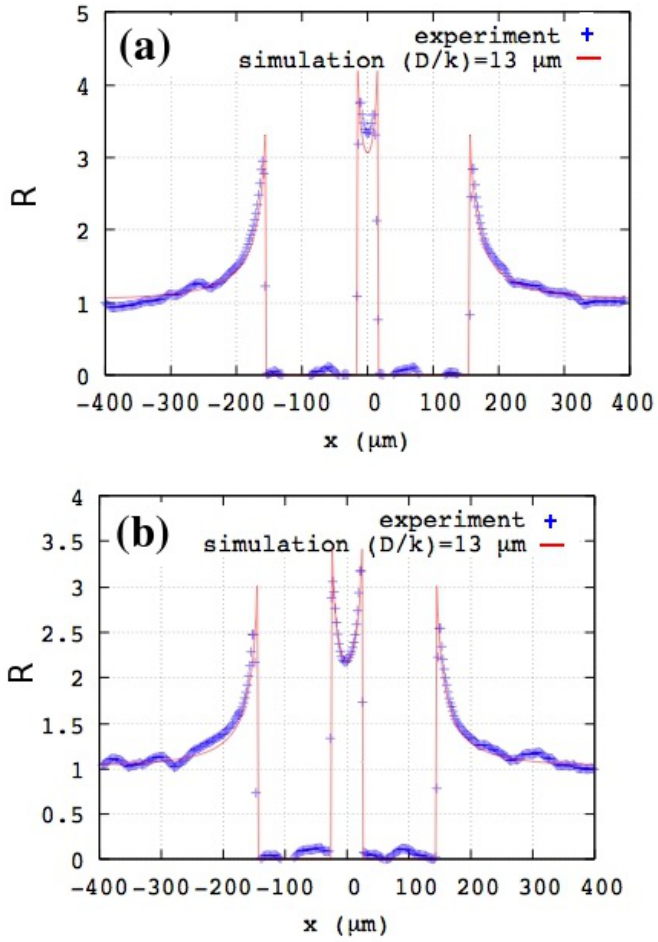

Figure 33: Cross-section normalized thickness profiles (measured and calculated) for two different mask patterns, (a) Wm = 140 μm, Wo = 40 μm, and (b) Wm = 120 μm, Wo = 60 μm. In both cases, D/k is set to 13 μm.

microstructure with smooth vertical facets and a smooth surface with rms roughness of 0.4 nm. White light interferometry has been used to measure the growth rate enhancement ratio. The growth rate enhancement ratio varies linearly with the mask width, Wm, and decreases with increase of the mask opening, Wo. These relationships show similarity to the results reported by others [12]. By fitting the simulated VPD model to the experimental results, the ratio of diffusion length, D/k is empirically determined to be 13 μm.. This value is comparable to 11.4 μm calculated by Coltrin *et al.* [41, 42].

CHAPTER IV

NANO SELECTIVE AREA GROWTH

4.1 Nano selective area growth on GaN template

By using the optimized growth conditions obtained in the previous study, we investigated the growth of GaN nanostructures by nano selective area growth (NSAG). A perfect selective growth was achieved successfully. Excellent surface morphology of the nanodots with homogeneous height and width was demonstrated. Growth morphology was studied by atomic force microscopy and scanning electron microscopy. The result is published in Materials Science and Engineering B [44]. It should be noted that the VPD model used to study micro-SAG does not apply to NSAG since the model neglects the effect of the surface migration, which plays a significant role in NSAG.

4.1.1 Experimental procedures

To fabricate a regular array of NSAG structures, a SiO_2 dielectric mask with a thickness of 140 nm was deposited on a (0 0 0 1)-oriented GaN template using chemical vapor deposition (CVD). After that, an array of the mask openings with a diameter of 80 nm were developed in the mask by using electron-beam lithography and reactive ion etching. Figure 34 shows the process for nano mask preparation by e-beam lithography used in this study. In the first step, a silicon dioxide layer is deposited on the wafer by plasma enhanced chemical vapor deposition. A layer of negative photoresist is subsequently spin coated on top of the silicon dioxide layer. The photoresist is illuminated by the e-beam lithography with the desired pattern in the third step. The portion of the negative photoresist that is exposed to e-beam becomes insoluble to the photoresist developer. Therefore, only the unexposed portion of the photoresist

is dissolved by the photoresist developer. Reactive ion etching is used to remove the silicon dioxide layer to expose the GaN layer underneath. These openings played the role of nucleation site for the GaN nanostructure growth. Finally the photoresist is remove by acetone bath. Figure 35 shows a SEM image of the patterned mask on the GaN template.

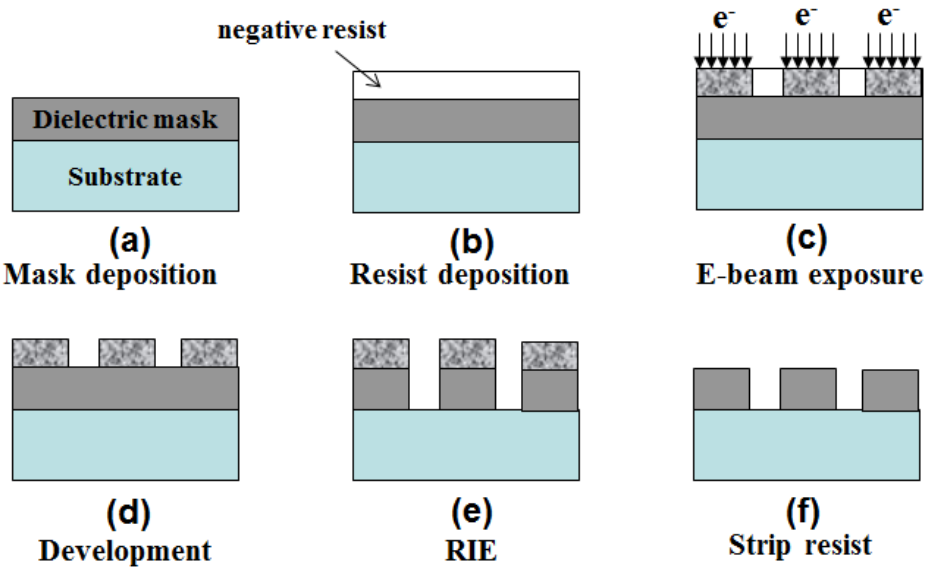

Figure 34: Process for nano mask preparation by e-beam lithography.

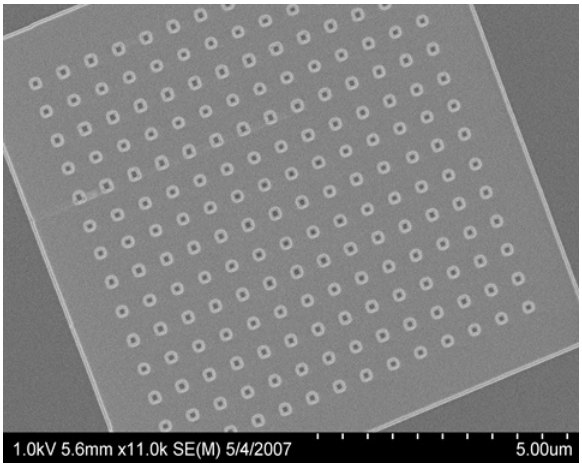

Figure 35: SEM image of the patterned mask on GaN template.

Prior to load the samples into the MOCVD system, the samplae is surface cleaned

by the following procedure:

- Put the sample in a beaker full of acetone and ultrasonic bath for 5 mins. Take the sample out and rinse with DI water.
- Put the sample in a beaker full of ethanol and ultrasonic bath for 5 mins. Take the sample out and rinse with DI water.
- Put the sample in a beaker full of DI water and ultrasonic bath for 5 mins.
- Put the sample in a beaker filled with acid sulphuric for 30 seconds. Subsequently thoroughly rinse with DI water.
- Put the sample on a filter paper and blow dry with N_2

The growth conditions used in this study are as shown in the following:

- temperature: 1000°C
- pressure: 1.33 kPa (100 Torr)
- V/III ratio: 4500
- growth rate: <1 μm/h
- carrier gas: nitrogen
- precursor: TMGa and NH_3

4.1.2 Growth and characterization of nanostructures

Epitaxial growth of nominal thicknesses of 200 and 400 nm were performed on a patterned substrate with periodic nano openings. Figure 36a shows a 30° tilted high resolution SEM image of a NSAG GaN layer on a patterned sapphire/GaN template substrate. It can be seen that perfect selective growth was obtained and the nanodots

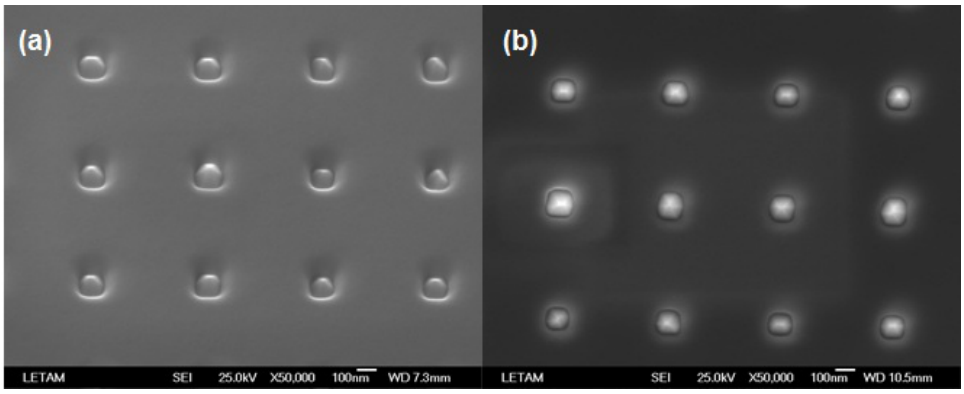

Figure 36: SEM image of GaN grown by NSAG (a) before removing the mask and (b) after removing the mask.

were completely confined in the opening of the mask. An SEM image of the sample after the mask is removed is shown in Figure 36b.

AFM measurements of the NSAG samples were performed before and after removing the dielectric mask. Figure 37a shows an SEM image before the mask was removed. It can be seen again that the growth was perfectly selective. Figure 37b shows a 5 x 5 μm^2 AFM image of NSAG GaN after removal of the mask. Nanodots with very smooth surface morphology and homogeneous in both width and height were obtained. Several patterns have been characterized, and the heights of the nanodots measured were between 70 to 100 nm. Figure 38 shows an AFM profile measurement across the nano-patterned area as well as the area far from the mask. The dips and the protrusions in this measurement correspond to the masked area and the GaN nanodots, respectively. The overgrowth at the edges of the mask was about 60 nm higher than the nominal thickness due to the migration of the precursors from the mask.

Unlike the micrometer scale SAG structures, there was no growth enhancement observed for the NSAG structures. This phenomenon was attributed to the fully developed pyramids with stable facets [45]. Both the 200 nm and 400 nm nominal thick NSAG layers result in the same height of the nanodots as shown in Figure

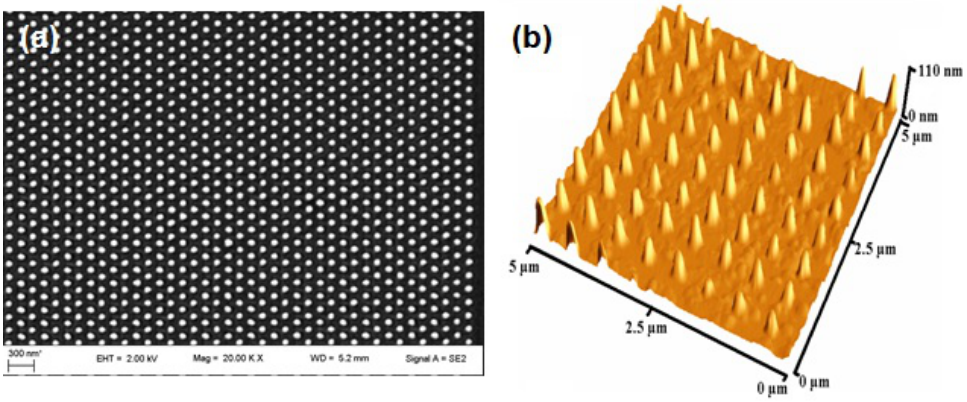

Figure 37: (a) SEM image of GaN nanodots grown by NSAG. (b) AFM image GaN nanodots after removing the mask.

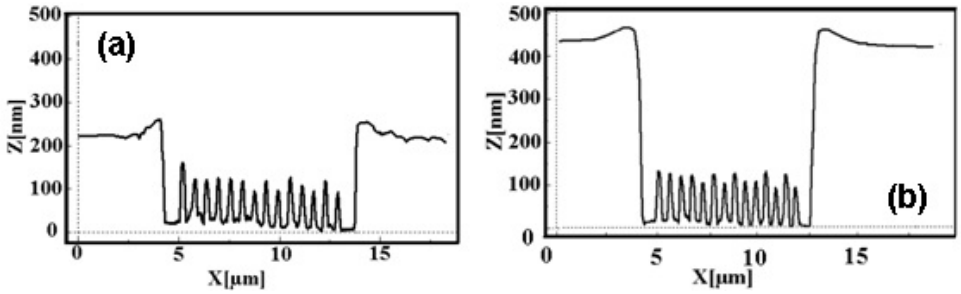

Figure 38: AFM profile measurement of NSAG across the dielectric mask with (a) 200 nm nominal thickness and (b) 400 nm nominal thickness.

38, which again confirms that the stable facets slow down the growth of pyramids. The height to width ratio of the nanodots was found to be 1, which indicates fully developed pyramids with facets of {1 -1 0 1}.

4.2 Nano selective area growth on highly lattice mismatched materials, nanoheteroepitaxy

The last part of the preliminary research was to perform nano selective area growth of GaN on highly mismatched substrates. GaN nanostripes and nanodots structures were successfully grown on both an AlN template and a SiC substrate. The influence of the growth condition and the mask orientation on the growth morphology were studied. Micro Raman studies showed improvement in crystal quality in the lateral overgrown nanostripes [46].

4.2.1 Experimental procedures

In this study, SiO_2 dielectric masks of 10 x 10 μm^2 with nano openings of 80 nm and nano stripes of 120 x 7600 nm^2 were prepared by e-beam lithography. The GaN growth was carried out in a MOVPE T-shaped reactor. The substrates were cleaned in a H_2SO_4 solution, and then rinsed in deionized water prior to growth. Nitrogen was used as carrier gas. Trimethylgallium (TMGa) and ammonia were used as the sources of gallium and nitrogen, respectively. The growth temperature was 1000°C. Two different growth pressure regimes were investigated: 100 and 450 Torr. The V/III molar ratio in the vapor phase was around 4500:1. To obtain high crystal quality and perfect selectivity, the growth rate of GaN was kept close to 1 μm/h in the unmasked part of the wafer. The structural properties of the grown materials were characterized by x-ray diffraction, atomic force microscopy, scanning electron microscopy, and micro-Raman mapping with a lateral resolution of 1 μm.

4.2.2 GaN nanostructures on AlN template

Figure 39 shows the SEM image of the patterned mask before a) and after the growth b). The fill factor of the nano opening pattern in this study is 0.0278. As shown in Figure 39b, perfect selective area growth with no random deposition of polycrystal on the mask was achieved. All the nanostructures were grown inside the nano openings as defined by the electron beam lithography and reactive ion etching. The GaN nanostripes in Figure 39b exhibit epitaxial lateral overgrowth in both the [1 1 -2 0] and [-1 -1 2 0] directions but not in the [1 -1 0 0] and [-1 1 0 0] directions. This phenomenon can be attributed to the different crystallographic planes at the growth front. Near the edges of the [1 -1 0 0] and [-1 1 0 0] directions, the growth front is decomposed into {1 -1 0 1} planes as observed in Figure 39b and confirmed by AFM measurements in Figure 39a and 39c. These planes are stable and tend to exhibit a slow lateral overgrowth rate [19]. On the other hand, the growth front along the [1 1

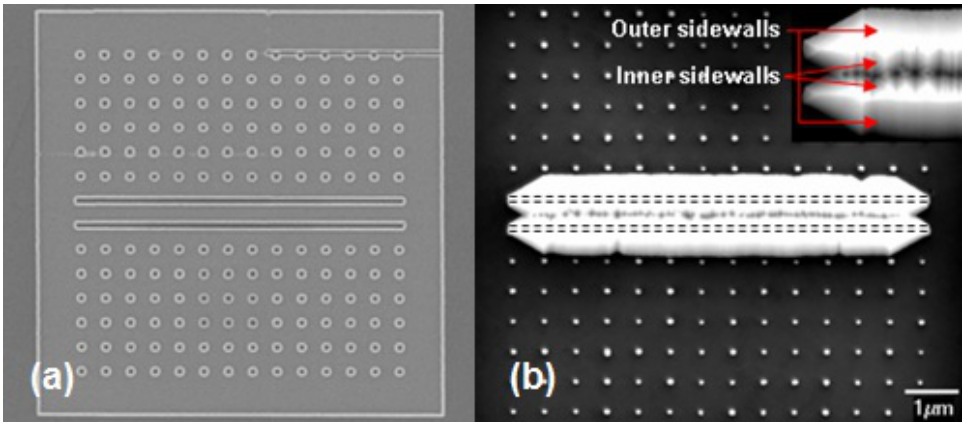

Figure 39: SEM images of the patterned mask on AlN/Al_2O_3 template (a) before and (b) after the growth of the GaN nanostructures. The dashed lines in (b) show the windows of the nanostripes that are filled by the GaN crystal. Inset shows the magnified view of the nanostripe structures with jagged sidewall.

-2 0] and [-1 -1 2 0] consists of {1 1 -2 n} planes. These planes are characterized by high lateral to vertical growth rates and hence they tend to laterally overgrow above the dielectric mask.

The growth front of the inner sidewalls between the two nanostripes exhibits jagged {1 -1 0 1} morphology as shown in the inset of Figure 39b. However, this phenomenon was not observed in the outer sidewalls of the nanostripes. We attribute this to the fact that the inner and outer sidewalls of the nanostripes receive different amounts of reactive species. The inner sidewalls received less reactive species from the surface migration and lateral vapor diffusion (higher effective filling ratio due to the lateral expansion) and consequently have a slower lateral growth rate with jagged {1 -1 0 1} facets. Conversely, the outer sidewalls received a larger amount of reactive species from the mask region and hence have a higher lateral growth rate. This phenomenon explains the different growth rate of the nanostripes in the [1 1 -2 0] and [-1 -1 2 0] directions as shown in Figure 39b (faster lateral growth rate for the outer sidewalls and slower for the inner sidewalls).

Figure 40 shows AFM measurements of the lateral growth nanostripes. In Figure 40a, different types of crystallographic facets that form a nanostripe can be observed.

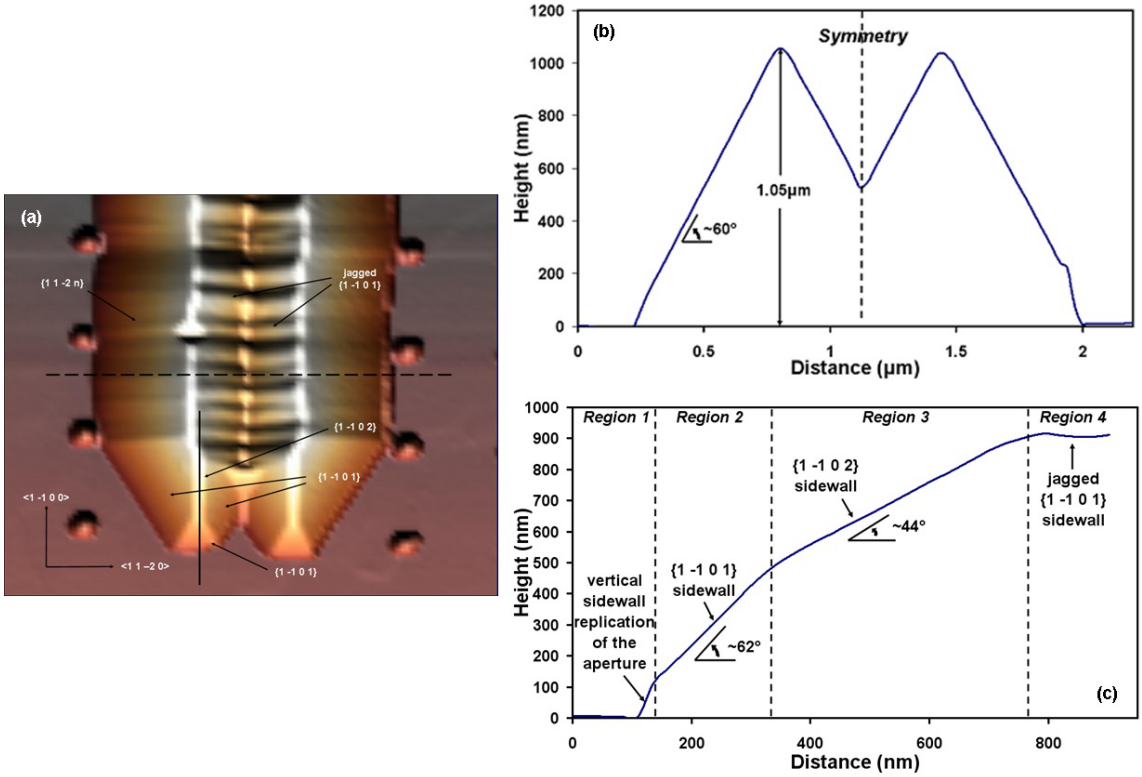

Figure 40: AFM images of the lateral growth nanostripes: (a) plan view of the nanostripes with various crystallographic planes; (b) height profile measurement across the nanostripes in the horizontal direction (dashed line in Figure 39a) and (c) height profile measurement across the nanostripes in the vertical direction (solid line in Figure 39a).

These facets consist of {1 -1 0 1}, {1 1 -2 n}, {1 -1 0 2}, and jagged {1 -1 0 1} facets. Figure 40b and 40c show the AFM profile measurements across the nanostripes in the horizontal (dashed line in Figure 40a) and the vertical (solid line in Figure 40a) direction respectively. As shown in Figure 40b, the two nanostripes with pyramidal cross-section coalesced together. The height of both nanostripes is around 1.05 μm and the slope of the outer sidewalls is around 60°. This slope angle corresponds to the {1 1 -2 n} facets where n is 1.88 (n = 2 when slope angle = 58.39°). As shown in Figure 40c, the AFM profile of the nanostripe can be divided into 4 different regions. The first region consisted of a vertical sidewall, which is the replication of the nano openings defined by electron beam lithography and reactive ion etching. This vertical sidewall showed some inclination from the vertical line as a result of the convoluted AFM tip. In the second region, a {1 -1 0 1} sidewall was observed with an angle around 62°. These stable facets have practically stopped the growth in both the [1 -1 0 0] and [-1 1 0 0] directions. The sidewall facet then became oriented {1 -1 0 2} in the third region. The change of the sidewall facet is to accommodate the different growth rates of each sidewall that contains the nanostripe. The fourth region consists of the jagged {1 1 0 -1} sidewalls.

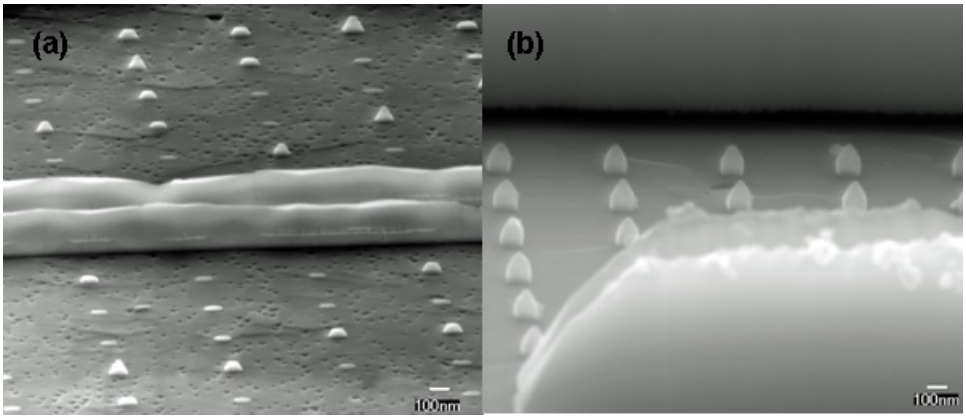

Figure 41: SEM angle views of GaN nanodots array after removing the mask. The thicknesses of the GaN layer on the unpatterned area are (a) 200 nm and (b) 1000 nm.

Figure 41 shows angle view SEM images on GaN nanodots grown for different

unpatterned area thicknesses (a) 200 nm and (b) 1000 nm. In Figure 41a, three types of nanostructures can be observed, complete pyramid structure, truncated pyramid with a smooth (0 0 0 1) top surface, and thin layer of 2D growth film with a smooth (0 0 0 1) top surface. The formation of these different nanostructures is probably due to the inhomogeneous diffusion of reactive species, and hence inhomogeneous growth rate for a relatively short growth time (200nm thickness on the unpatterned area). For the growth with 1000 nm thickness of unpatterned area thickness (Figure 41b), a uniform of GaN nanodots structure is obtained. In Figure 42a, a AFM profile of a single nanodot is shown. The top of the nanodot is a six sided {1 -1 0 1} pyramid, while the bottom of the nanodot is composed of six vertical {1 -1 0 0} facets that form a hexagonal prism. The height distribution of the nanodots is shown in Figure 42b. All the nanodots have a height of about 150 nm despite an inhomogeneous growth rate at the initial stage as shown in Figure 42a. It is important to emphasize that a precise control of location, diameter and height of each nanodots with a periodic array in long range order is very useful for integrated photonic crystal applications.

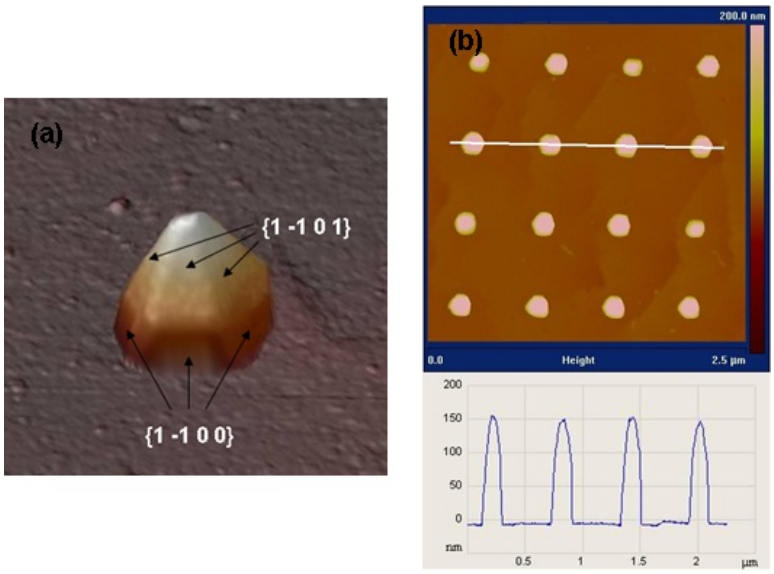

Figure 42: AFM images of (a) a single nanodot structure and (b) height distribution profile of 16 nanodots grown by NSAG. The thickness of the unpatterned layer is 1000 nm.

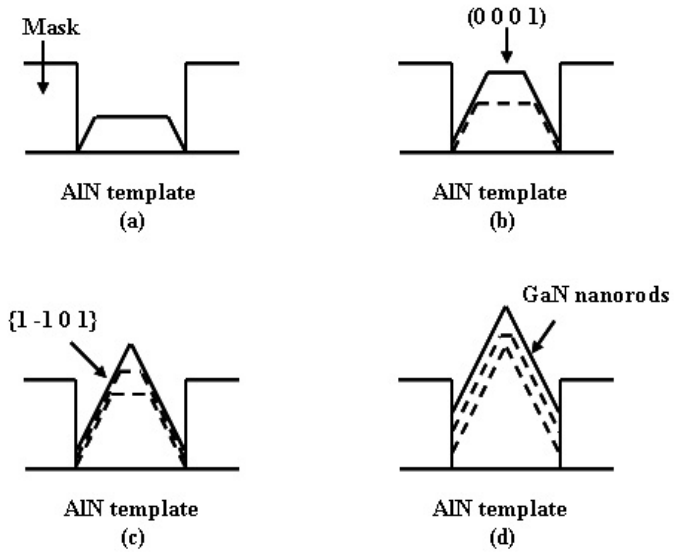

Figure 43: Schematic diagram of a proposed growth evolution of the GaN nanodot.

By examining the various morphologies that appear in the SEM images (Figure 41), we propose a growth evolution of the GaN nanodot as depicted in Figure 43. The growth starts as a 2-D thin film with a smooth (0 0 0 1) top surface as shown in Figure 43a. Further growth leads to the formation of a truncated pyramid structure with {1 -1 0 1} sidewalls and a smooth (0 0 0 1) top surface. As the truncated pyramid continues to grow, a complete pyramid is eventually obtained (Figure 43c). Any further growth will deposit on top of the {1 -1 0 1} sidewall and the growth front proceeds slowly in the vertical direction as shown in Figure 43d. The slow growth of the {1 -1 0 1} facets is the primary factor resulting in low selective area growth efficiency and homogeneous height distribution of GaN nanodots (Figure 41b) despite the inhomogeneous starting growth as shown in Figure 41a.

4.2.3 GaN nanostructures on SiC

Figure 44a shows a planar view of an SEM image of the mask that is prepared for the growth of nanodots and nanostripes on a 6H-SiC substrate. A regular array of nano openings with a uniform diameter of 100 nm as well as two nanostripes orientated

along the <1 1 -2 0> direction are prepared. The fill factor for the nanodots area, which is defined by the ratio of the open area to the whole area of the mask, is set to 0.028. Figure 44b shows NSAG of GaN nanodots and nanostripes grown in the nano openings of the mask at 100 Torr. A perfect selectivity is obtained at this growth condition as indicated by the absence of GaN polycrystal formed on the mask. Both the nanodots and nanostripes have smooth and homogeneous side walls and are completely confined inside the mask openings.

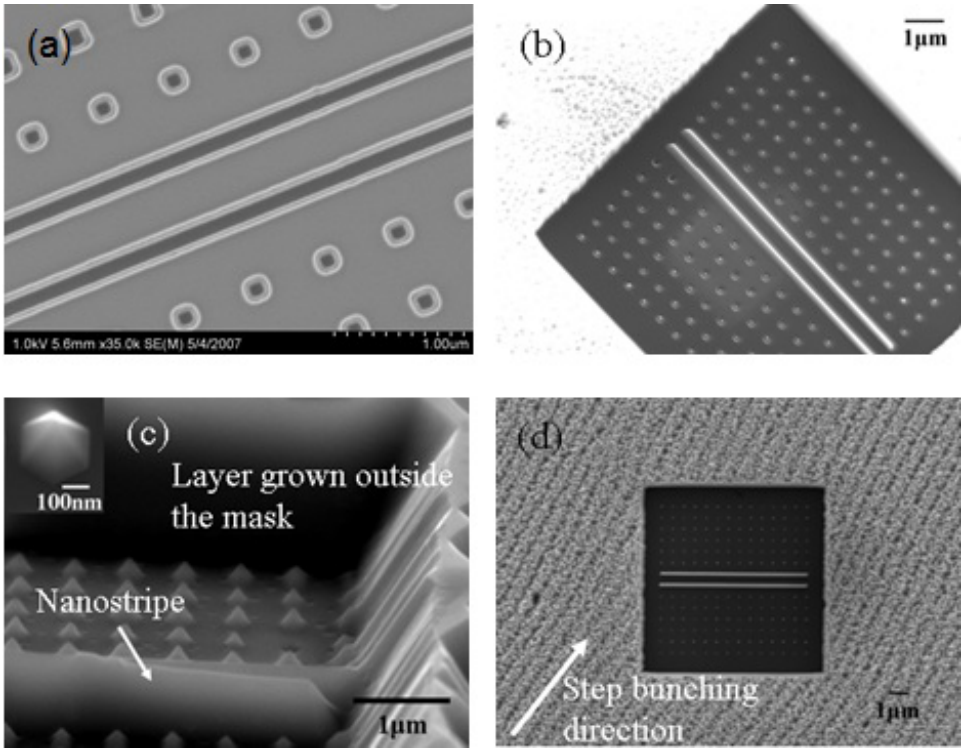

Figure 44: (a) SEM image of the mask before growth; (b) SEM image of the nanostructures grown on SiC substrate at 100 Torr; (c) High magnification SEM angle view image of the nanostructures and the growth on the non-masked area; (d) SEM planar view image compares NSAG grown structures in the mask openings and the step bunching effect for GaN grown on the planar 6H-SiC substrate.

Figure 44c compares higher magnification angle view SEM images of the nanostructures and the continuous GaN layer grown in the non-masked area. For both growth pressures of 100 and 450 Torr, the nanodots have a much smaller height

compared to the thickness of the continuous film in the non-masked area. This observation contradicts the expectation of growth rate enhancement, as observed in the micro-SAG structures [47]. Even in the case when the lateral size of the mask is smaller than the diffusion length D/k for precursors in the gas phase, the growth enhancement is expected in the SAG region due to formation of an excessive precursor concentration above the masked area. In the case of GaN growth, D/k is about 11 microns [42], which is comparable to the total size of the oxide mask (Figure 44a). We can see the growth enhancement regions at the edges of the continuous GaN film that surrounds the 10 x 10 μm mask, as expected from the gas phase diffusion model. However, instead of growth rate enhancement, we observed a significant growth rate suppression in both nanodot and nanostripe regions. This phenomenon can be explained by the growth inside the nano openings is suppressed due to formation of hexagonal pyramids, which are terminated by the {1 -1 0 1} facets. The growth rate at these facets is known to be much slower compared to that for the vertical growth in c-direction of GaN. In this scenario, the main factor determining the size of the dots in the NSAG region is not the fill factor of the mask, but the ratio between the nano opening and the typical size of the nucleation grains. For the nanostripe, we observed a four times faster growth rate compared to that for nanodot, which is still much less than the growth rate for continuous film. Since one of the in-plane directions was not confined in the nanostripe, the nucleation sites can coalesce in the direction along the stripe forming a faster growing c-plane terminated facet. This mechanism eventually promotes the growth in the stripe openings compared to nanodots as it is shown in Figure 44c.

Figure 44d shows a planar view SEM image that compares the growth in the masked and non-masked areas. A self-modulated growth profile that occurred at the planar substrate (non-masked area) is due to poor wetting of Ga on SiC surface [48], which suppresses the lateral growth of GaN on SiC surface while promoting the

effect of GaN bunching along the step ledges on the surface [49]. As shown in Figure 44d, NSAG provides a nanostripe growth along the direction determined by the mask orientation, which is not affected by the step bunching effect.

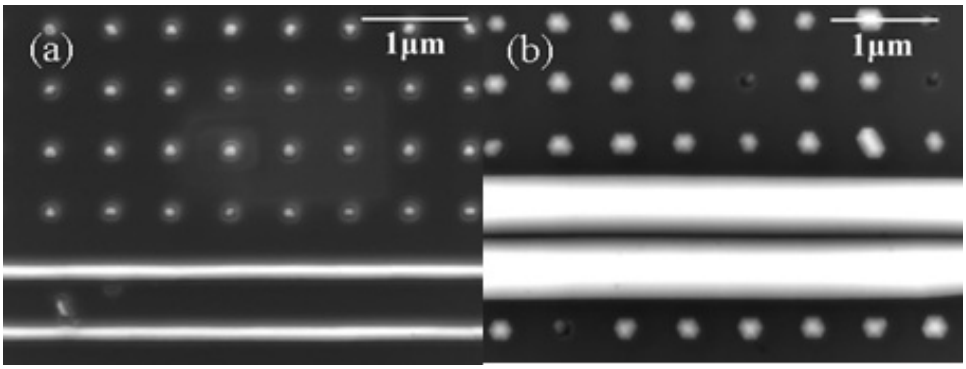

Figure 45: SEM images of GaN nanostructures on SiC substrate at (a) 100 Torr and (b) 450 Torr.

To realize the concept of ELO on the nano scale, the influence of growth pressure on the size and shape of the nanostructure was investigated. Figure 45 compares SEM images of the GaN nanostructures grown at 100 and 450 Torr. At lower growth pressure, the GaN nanostructures exhibited an excellent surface morphology for the top surface, which is terminated by six smooth {1 -1 0 1} facets. The growth was completely confined inside the mask openings with no lateral overgrowth even for the layer thickness twice larger than that shown in Figure 44d. However, at high growth pressure (450 Torr), the nanostructures showed epitaxial lateral overgrowth and an increase of the growth rate. The diameter of the nano pyramids grown at 450 Torr was about three times larger than that for the low pressure growth, as seen in Figure 45a and 45b. The increase in growth rate with reactor pressure can be explained in terms of the surface migration from the mask region. The gas residence time is increased at higher pressure and, hence, more reacting species are transported to the openings before being desorbed back to the gas phase. With increase of the growth time, the nanostructure grown at high pressure would eventually coalesce together forming a high quality thin film.

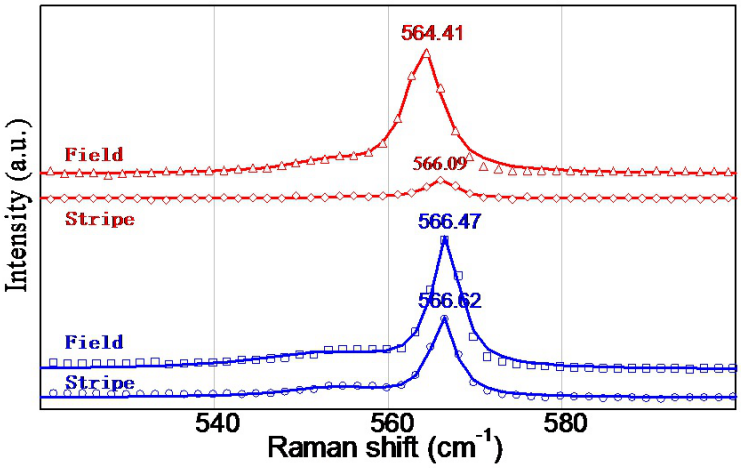

Figure 46: Raman spectra of GaN grown in the stripe opening and on the unpatterned are at 100 Torr (red) and 450 Torr (blue). The symbols are experimental obtained data while the lines are curve fit of the experimental results.

A backscattering z(-,-)z Raman scan of GaN grown in the stripe opening and on the filed layer at different reactor pressure is shown in Figure 46. In both cases the E_2 phonon mode of GaN nanostripe are blue-shifted when compared with the continuous grown GaN film. The Raman intensity of the nanodot is too low and hence no comparison is made in this study. Table 6 summarizes the E_2 mode frequencies and the biaxial stress determined in GaN thin film grown on planar SiC substrate and nanostripe at low and high pressure respectively. The strain-free GaN E_2 mode frequency is taken to be 567.0 cm^{-1} [50].The biaxial stress was calculated from the frequency shift by using the proportionality factor of 4.2 $cm^{-1}GPa^{-1}$ for wurtzite GaN [51]. The biaxial stress measured in the GaN grown on planar SiC substrate is in tensile as confirmed with x-ray diffraction. The seeming relaxation of the GaN thin film grown on planar SiC substrate at high pressure growth as compared to low pressure can be attributed to the difference in thickness as measured by AFM (1.2 μm for 450 Torr and 500 nm for 100 Torr). However, despite the thickness of the GaN grown on planar SiC substrate being much more than that for the nanostripes (Figure 44c), the nanostripes are still more relaxed than the GaN grown on planar

Table 6: E_2 mode frequency and biaxial stress measured in GaN thin film grown in the nanostripe opening and on the planar SiC substrate at low and high growth pressure.

Sample structure	E_2 frequency (cm^{-1})	Biaxial stress (GPa)
GaN on planar SiC (low pressure)	564.41	-0.62
GaN on planar SiC (high pressure)	566.47	-0.13
GaN nanostripe (low pressure)	566.09	-0.22
GaN nanostripe (high pressure)	566.62	-0.09

SiC substrate for both low and high pressure growth. This phenomenon was due to the three dimensional stress relief mechanisms of the nanostructure [24]. An average frequency shift of about 1.68 cm^{-1} was observed for the nanostripe as compared to the film grown on planar SiC substrate at low pressure, which corresponds to 0.40 GPa of relaxed strain. At high growth pressure the E_2 mode frequency is close to the strain-free GaN E_2 frequency, indicating a quite complete relaxation of the residual strain in the nanostripe, which is correlated to the lateral overgrowth regime as shown in Figure 44b. The results indicate, on one hand, relaxation of the strain inside the stripe and, on the other hand, relaxation of the strain for both the high pressure grown thin film and nanostripe.

4.3 Analysis of strain relaxation in GaN nanostructures using submicron beam X-ray diffraction

Progress in this emerging field of nanotechnology depends heavily on utilization of advanced material characterization tools, such as synchrotron radiation high resolution submicrobeam x-ray diffraction [52, 53], which has been recently applied to various materials systems and device structures, demonstrating the capability to measure strain relaxation at the sidewalls of micron-wide waveguide ridges and to reveal details of inter- and intrafacet surface migration effects [53]. Currently, there is substantial interest in knowing the variation of structural properties across nanostructures that is being satisfied by combining techniques such as high-resolution x-ray diffraction and

reciprocal space mapping (RSM), with real-space mapping on the nanoscale [53, 54].

In this study, we apply nondestructive synchrotron-based submicron beam XRD with a spatial resolution of 240 nm along with RSM to determine the strain and (0 0 0 1) planar tilting in GaN nanodots and nanoridges. The observed trends in strain and tilt of the nanostructures match those previously observed for microstructures [53], and suggest an explanation for the mechanism behind 3D stress relaxation effects inherent in heteroepitaxy.

4.3.1 Experimental procedures

XRD characterization of the nanostructures was carried out using synchrotron radiation with x-ray energy of 10.4 keV at the 2-ID-D micro-diffraction beamline at Advance Photon Source (APS) (Figure 47a). Synchrotron radiation was focused using a zone plate producing a quasi-circular spot with a FWHM of r $\approx$ 240 nm. The angular resolution for θ and χ was limited by the 180 arc sec divergence of the focused beam. Samples were mounted on an XYZ stage, which enabled lateral (X-Y) mapping for the XRD measurements. The position of the x-ray beam on the sample surface was controlled with 50 nm precision by simultaneous monitoring of the Ga-K fluorescence from the nanostructures. Diffracted intensity was collected by a large-area CCD detector positioned on the 2θ arm of a diffractometer. The inter-pixel distance and, hence, the resolution along the 2θ direction corresponded to $\sim$8 arc sec. In the following we will present results for (00.4) symmetric reflections measured for nanodots and nanoridges; the latter have been oriented along the diffraction plane. By monitoring Ga-K fluorescence, which originated from NSAG structures and was absent in the substrate, we can track the relative position of the nanostructures with respect to the focused x-ray beam.

The experimental Bragg peaks for 6H-SiC and sapphire were used to calibrate the measured values of 2θ and χ for the GaN nanostructures. For simplicity of

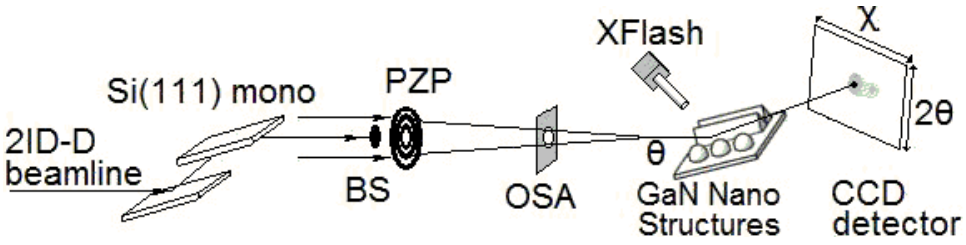

Figure 47: Experimental setup. Si(1 1 1) mono-silicon monochromator; BS-gold beam stop; PZP-phase zone plate; OSA-order sorting aperture; XFlash-fluorescence detector.

Table 7: Growth conditions and measured strains for the samples.

				Strain (±0.0003)		
Sample	Substrate	Pressure (Torr)	Field thickness (nm)	Dots	Ridges	Field
1	6H-SiC	450	400	-0.0004	-0.0005	-0.0006
2	6H-SiC	100	400	-0.0011	-0.0012	-0.0015
3	AlN	450	600	-0.0003	-0.0005	0.0000

data representation, strain was re-calculated with respect to the accepted lattice parameters for bulk GaN from Ref [55]: cGaN = 0.5185 nm. Reconstruction of the diffracted intensity distribution around the (00.4) reciprocal lattice point in three-dimensional reciprocal space was done by acquiring multiple CCD images at different θ angles around θ_{Bragg}. The two axes of the CCD frame correspond roughly to 2θ and χ angles. For each pixel of the measured CCD frames, the $\{\Delta\theta, \Delta 2\theta, \chi\}$ coordinate system has been transformed into relative reciprocal space coordinates $\{\Delta q<10.0>, \Delta q<01.0>, \Delta q<00.1>\}$ using standard transformations [39]. Strain along q<00.1> (c-direction) has been presented in terms of the d-spacing mismatch and calculated as $S = (q_{bulk} - q_{nano}) / q_{nano}$, where q_{bulk} is the value for bulk GaN and q_{nano} is the measured value for the nanostructures.

4.3.2 Results and discussion

Sample properties are summarized in Table 7. Figure 48b shows an X-Y map of the diffracted intensity collected from the nanodots region for sample 3 at the (00.4) Bragg conditions with a fixed value of the θ angle. The peaks of intensity in Figure 48b

correspond to the nanodot positions. Note correlation with the SEM image (Figure 48a) of the same sample. Variations of the diffracted intensity between different nanodots are due to minor planar misorientation. Figures 48c and 48d show an SEM image of sample 2 and an AFM image of sample 1. Note that the high pressure samples (sample 1 and sample 3) exhibit significant lateral overgrowth which causes their ridge structures to partially coalesce.

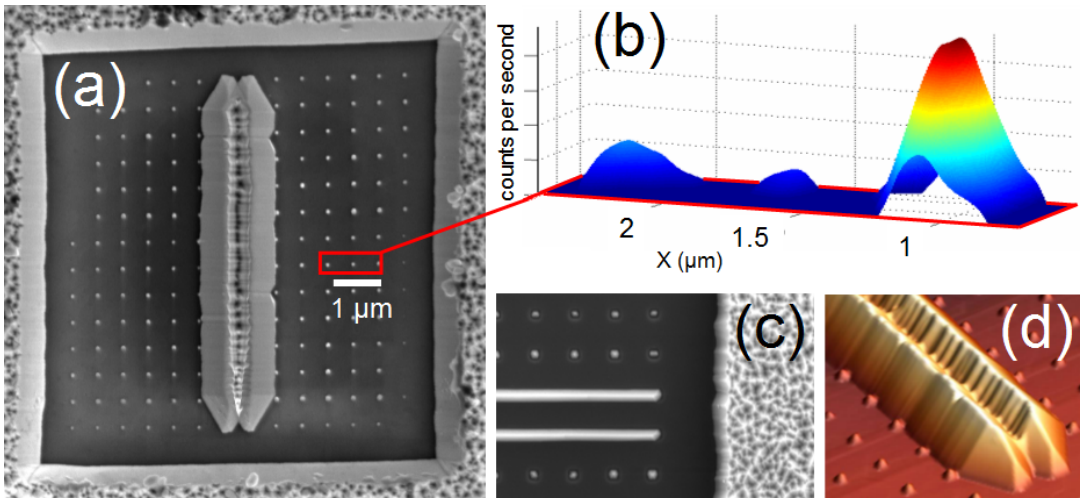

Figure 48: (a) SEM image of sample 3. (b) X-Y map of the diffracted intensity collected from the nanodots region. Background is subtracted and θ is optimized for the rightmost nanodot. (c) SEM image of sample 2. (d) AFM image of sample 1.

Figure 49a shows evolution of the diffraction signal distribution measured at the Bragg conditions for different positions of the x-ray beam across the GaN field, nanodots, and nanoridges in sample 1. In the nanodots region [beam positions (ii), (iii)], the tilt effect is not discernable and, hence, the (0 0 0 1) planes of nanodots are roughly parallel to the substrate. Note that the field part (i) of the structure has the same behavior. However, when the beam is scanning across the nanoridges [beam positions (iv)-(vi)], we see five signals distinct in χ. Figure 49c shows reconstruction of the plane orientations for the double-nanoridge structure. In the central part, where ridges merge, the tilt is strictly zero, while at either side, both ridges tilt away from the center by about 0.3 deg, and the (0 0 0 1) planes are tilted with respect

to this angle. The strong $\chi = 0$ signal throughout the structure, especially in the central part of each ridge, indicates a strong presence of untilted planes, suggesting that the planar tilting occurs mostly near the sidewall surfaces and that the bulk of the structure is comprised of untilted planes. Figure 49b shows the same measurements for the low-growth-pressure sample (sample 2). For the same relative beam positions we observe a similar tilting of the (0 0 0 1) planes in the nanoridges. Meanwhile, the signal from the nanodots looks and evolves in the same way as in the first sample. The nanoridge structure of sample 3 is almost completely fused, causing the diffracted signal to be smeared in χ (FWHM = 0.55 deg), indicating a continuous, 'bowed' configuration of the (0 0 0 1) planes.

Thus, we have observed an effect of crystallographic (0 0 0 1) planar tilting for the nanoridges. This result can be compared to the previously measured effect in significantly larger GaN microridges (10 μm wide)[53]. While the absolute effect in microridges is much stronger, the tilting rate of $\Delta\chi/\Delta X = 0.6$ deg/μm holds for both systems. We conclude that this planar tilting effect is a general feature of heteroepitaxialy grown GaN nano and micro structures with smooth free-standing sidewalls. Sample 3 ridges, which are much larger, exhibit smooth planar bowing just like GaN microridges6 while the SiC samples have planar discontinuity at the ridge centers. This suggests that this discontinuity disappears as the ridge centers become further removed from the sidewall surfaces where the tilting takes place. Presumably, the (0 0 0 1) planes in the nanodots also undergo tilting, but they are too small laterally for our set up to distinguish tilted signal from the untilted signal. Yet unpublished results on micro hexagons show a radially dependant tilting rate of $\Delta\chi/\Delta X = 0.12$ deg/μm.

Figure 50 shows 3D reconstruction of the diffracted signal around the (00.4) reciprocal lattice point for the two types of nanostructures on both SiC samples. Isointensity surfaces are elongated in the plane perpendicular to (0 0 0 1) due to the

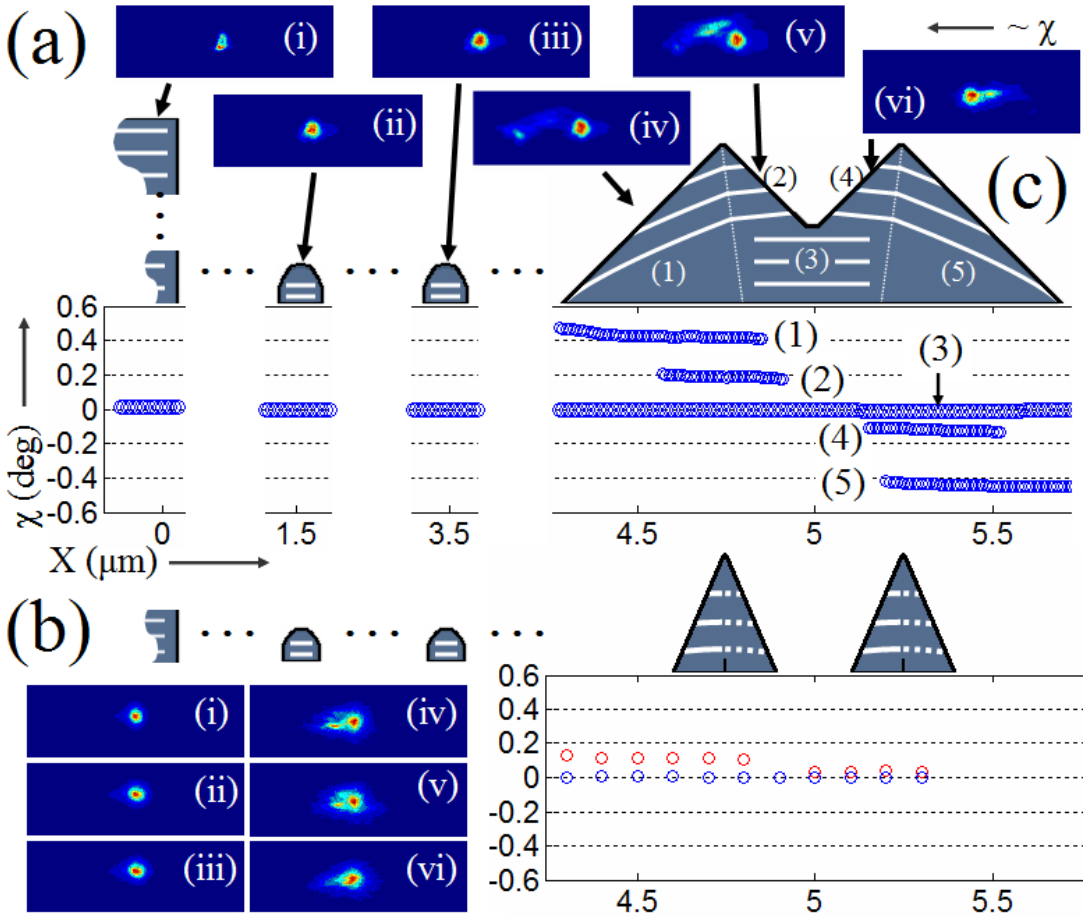

Figure 49: (a) Diffraction signal distribution for different positions on the field, nanodots, and ridges for the high-pressure sample 1. (b) The same measurements for the low-pressure sample 2. (c) Qualitative reconstruction of the planar tilting. Numbers (1-5) correspond to different segments of the experimental dependencies of the experimental χ signals in (a) and each describes a distinct continuum of planar tilting.

momentum spread of the focused x-ray radiation. However, the relative position of the centers of mass for these two figures along the <00.1> direction is not affected by that and indeed corresponds to the lattice parameter difference along the c-axis. A summary of strain data is presented in Table 7. Note that the GaN nanostructures are already quite relaxed, owing to misfit dislocation at the nucleation site [56]. We see that c-axis strains between nanodots and nanoridges in all samples are comparable within our resolution, and that the field, which is the continuous GaN film surrounding the mask area, is more strained in the SiC samples. Sample 3 was grown

with a very rough field comprised of an irregular array of free-standing structures, so it is expected (and intended) that it has a very small strain. We note that even though there is a difference in strains between samples, this difference does not affect the rate of planar tilting. We also note that the tilted planes are more relaxed than the untilted planes (Figure 50b). While this effect is within our strain resolution, it is seen in all tilted ridges and is corroborated by the results with micro-ridges, where strain resolution was not an issue [53]. Thus we can propose a mechanism of strain relaxation that involves re-orientation of the (0 0 0 1) planes.

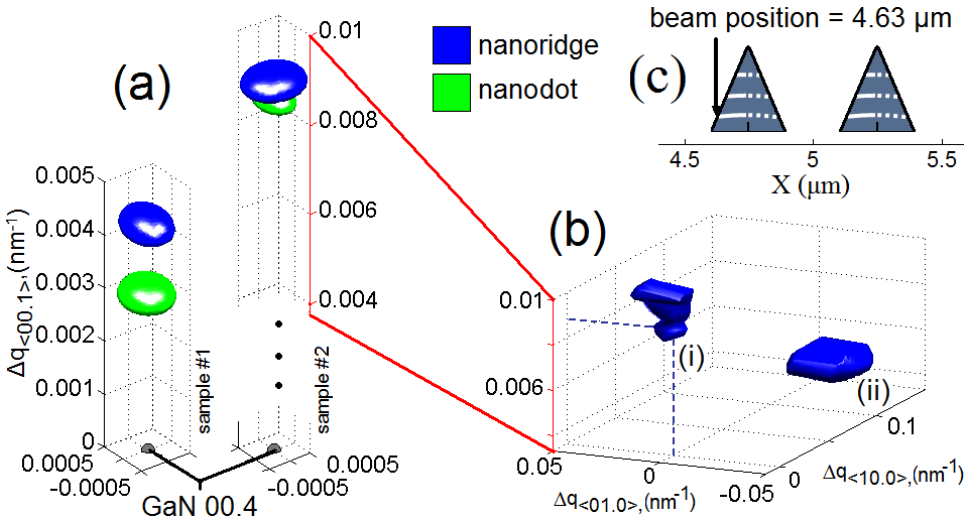

Figure 50: (a) Iso-intensity surfaces at the level of 99.9% of the maximum intensity of the 3D signal distribution for the nanodots (green) and nanoridges (blue). Data represents an average for signal from all nanostructures of that type measured per sample. For the ridges, only signal from the untilted planes is considered. The Δq axes are relative to the 00.4 reciprocal lattice point of theoretical bulk GaN. (b) Iso-intensity surface at the level of 50% of the maximum intensity of the 3D signal distribution for a position on a nanoridge of sample 2. (i) is the main signal from the substrate-aligned (0 0 0 1) planes, and (ii) is the secondary signal from the tilted (0 0 0 1) planes. (c) The position on the nanoridges where the signal in (b) was collected.

4.4 III-nitride nanodots, nanowires and multi quantum wells

Low dimensional nitrides structures such as quantum dots (QDs) have attracted much attention for light emitting devices such as laser diodes due to the enhanced carrier

confinement and to temperature stability of the threshold current [57]. In addition, the strong exciton binding energies in the nitride compounds make them suitable for single-dot emitters. However, these applications require QDs with homogeneous size distribution, a precise control of position, and a high areal density of dots, which cannot be provided by self assembly in the Stranski-Krastanow growth mode [58]. Additionally, it has been reported that quantum well structures grown on non-polar or semi-polar GaN facets show a reduced piezoelectric field effect [59, 60]. However, non-polar or semi-polar layers grown on foreign substrates such as r-plane sapphire and m-plane SiC typically have very high densities of stacking faults and defects [61, 62].

Recently, selective area growth (SAG) has been shown to be a powerful approach to grow not only QDs [63, 64] at the apex of a pyramid but also quantum well structures on semi-polar planes [65, 66]. Until now, most of the reported QDs and quantum wells have been produced by SAG with a typical in-plane size on the micrometer scale. SAG on the nano scale on the other hand offers advantages such as a 3-D stress relief mechanism [25], extremely low defect density, an increase of the areal density of the dots and an increase of the light emitting area. In this section, we present the nanodots, nanowires, and semi-polar quantum well structures produced by nano selective area growth. Their structural and optical properties will be discussed.

4.4.1 Experimental procedures

Similarly, the NSAG of GaN-based materials are performed in the MOVPE T-shaped reactor. First, a SiO_2 dielectric mask with a thickness of 100 nm is deposited on a (0001)-oriented GaN/Al_2O_3 template using chemical vapour deposition. The thickness of GaN is 3.5 μm and the threading dislocation density is 5 x 10^8 cm^{-2}. Electron-beam lithography and reactive ion etching are then used to pattern the SiO_2 mask on the template. The nano-openings are 80 nm in diameter and the windows of the

nano-stripes (0.12 μm x 7.6 μm) are defined in two different directions, <1 -1 0 0> and <1 1 -2 0>. The nano-openings and nano-stripes act as the nucleation sites for the subsequent growth of the GaN nano-pyramid and nano-ridge structures respectively. The MOVPE growth is carried out under nitrogen ambient. Trimethylindium, trimethylgallium, trimethylaluminum, and ammonia are used as the sources of indium, gallium, aluminum, and nitrogen, respectively. The total reactor pressure is fixed at 13.3 kPa. The growth rate is kept relatively low to obtain a high crystal quality and perfect selectivity.

The growth starts with NSAG of GaN at 1000°C until the faceted pyramid and ridge structures are obtained. This growth is then followed by either AlGaN/GaN layers (grown at 1000°C) or InGaN/GaN layers (grown at 800°C) deposited at the top of the nano-pyramids and nano-ridges. To study the growth evolution of the AlGaN/GaN nanostructure, AlGaN thin layers are occasionally deposited for 1 minute to act as a marker. The first few AlGaN markers are deposited during minutes 3, 6, 11, and 16 of the growth. The subsequent AlGaN markers are grown every 15 minutes. The surface morphology of the faceted nanostructures is characterized by scanning electron microscopy. Cross-sectional TEM and synchrotron based submicron beam X-ray diffraction are used to study the structural properties. Room temperature spot mode cathodoluminescence is used to characterize the optical properties of the nanostructures.

4.4.2 Optical and structural properties of III-nitride nanodots, nanowires and multi quantum wells

Figure 51 shows the SEM images of a nano-pyramid and several nano-ridges grown by NSAG. The selectively grown structures are very well faceted because of the anisotropy of the growth rate along different crystallographic planes. For the nano-pyramid, the growth fronts consist of six {1 -1 0 1} facets. The AFM measurements (not shown here) show that the dimensions of the pyramids and ridges are uniform

over the whole patterned area.

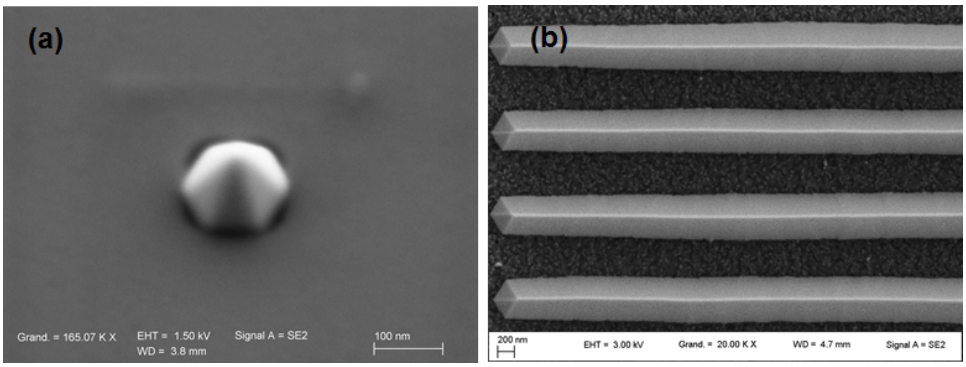

Figure 51: SEM images of a hexagonal nano-pyramid and several <1 1 -2 0> oriented nano-ridges grown by NSAG.

To investigate the threading dislocations and the growth evolution of the nanostructures, TEM has been employed. A bright field TEM image of a nanostructure is presented in Figure 52a. This TEM image shows the absence of threading dislocations in the nanostructure grown by NSAG. The reduction of dislocation density in the nanostructure is due to the small size of the openings (on the order of a few nanometers), which causes most of the threading dislocations in the template to be interrupted by the dielectric mask as shown in Fig 52a. The growth evolution of the nanostructure (nano-ridge and nano-pyramid) is studied by high angle annular dark field (HAADF) TEM. The growth starts with the formation of a truncated pyramid structure as shown by the AlGaN markers in Figure 52b. The growth rate in the c-plane direction is higher than the growth rate on the side facets. This leads to the formation of a complete pyramid with six {1 -1 0 1} facets. After the nano-opening is filled, the growth becomes laterally over the top of the dielectric mask while maintaining the pyramidal shape.

A HAADF TEM image of the AlGaN/GaN NSAG structure is shown in Figure 53. The thickness of the AlGaN layers has been estimated from the TEM image to be about 2.5 monolayers or ∼0.65 nm. The growth is highly uniform and the image contrast shows a sharp and flat interface between AlGaN and GaN epilayers.

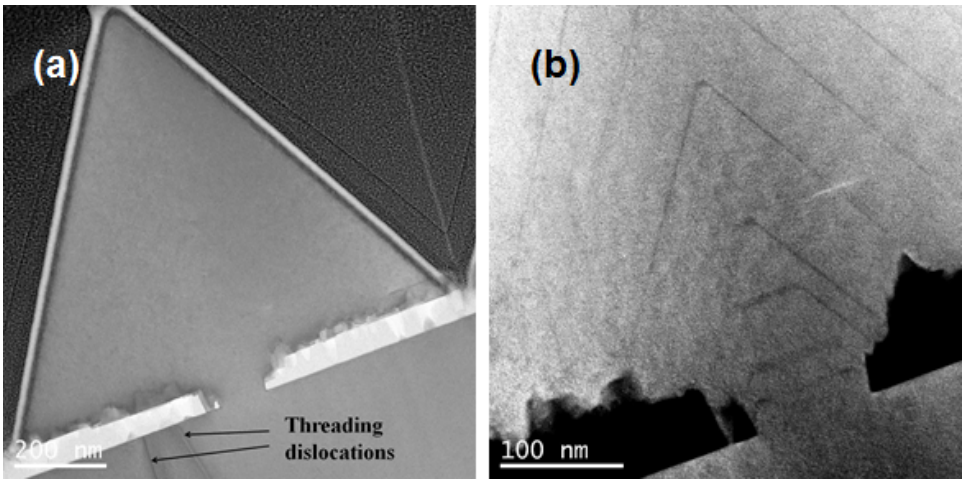

Figure 52: (a) Cross-sectional bright field TEM image of AlGaN/GaN grown on a nano-ridge showing absence of threading dislocations in the nanostructure. (b) Cross-sectional HAADF TEM image near the nano-opening showing the growth evolution of the nanostructure by NSAG.

The nanodots and nanowires form at the top of the nano-pyramid and nano-ridge, respectively. The nanowires grown on the nano-ridge are very homogeneous in size with the height of about 2.5 nm and width of 6 nm as shown in Figure 53. EDX shows about 8% aluminum incorporation at the apexes of both the nano-pyramid and nano-ridge.

To further investigate the structural properties and the incorporation of aluminum in the nanostructure, synchrotron based submicron beam XRD has been used to characterize individual AlGaN nanostructures, which were grown under the same growth conditions. Figure 54 shows the asymmetric reflection (1 0 . 5) reciprocal space map of the AlGaN nano-ridge structure grown by NSAG. The AlGaN nanostructure is found to be elastically strained. Based on the angular positions of the diffraction peaks, the structural parameters of the AlGaN nanostructure have been calculated. The average aluminum atomic content both in the nanostructure and in the unpatterned area is found to be around 5%, which is lower than the composition found at the apexes of the nano-pyramid and nano-ridge.

The HAADF TEM image of five InGaN MQWs grown on the semi-polar plane

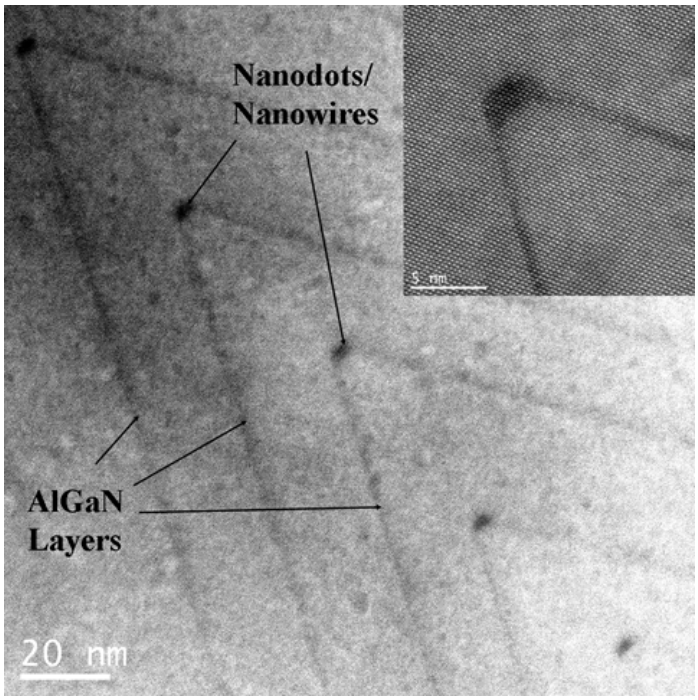

Figure 53: Cross-sectional HAADF TEM image of AlGaN/GaN layers grown on a nano-ridge showing sharp interfaces between the AlGaN and GaN epilayers and uniform growth. Inset shows a nanowire grown at the apex of a nano-ridge. The height and width of the nanowire is estimated to be 2.5 nm and 6 nm, respectively.

of a GaN nano-pyramid is shown in Figure 55a. Unlike in the AlGaN/GaN growth, no clear evidence of quantum dot formation is observed at the apex of the nano-pyramid. We also found that the growth facets of two different Miller's indices are formed on the InGaN/GaN nano-ridges. Figure 55b shows growth facets of (1 -1 0 1) originating at the bottom of the nano-ridges and intersecting with the other growth facets of higher Miller's indices that extend to the top of the nano-ridges. Up to now, the reason for this formation of higher Miller's indices growth facets is not known. EDX analysis shows that as high as 10% of indium has been incorporated at the intersection of the growth facets while only 6% of indium has been incorporated in the InGaN MQWs. This phenomenon can be attributed to the surface modifications (intersection of growth facets) that lower the chemical potential of nucleation. Note that the high accumulation of indium at the intersection of the growth facets is

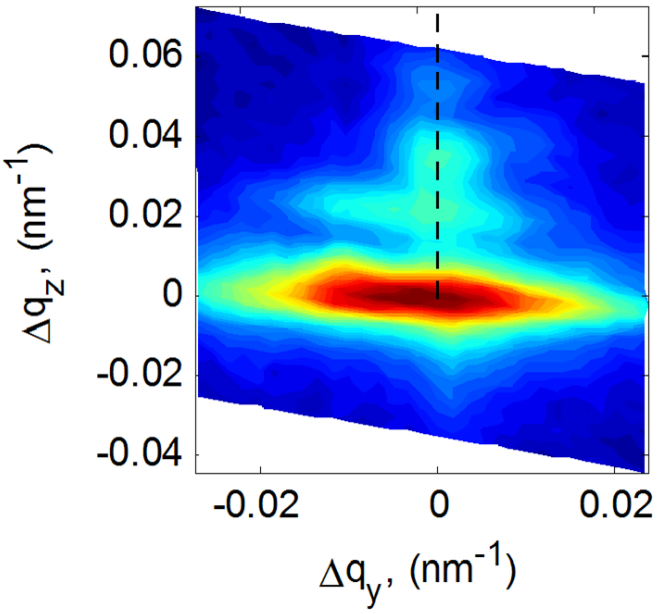

Figure 54: (10.5) reciprocal space mapping of a AlGaN nano-ridge structure grown by NSAG. The strong peak in the center of the map corresponds to the GaN substrate. The signal from AlGaN consists of a weaker layer peak (right above the GaN peak) and the thickness fringes. The incorporation of aluminum on the nanostructure has been estimated from the separation in reciprocal space between GaN and AlGaN peaks to be 5%.

essentially equivalent to formation of a quantum wire structure along the nano-ridge direction.

The optical properties of InGaN MQWs were investigated by room temperature CL spectra, as shown in Figure 56. A strong emission at 422 nm and a weak broad emission close to 600 nm are observed from the InGaN MQWs grown by NSAG. The weak broad emission is due to the surface related defect from the nanostructure [67]. The wavelength of CL emission from the unpatterned area is 436 nm. The intensity from the InGaN MQWs grown on the nanostructure is a few times higher in magnitude than the emission from the InGaN MQWs grown on the unpatterned area. The enhancement in CL emission is mainly attributed to a reduction in the non-radiative recombination centers associated with threading dislocations as confirmed by the TEM results. However, the cause of the small blue shift from the MQWs

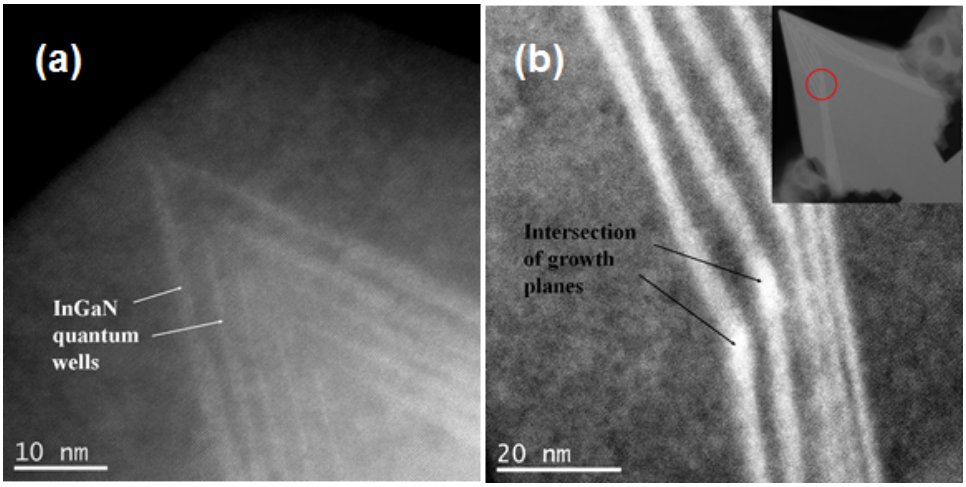

Figure 55: (a) Cross-sectional HAADF TEM image of five-period InGaN/GaN MQWs grown on a semi-polar facet of the nano-pyramid. No clear evidence of quantum dots is observed at the top of the nano-pyramid. (b) Cross-sectional HAADF TEM image of InGaN/GaN MQWs showing change of growth facet close to the top of the nano-ridge. Inset shows the place where the intersection occurs. EDX analysis shows higher indium mole fraction at the intersection of the growth facets compared to the average value for the MQWs.

grown on the nanostructure is still unclear and further investigation will be required.

4.5 Summary

In this chapter, we have studied NSAG on both lattice matched (GaN) as well as highly lattice mismatched (SiC and AlN) substrates. A perfect selectivity growth of the GaN has been obtained. The nanodots and nanostripes have excellent surface morphology with very smooth surface side walls. We demonstrated that our technique allows the growth of nanostripes along any in-plane crystallographic direction without any influence from the step bunching effect that occurs on the planar substrate. By varying the reactor pressure, growth of isolated nanostructures or epitaxial lateral overgrowth structures can be obtained. The lateral overgrowth nanostripes are almost completely relaxed, while the confined nanostripes are more relaxed than the GaN thin films grown on planar substrates.

We applied a nondestructive approach combining RSM and real-space mapping for

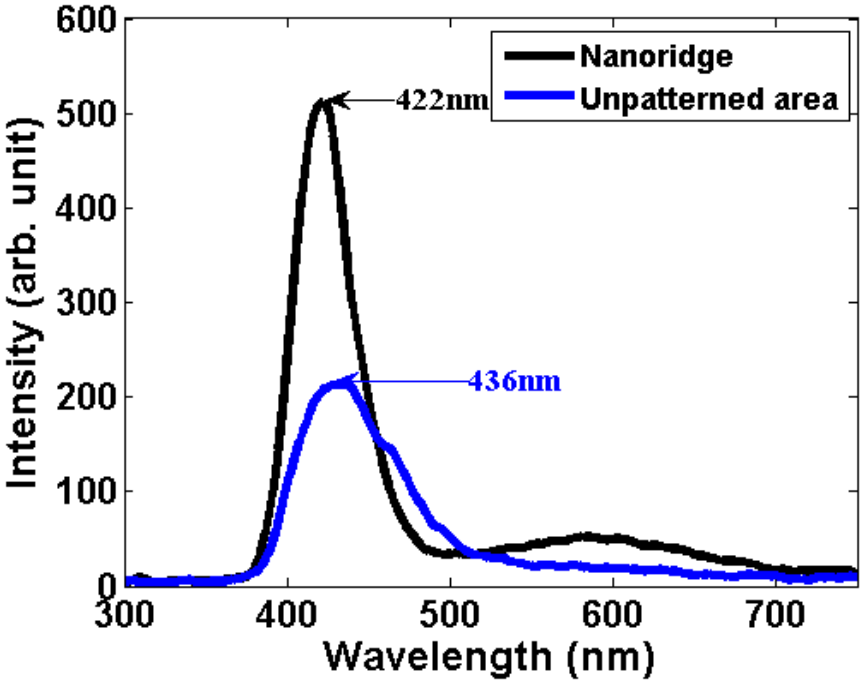

Figure 56: Room temperature CL spectra of InGaN/GaN MQWs grown on the nanoridges and on the unpatterned area. The InGaN MQWs grown on the nanostructure show higher CL intensity and ∼14 nm blueshift of luminescence peak wavelength from the MQWs grown on the unpatterned area.

analytical diffraction studies of GaN nanostructures. We found that the magnitudes of planar tilt and c-axis relaxation in heteroepitaxial growth increase with distance from the center of the free-standing structure, and that this dependence holds even on the nanoscale. We note that the tilted planes are less strained than the untilted planes, suggesting that the strain relaxation occurs in these tilted planes.

Nanodots, nanowires, and semi-polar quantum well structures of GaN-based material have been grown by NSAG. The structural and optical properties of these nanostructures have been investigated. The nanostructures grown by NSAG are found to be free of threading dislocations. The growth is very uniform with sharp interfaces between layers. The nanodots/nanowires are very homogeneous in size. InGaN MQWs grown on the nanostructure show enhanced CL emission as compared to the planar InGaN MQWs grown in the unpatterned area. The Al mole fraction at the apex of

the nanostructure and the Indium mole fraction at the intersection of growth planes are higher than those for the respective field layers.

CHAPTER V

GROWTH AND FABRICATION OF III-NITRIDE LIGHT EMITTING DIODES

5.1 Introduction

Recently, the development of group III-nitrides has played an important role in high brightness light emitting diodes. Solid state lighting offers many advantages over the conventional incandescent technology. For example, LEDs consume only about 10% of the power for the same luminous flux required by their incandescent counterparts. Moreover, LEDs have much longer lifetime compared to incandescent counterparts, lasting ten of thousands of hours, compared to 2000 for the latter. The higher efficiency and longer lifetime of LEDs result in less energy consumption and less waste.

While there have been many advancements made in LEDs operating in the blue and violet spectral range, there is still much room for improvement in quantum efficiency for LEDs operating in the UV and visible green spectral range. There are two main approaches for improving LED efficiency: the first is increasing the internal quantum efficiency, and the second is increasing the external quantum efficiency. The former is determined by crystal quality, epitaxial layer structure, as well as the spontaneous polarization and the piezoelectric polarization produced by the strain in the non-lattice matched heterostructure, while the latter is determined by the light extraction efficiency.

In this chapter, we utilize a new growth technique, NSAG, to realize a low dislocation density epitaxial layer structure and a low piezoelectric polarization by growing on semi-polar GaN facets. Furthermore, the pyramidal-shaped nanostructures grown by NSAG can also enhance the light extraction efficiency.

5.2 Epitaxial Growth Development and Characterization

For a comparative study, a nano-diode is grown simultaneously with a control LED. As its name implies, the nano-diode is fabricated from nanostructures grown by NSAG, while the control LED is fabricated from unpatterned areas. The basic epitaxial structure of a III-nitride LED consists of a n-contact layer, two undoped GaN layers, five periods of InGaN/GaN (5nm/10nm) MQW active region, and a p-contact layer. The nano-diode structure has an additional transparent induced tin oxide (ITO) layer, which serves as p-contact layer. Figures 57 and 58 show the epitaxial structure for the control LED and the nano-diode, respectively.

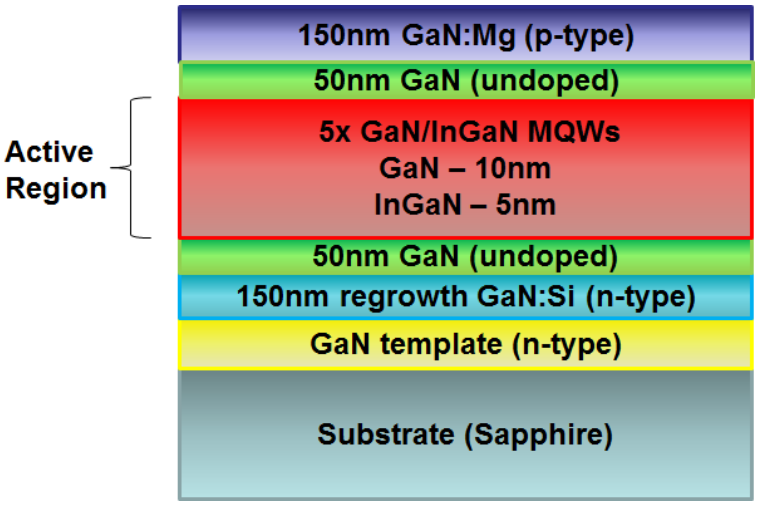

Figure 57: Epitaxial structure of a *p-i-n* GaN-based light emitting diode (control LED).

The epitaxial layers of nano-diode and control LED structures are grown on a 3.5 μm c-axis (0001) GaN/Al_2O_3 template by MOVPE in a T-shaped reactor. Trimethylgallium, trimethylindium, bis-cyclopentadienyl magnesium (Cp_2Mg), silane (SiH_4), and ammonia are used as precursors for Ga, In, Mg, Si, and N elements, respectively. Hydrogen is used as carrier gas in the entire epitaxial growth except during the growth of InGaN/GaN active layers, in which nitrogen is used. Prior to the growth of LED structures, a 100 x 100 μm^2 and 200 x 200 μm^2 SiO_2 dielectric mask with a thickness

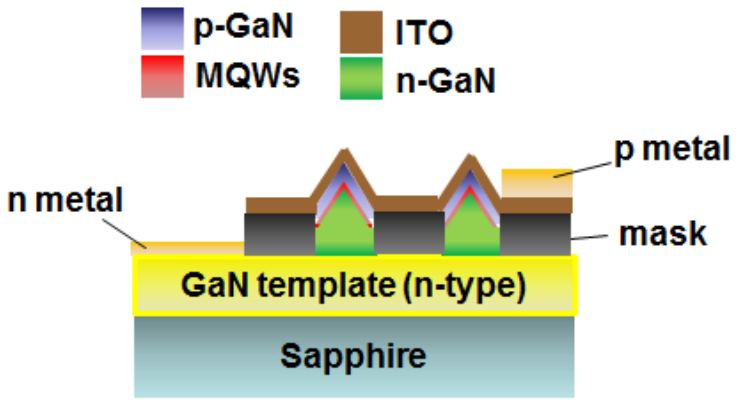

Figure 58: Epitaxial structure of a *p-i-n* GaN-based nano-diode.

of 100 nm is deposited on the substrate. The dielectric mask are processed by e-beam lithography to realize nanostripe openings of 0.12 x 98 μm^2 or 0.12 x 98 μm^2.

Standard experiments start with a heat ramp up to 1000°C, corresponding to step (a) in the reflectivity recoding (Figure 59). A 150 nm layerof n-doped GaN and subsequently a 50 nm layer of undoped GaN quantum barrier are deposited (b). The deposition of GaN is then stopped, and the temperature is decreased down to 800°C (c). When the temperature is stable at 800°C, five periods of InGaN/GaN MQWs are deposited (d). Afterwards, the growth is stopped again, and the temperature is ramped up to 1000°C (e). The epitaxial growth of 50 nm of undoped GaN and 150 nm of p-doped GaN are allowed to proceed (f). The period of the oscillation of the reflectivity can be used to monitor the epitaxial thickness. The reflectivity signal shows undamped oscillations (Figure 59, step f) with a periodicity of 43 mins (corresponding to a growth rate of 195 nm/h). Should the growth be inhomogeneous, the reflectivity will decrease, resulting a damped oscillation. The *in-situ* reflectivity shows that the growth mode is 2D in nature.

Hall-effect measurements carried out at room temperature reveal a hole concentration of $\sim$1x10^{17} cm^{-3} with a mobility of $\sim$3.54 cm^2/Vs for a p-GaN:Mg layer grown at 1000°C in hydrogen ambient, while an electron concentration of $\sim$1x10^{18} cm^{-3}

with a mobility of $\sim$70cm^2/Vs is achieved for a n-GaN:Si layer grown at 1000°C in hydrogen ambient.

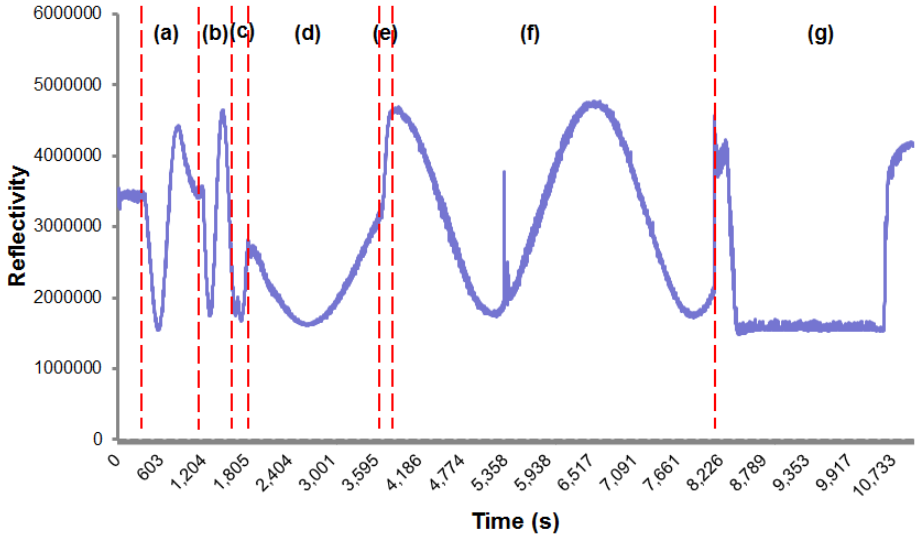

Figure 59: *In-situ* reflectance measurement during *p-i-n* GaN based LED growth on GaN template.

To promote a 2D growth mode, hydrogen is used as a carrier gas. Figure 60 shows the AFM and SEM images of a control LED revealing atomic steps on the surface with no visible nano-pits. The AFM images show an atomically smooth surface with no visible nano-pits, demonstrating the superior material quality of GaN epitaxial layers after switching the carrier gas from N_2 to H_2. Root-mean square (RMS) surface roughness values are approximately 0.5 nm for 10 x 10 μm^2 scans.

Figure 61 shows SEM images of a nano-diode structure grown on a 100 x 100 μm^2 patterned dielectric mask. It can be seen that nanoridges grown in the center of the nano-diode are well-shaped and completely fill the mask openings. In contrast, the growth of nanoridges at the edges of the nano-diode are inhomogeneous, and they do not completely fill the mask openings. We attribute this phenomenon to lateral diffusion and surface migration of the reactive species during the MOVPE process. These unfilled mask openings are the cause of undesirable leakage current, which will be discussed later.

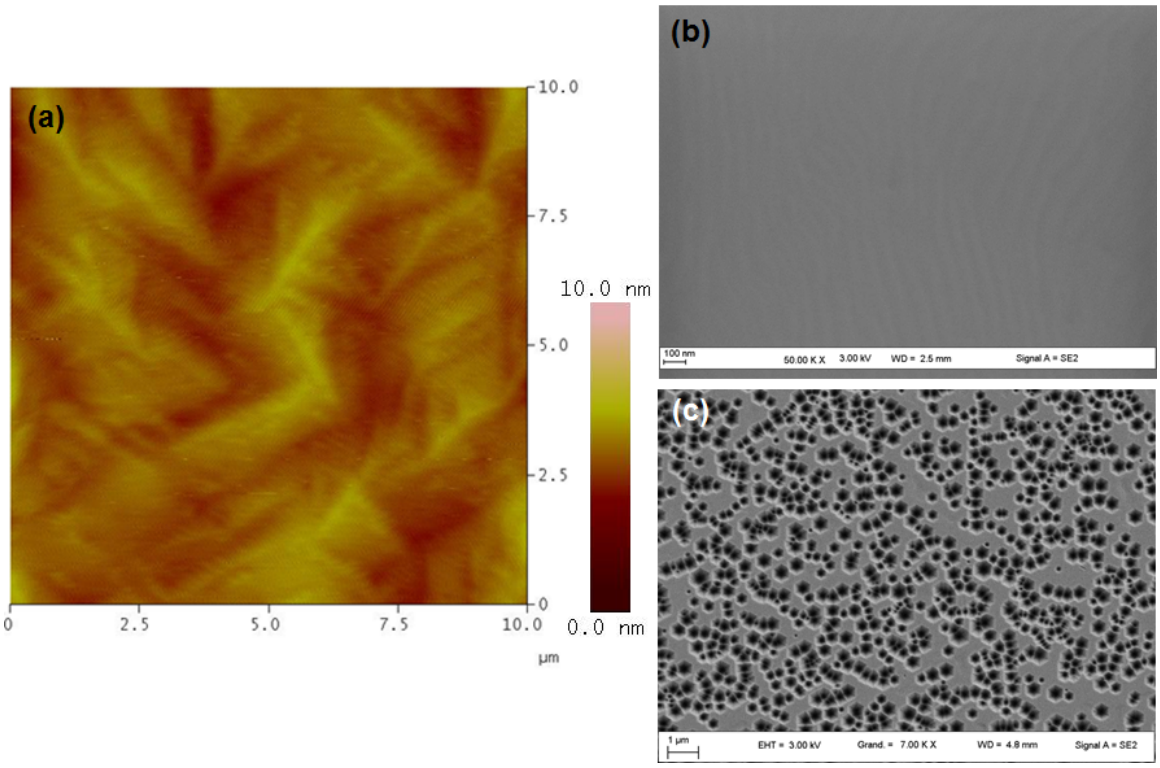

Figure 60: (a) AFM image of a LED structure grown with H_2 carrier gas. (b) SEM image of a LED structure grown with H_2 carrier gas. (c) SEM image of a LED structure grown with N_2 carrier gas. The pit density and surface roughness are reduced significantly by switching from N_2 to H_2 carrier gas.

The crystalline quality of the control LED epitaxial layers is analyzed using a high-resolution X-ray diffractometer. Figure 62 shows the ω scans of GaN and InGaN peaks at (00.4). The full width at half maximum (FWHM) line widths of the GaN and InGaN peaks are 292 and 312 arcsec, respectively. These results are comparable to those of InGaN/GaN MQWs p-i-n structures grown on GaN/sapphire substrates.

Figure 63 shows the $\omega/2\theta$ scan at (00.2) and (00.4). The blue curves represent experimental results while the red curves represent simulated fit results. The simulation shows about 6% Indium incorporation at the MQWs and that the well and barrier thicknesses are 4.5 and 8.8 nm, respectively. Note that the intended well and barrier thicknesses are 5 and 10 nm, respectively. All the simulated results are obtained by using X'Pert Epitaxy software.

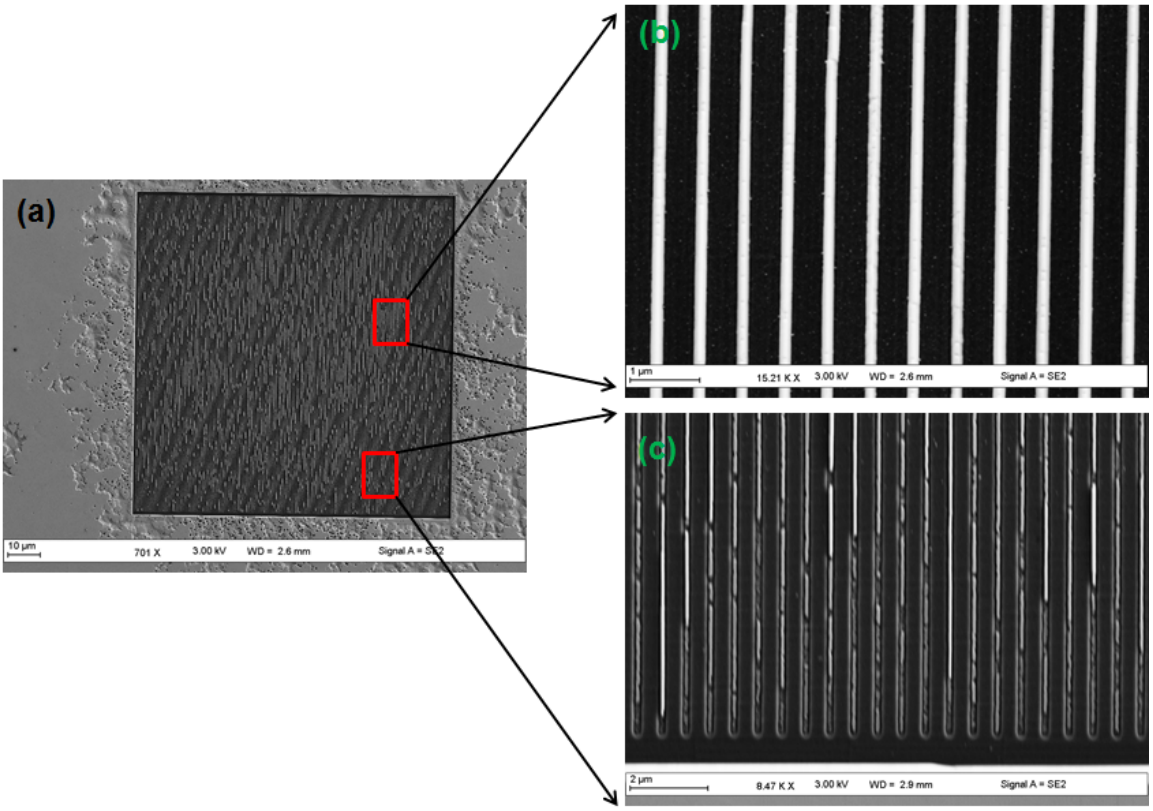

Figure 61: (a) SEM image of a nano-diode structure. (b) Magnified SEM image in the center of the nano-diode showing well-shaped nanoridges. (c) Magnified SEM image at the edges of the nano-diode showing unfilled mask openings.

Figure 64 shows the room temperature CL spectra of a nano-diode at various electron accelerating voltage. It should be noted that the CL peak does not change with the electron accelerating voltage. The intensity of the InGaN peak is much stronger compared to that for yellow band, indicating a better optical quality of the InGaN MQWs. The CL peak from the GaN template appears at high accelerating voltage due to increased depth of penetration.

Figure 65 shows the room temperature CL spectra of a nano-diode and the control LED. The band-edge CL intensity of the nano-diode is much stronger compared to that for the control LED due to a reduction of the overall defect density, which has been explained in the previous chapter. The higher CL intensity of the nano-diode can also be attributed to the random scattering of the emitted light in nanostructures,

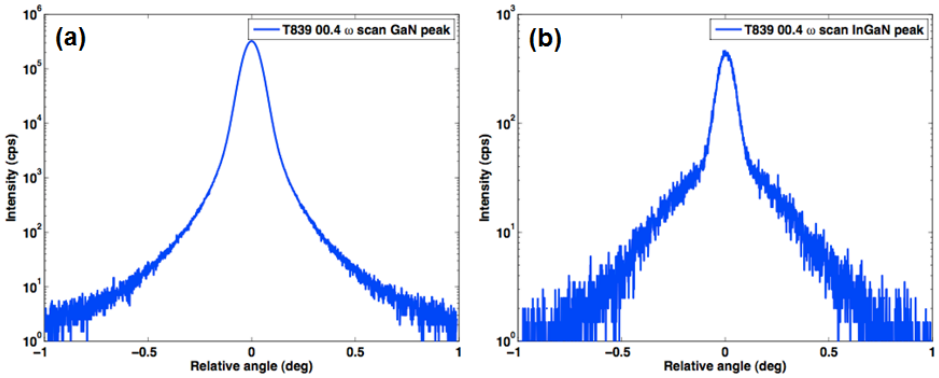

Figure 62: (a) ω scan of GaN peak at (00.4). (b) ω scan of InGaN peak at (00.4). The FWHM of GaN and InGaN peaks are 292 and 312 arcsec, respectively.

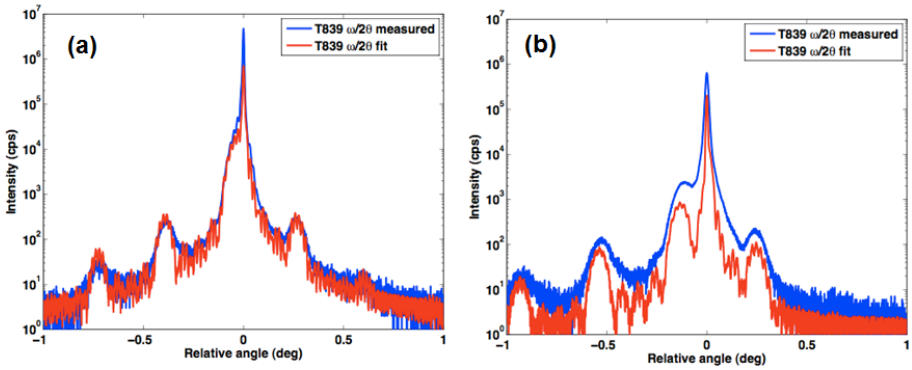

Figure 63: (a) $\omega/2\theta$ scan at (00.2). (b) $\omega/2\theta$ scan at (00.4). The blue curves represent experimental results while the red curves represent simulated fit results. The simulation shows about 6% Indium incorporation at the MQWs.

which can enhance the light extration efficiency of a LED. The directions of the propagation of light can be changed from regular to random, and reflected multiple times before being absorbed by the substrate, leading to the enhancement of light extraction. The InGaN peak of the nano-diode and control LED are 413 and 396 nm, respectively. We believe this phenomenon is caused by the difference in Indium incorporation between c-plane GaN template and semi-polar plane GaN nanoridges.

The fabrication procedure of the *p-i-n* junction LED of the nano-diode is described below in detail. The device processing is done by Dr. Martinez from the Laboratory

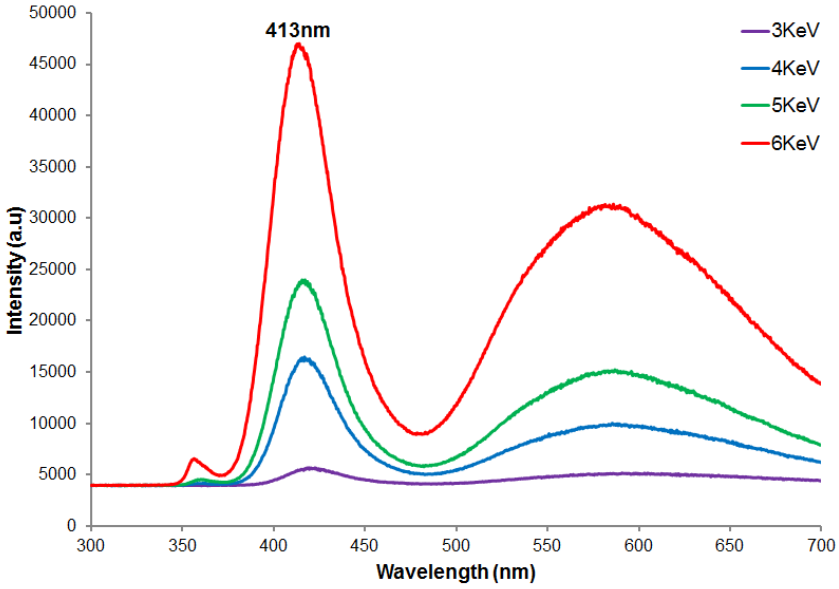

Figure 64: Room temperature CL spectra of nano-diode at various electron accelerating voltage. Note that the CL peak does not change with the electron accelerating voltage.

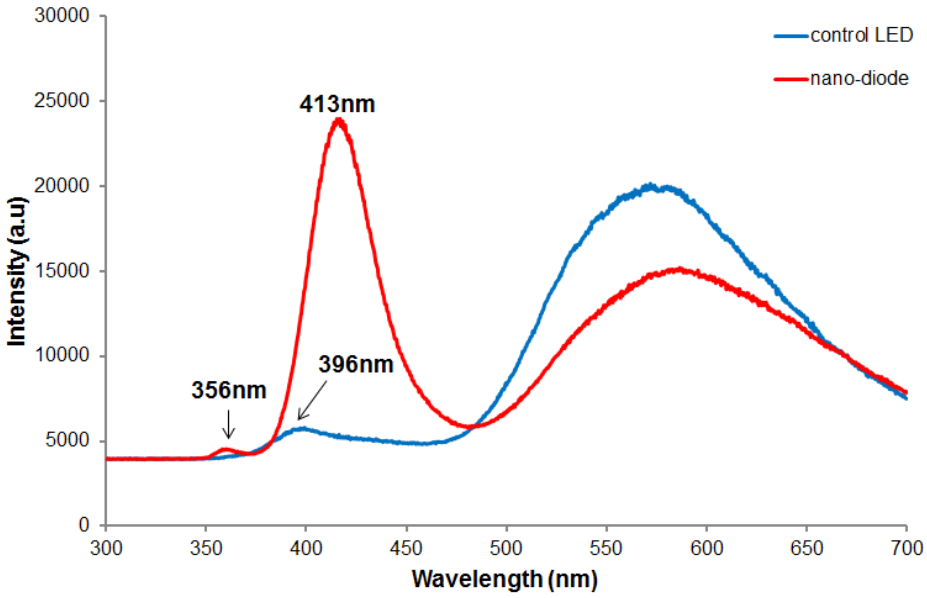

Figure 65: Room temperature CL spectra of nano-diode and control LED. The nano-diode shows enhanced CL emission as compared to the control LED, which is grown on the unpatterned area.

for Photonics and Nanostructures [1]. Prior to processing, all the samples are cleaned in acetone, ethanol and DI water for 10 minutes each in an ultrasonic bath. Then the wafers are taken into the cleanroom to be processed by the following procedure:

- definition of square mesa on the top of matrices using photoresist
- dry etching of samples, controlled to a depth of 630 nm
- definition of openings using photolithography for n-contact evaporation
- n-contact evaporation (Ti/Al/Au) followed by rapid thermal annealing
- definition of openings in photoresist on the top of matrices
- induced tin oxide (ITO) evaporation: 50 nm
- definition of openings by photolithography
- p-contact evaporation (Cr/Ni/Au) followed by rapid thermal annealing

Nano-diodes are processed into 100 x 100 μm^2 and 200 x 200 μm^2 square mesas by inductively coupled plasma etching using a Cl_2/He carrier gas mixture. An optical image of a fabricated 100 x 100 μm^2 mesa device with contact probe pad is shown in Figure 66. A 50 nm thick ITO layer is evaporated on top of the p-layer to serve as a transparent p-contact. Ti/Al/Au and Cr/Ni/Au Ohmic contacts are evaporated on the n-layer and ITO-layer respectively, and annealed at 600°C in a N_2 ambient.

In contrast, the control LEDs are processed and tested differently. The Indium contact is deposited on the n-layer, which is exposed using a diamond knife. Furthermore, the control LEDs are tested without a p-contact probe pad.

[1]Laboratory for Photonics and Nanostructures, CNRS 20 Route de Nozay Marcoussis 91460 France

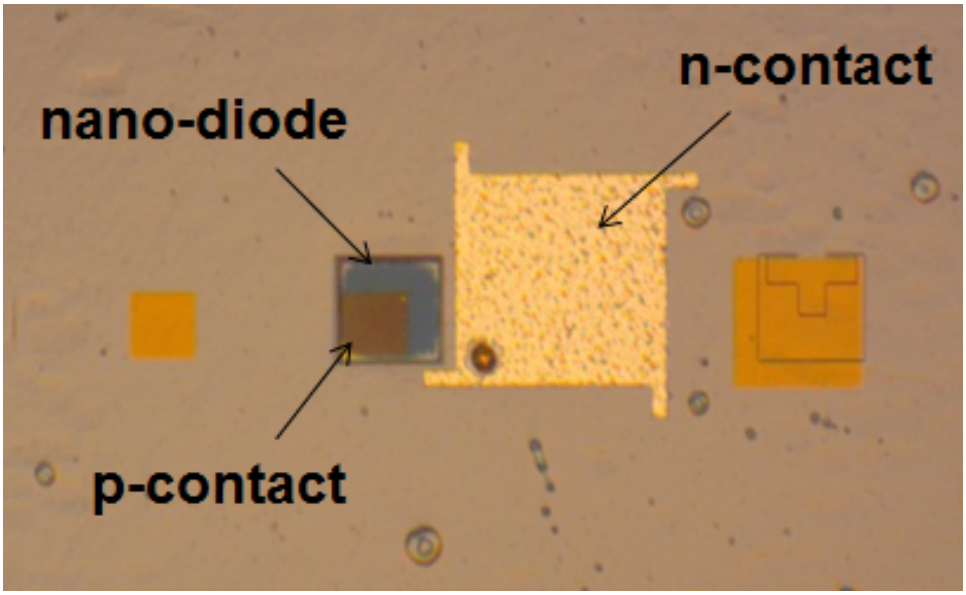

Figure 66: Optical image of a fabricated 100 x 100 μm^2 GaN/InGaN *p-i-n* nano-diode with control probe pad.

5.3 Light Emitting Diode Device Data

Figure 67 shows the I-V curve of a control LED. The diode ideality factor and series resistance extracted from the I-V curve are n=4.5 and R_S~10kΩ, respectively. A high diode ideality factor results in a high forward voltage, and thus a low power efficiency. However, it is commonly reported that III-nitride devices can have diode ideality factors as high as 5-7 [68, 69]. The high series resistance, R_S, can be attributed to the combined effect of the absence of p-contact layer, non-optimized n-contact layer, as well as a relative low hole concentration (~1x10^{17} cm^{-3}). The leakage current is measured to be 8 x 10^{-8}A at 0V and 7 x 10^{-6}A at -10V.

The electroluminescence (EL) spectrum of the control LED in Figure 68 shows that the peak emission wavelength remained at ~390 nm despite the increase of the injection current from 10 mA to 35 mA. This constant peak emission wavelength results are dissimilar to the results in InGaN SQW LED structures reported by others [70]. They reported a blue-shift of peak emission wavelength with increasing driving current, due to the combined effects of coulomb screening of the piezoelectric field in

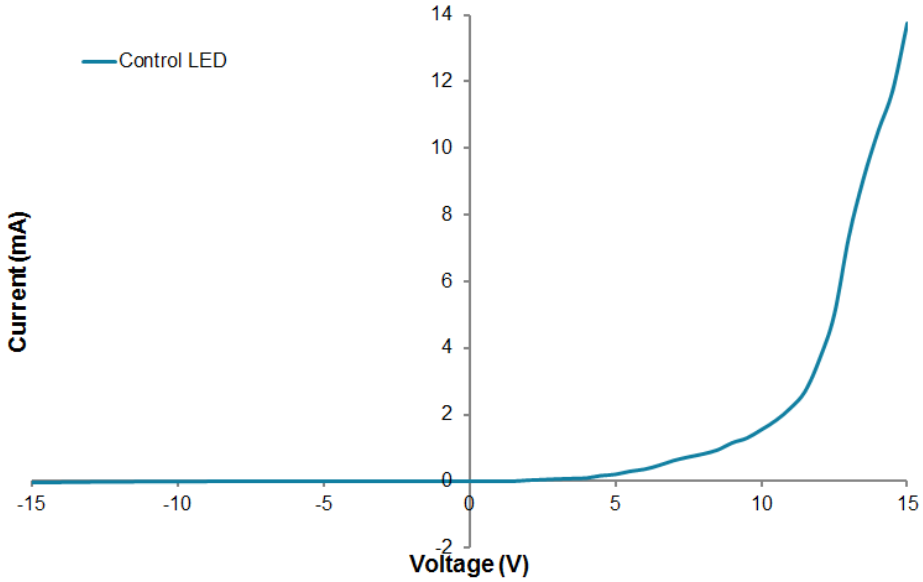

Figure 67: The I-V curve for the control LED.

reduced band bending [16, 73], and band-filling of the energy tail states [71]. The constant peak emission in our control LED can be attributed to a low In concentration (∼6%), which lead to a low piezoelectric field in the structure. The inset of Figure 68 illustrates the emission from the device at an injection current of 10 mA.

The I-V curve of the nano-diode shown in Figure 69 reveals a non-ideal diode characteristic. The leakage current is measured to be as high as 6 x 10^{-5}A at 0V and 7 x 10^{-2}A at -2V. This abnormally high leakage current is believed to be caused by suboptimal device structure as explained in the following. The SEM image of the nano-diode shown in Figure 61 reveals an inhomogeneous growth of nanostructures in the mask openings. As a result, some of the mask openings are not completely filled by the nanostructures. These unfilled mask openings could serve as short-circuit routes in the nano-diode structure, and hence, lead to a high leakage current. In addition to suboptimal device structure, unoptimized device processing may also contribute to high leakage current. This hypothesis is supported by the absence of emission signal in the EL characterization. Further studies of device design optimization for nano-diodes will be performed.

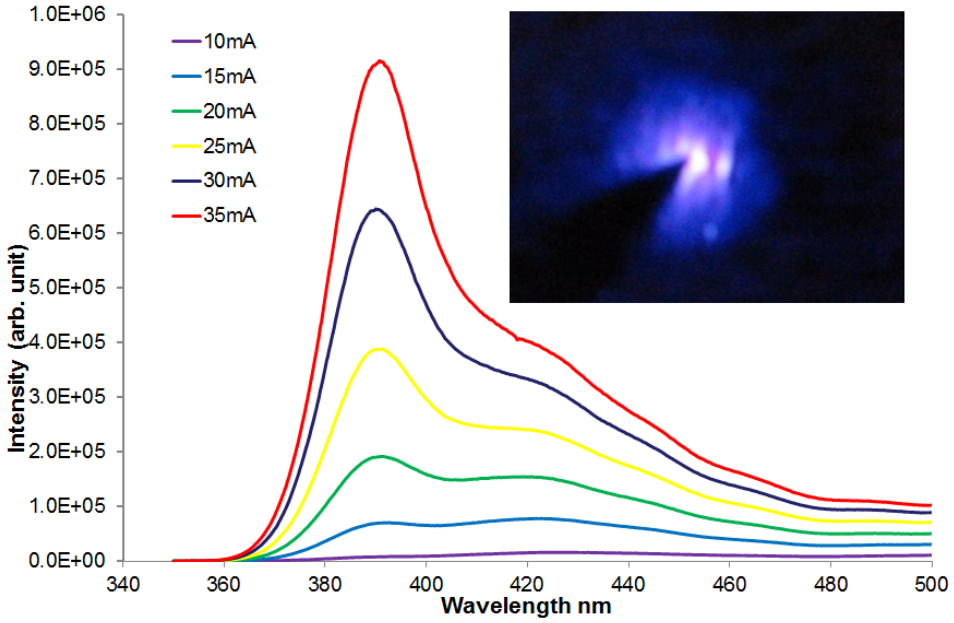

Figure 68: The EL spectra of the control LED at various injection currents. Inset shows the emission at an injection current of 10 mA during testing.

5.4 Summary

In this chapter, we have attempted to grow and fabricate NSAG grown light emitting diodes and nano-diodes with emission spectra in the UV wavelength range. First, we have compared the effects of hydrogen and nitrogen as carrier gases on the surface morphology. We have shown that by using hydrogen as a carrier gas, the pit density and surface roughness of the LEDs can be reduced significantly.

Second, we have investigated the structural and optical properties of the epitaxial layers by using XRD and CL, respectively. The XRD results show that we have about 6% Indium incorporation which is corroborated by CL measurement. The CL measurements show that the band-edge intensity of the nano-diode is much stronger compared to that for the control LED. This phenomenon is attributed to reduction of the overall defect density and increase of light extraction.

Finally, we have grown, fabricated and characterized LEDs emitting at ~390 nm. The diode ideality factor and series resistance for the control LED are n=4.5 and

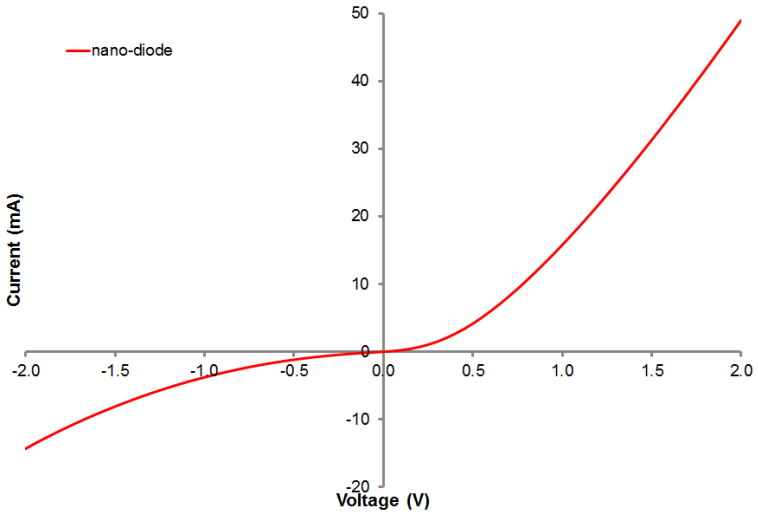

Figure 69: The I-V curve for the nano-diode.

R_S~10kΩ, respectively. Unfortunately, the nano-diode fabricated suffers from high leakage current and does not exhibit electroluminescence.

CHAPTER VI

CONCLUSIONS AND FUTURE WORK

This work demonstrates a new technology to grow high quality GaN based material by nano selective area growth. The motivation is to overcome the limits of the conventional growth method, which yields a high density of dislocations in the epitaxial layer. A low dislocation density in the epitaxial layer is crucial for high performance and high efficiency devices. The realization of an efficient device still requires a deeper understanding and optimization of the parameters controlling the material growth and an optimization of the electrical contacts.

This work focuses on growth and material characterization of GaN-based nanostructures (nanodots and nanostripes) grown using NSAG. NSAG, with a precise control of diameter and position of nanostructures, opens the door to new applications such as: 1) single photon sources, 2) photonic crystals, 3) coalescence of high quality GaN templates, and 4) novel nanodevices.

The preliminary work begins with optimization of the growth conditions for GaN structures at the micrometer scale. A perfect selectivity on the SiO_2 masks has been obtained for mask widths less than or equal to 60 μm. The AFM shows a ribbon-shaped GaN growth between the masks with smooth vertical facets and a smooth surface with rms roughness of 0.4 nm. The growth rate enhancement ratio varies linearly with the mask width, Wm, and decreases with increase of the mask opening, Wo. By fitting the simulated VPD model to the experimental results, the ratio of diffusion length, D/k is empirically determined to be 13 μm..

The optimized growth condition for micro-SAG is applied to grow nanostructures

on both lattice matched as well as highly lattice mismatched (SiC and AlN) substrates. A perfect selectivity growth of the GaN has been obtained. The nanodots and nanostripes have excellent surface morphology with very smooth surface side walls. We demonstrated that our technique allows the growth of nanostripes along any in-plane crystallographic direction without any influence from the step bunching effect that occurs on the planar substrate. By varying the reactor pressure, growth of isolated nanostructures or epitaxial lateral overgrowth structures can be obtained. The lateral overgrowth nanostripes are almost completely relaxed, while the confined nanostripes are more relaxed than the GaN thin films grown on planar substrates.

Synchrotron-based XRD has been used to study the GaN nanostructures. We found that the magnitudes of planar tilt and c-axis relaxation in heteroepitaxial growth increase with distance from the center of the free-standing structure, and that this dependence holds even on the nanoscale. The tilted planes are less strained than the untilted planes, suggesting that the strain relaxation occurs in these tilted planes.

Nanodots, nanowires, and semi-polar quantum well structures of GaN-based material have been grown by NSAG. The structural and optical properties of these nanostructures have been investigated. The nanostructures grown by NSAG are found to be free of threading dislocations. The growth is very uniform with sharp interfaces between layers. The nanodots/nanowires are very homogeneous in size. InGaN MQWs grown on the nanostructure show enhanced CL emission as compared to the planar InGaN MQWs grown in the unpatterned area. The Al mole fraction at the apex of the nanostructure and the Indium mole fraction at the intersection of growth planes are higher than those for the respective field layers.

Finally, we have attempted to fabricate light emitting diodes and nano-diodes with emission spectra in UV wavelength range. The control LED emits an electroluminescence at $\sim$390 nm. The diode ideality factor and series resistance for the control

LED are n=4.5 and R_S∼10kΩ, respectively. Unfortunately, the fabricated nano-diode suffers from high leakage current and does not exhibit electroluminescence.

As part of the future work, we would like to first propose the use of nanoimprint lithography to fabricate nanometer scale patterns. It offers many advantages over the e-beam lithography technology, such as low cost and high throughput. Secondly, we would like to optimize the growth conditions and modify the mask design to obtain homogenous growth. To avoid unfilled mask openings in the edges, we can reduce the lateral diffusion effects by increasing the distance between the mask openings and the mask edges. Thirdly, we would like to modify the device structure of the LEDs to improve the efficiency. To increase the external quantum efficiency, we can engineer the layout of the nanostructures to form photonic crystals, which can improve the light extraction. Finally, we should apply NSAG to grow device structures for different applications, such as high electron mobility transistors, single photon emitters, solar cells etc.

REFERENCES

[1] I. Vurgaftman and J. R. Meyer. J. Appl. Phys. 94(3675), 2003.

[2] L. P. Yu, J. Y. Shi, Y. Z. Wang, H. Zhang. Journal of Crystal Growth 268(484), 2004.

[3] R. People and J. C. Bean. Appl. Phys. Lett, 47(322), 1985.

[4] R. People and J. C. Bean. Appl. Phys. Lett, 49(229), 1986.

[5] P. Ruterana and G. Nouet Phys. Stat. Sol. B 227(177), 2001.

[6] P. Vennegues, B. Beaumont, S. Haffouz, M. Vaille, and P. Gibart. J. Cryst. Growth 187(167), 1998.

[7] E. Frayssinet, B. Beaumont, J. P. Faurie, P. Gibart, Zs. Makkai, B. Pecz, P. Lefebvre, and P. Valvin. MRS Int. J. Nitride Semicond. Res. 7(8), 2002.

[8] S. Tanaka, M. Takeuchi, and Y. Aoyagi. Jpn. J. Appl. Phys. Part 2 39(L831), 2000.

[9] K. Cheng, M. Leys, S. Degroote, M. Germain, and G. Borghs. Appl. Phys. Lett. 92(192111), 2008.

[10] Y. Kato, S. Kitamura, K. Hiramatsu, and N. Sawaki. J. Cryst. Growth 144(133), 1994.

[11] H. Volterra. Laser Focus World 38(64), 2002.

[12] M. Gibbon, J. P. Stags, C. G. Cureton, E. J. Thrush, C. J. Jones, R. E. Mallard, R. E. Pritchards, N. Collis, and A. Chew. Semicond. Sci. Technol. 8(998), 1993.

[13] S. Kitamura, K. Hiramatsu, and N. Sawaki. Jpn. J. Appl. Phys. 34(L1184), 1995.

[14] H. Miyake, K. Nakao, and K. Hiramatsu. Superlattices and Microstructures 41(341), 2007.

[15] T. Akasaka, Y. Kobayashi, S. Ando, N. Kobayashi, and M. Kumagai. J. Cryst. Growth 72(189), 1998.

[16] T. Akasaka, Y. Kobayashi, S. Ando, and N. Kobayashi. Appl. Phys. Lett. 71(2196), 1997.

[17] H. Watanabe, N. Kuroda, H Sunakawa, and A. Usui. Appl. Phys. Lett. 77(1786), 2000.

[18] S. Nakamura, M. Senoh, S. Nagahama, N. Iwasa, T. Yamada, T. Matsushita, H. Kiyoku, Y. Sugimoto, T. Kozaki, H. Umemoto, M. Sano, and K. Chocho. J. Cryst. Growth 189/190(820), 1998.

[19] D. Kapolnek, S. Keller, R. Vetury, R. D. Underwood, P. Kozodoy, S. P. Denbaars, and U. K. Mishra. Appl. Phys. Lett. 71(1204), 1997.

[20] H. O. Nam, M. D. Bremser, T. S. Zheleva, and R. F. Davis. Appl. Phys. Lett. 71(2638), 1997.

[21] A. Sakai, H. Sunakawa, and A. Usui. Appl. Phys. Lett. 71(2259), 1997.

[22] Z. Yu, M. A. L. Johnson, J. D. Brown, N. A. El-Masrys, J. F. Muth, J. W. Cook, J. F. Schetzina, K. W. Haberern, H. S. Kong, and J. A. Edmond. MRS Int. J. Nitride Semicond. Res. 4S1(G4.3), 1999.

[23] K. Hiramatsu, K. Nishiyama, A. Motogaito, H. Miyake, Y. Iyechika, and T. Maeda. Phys. Stat. Sol. A 176(535), 1999.

[24] S. Luryi and E. Suhir. Appl. Phys. Lett. 49(140), 1986.

[25] D. Zubia, S. H. Zaidi, S. R. J. Brueck, and S. D. Hersee. Appl. Phys. Lett. 76(858), 2000.

[26] X. Wang, X. Sun, M. Fairchild, and S. D. Hersee. Appl. Phys. Lett. 89(233115), 2006.

[27] S. D. Hersee, M. Fairchild, A. K. Rishinaramangalam, M. S. Ferdous, L. Zhang, P. M. Varangis, B. S. Swartzentruber, and A. A. Talin. Elec. Lett. 45(1), 2009.

[28] K. Y. Zang, Y. D. Wang, S. J. Chua, L. S. Wang, and S. Tripathy. Appl. Phys. Lett. 88(141925), 2006.

[29] A. Y. Cho and J. R. Arthur. Prog. Sol. Sta. Chem. 10(157), 1975.

[30] H. Manasevit. Appl. Phys. Lett. 12(156), 1968.

[31] A. Mircea, A. Ougazzaden, and R. Mellet. Prog. Cryst. Growth Charact. 19(39), 1989.

[32] Available at http://www.purdue.edu/rem/rs/sem.htm (01/2012)

[33] Available at http://www.hk-phy.org/ (01/2012)

[34] C. Kittle, Kittle. Introduction to Solid State Physics. New Jersey: John Wiley and Sons, Inc., 2005.

[35] C. Khulbe and T. Matsuura. Synthetic Polymeric Membranes Characterization by Atomic Force Microscopy. Berlin: Springer, 2008.

[36] V. Holy, U. Pietsch, and T. Baumbach. High-resolution X-ray Scattering from Thin Films and Multilayers. 3-16(149), 1999.

[37] M. A. Moram and M. E. Vickers. Rep. Prog. Phys. 1(72), 2009.

[38] P. F. Fewster. X-Ray Scattering from Semiconductors 2nd edn, 2003.

[39] D. K. Bowen and Tanner B K. High Resolution X-Ray Diffractometry and Topography, 1998.

[40] M. Schuster, P. O. Gervais, B. Jobst, W. Hosler, R. Averbeck, H. Riechert, A. Iberl, and R. Stommer. J. Phys. D: Appl. Phys. A56(32), 1999.

[41] M. E. Coltrin, C. C. Willan, M. E. Bartram, J. Han, N. Missert, M. H. Crawford, and A. G. Baca. MRS Internet J. Nitride Semicond. Res. 4S1(G6.9), 1999.

[42] M. E. Coltrin and C. C. Mitchell. J. Cryst. Growth 254(35), 2003.

[43] A. A. Sirenko, A. Kazimirov, R. Huang, D.H. Bilderback, S. O'Malley, V. Gupta, K. Bacher, L. J. P. Ketelsen, and A. Ougazzaden. J. Appl. Phys. 97(63512), 2005.

[44] J. Martin, A. Martinez, W. H. Goh, S. Gautier, N. Dupuis, L. Le Gratiet, J. Decobert, A. Ramdane, N. Maloufi, and A. Ougazzaden. Mater. Sci. Eng. B. 147(114), 2007.

[45] K. Hiramatsu, S. Kitamura, and N. Sawaki. MRS Symp. Proc. 395(267), 1996.

[46] W. H. Goh, J. Martin, S. Ould-Saad, S. Gautier, A.A. Sirenko, A. Martinez, L. Le Gratiet, A. Ramdane, N. Maloufi, and A. Ougazzaden. Phys. Status Solidi C 6(S510), 2009.

[47] T. Van Caenegem, I. Moerman, and P. Demeester. Prog. Cryst. Growth Charact. Mater. 35(263), 1997.

[48] F. R. Chien, X. J. Ning, S. Stemmer, P. Pirouz, M. D. Bremser, and R. F. Davis. Appl. Phys. Lett. 68(2678), 1996.

[49] J. K. Jeong, J.-H. Choi, H. J. Kim, H.-C. Seo, H. J. Kim, E. Yoon, C. S. Hwang, and H. J. Kim. J. Cryst. Growth 276(407), 2005.

[50] A. R. Goni, H. Siegle, K. Syassen, C. Thomsen, and J.-M. Wagner. Phys. Rev. B 64(035205), 2001.

[51] C. Kiesielowski, J. Kruger, S. Ruvimov, T. Suski, J. W. Ager, E. Jones, Z. Liliental, M. Rubin, and E. R. Weber. Phys. Rev. B 54(17745), 1996.

[52] A. A. Sirenko, A. Kazimirov, A. Ougazzaden, S. O'Malley, D. H. Bilderback, Z.-H. Cai, B. Lai, R. Huang, V. Gupta, M. Chien, and S.N.G. Chu. Appl. Phys. Lett. 88(081111), 2006.

[53] P. L. Bonanno, S. M. O'Malley, A. A. Sirenko, A. Kazimirov, Z.-H. Cai, T. Wunderer, P. Brckner, and F. Scholz. Appl. Phys. Lett. 92(123106), 2008.

[54] M. Hanke, M. Dubslaff, M. Schmidbauer, T. Boeck, S. Schder, M. Burghammer, C. Riekel, J. Patommel, and C. G. Schroer. Appl. Phys. Lett. 92(193109), 2008.

[55] V. Darakchieva, B. Monemar, and A. Usui. Appl. Phys. Lett. 91(031911), 2007.

[56] R. B. Kukta and L. B. Freund. J. Mech. Phys. Solids, 45(1835), 1997.

[57] Y. Arakawa. IEEE J. Sel. Top. Quantum Electron. 8(823), 2002.

[58] D. Simeonov, E. Feltin, J.-F. Carlin, R. Butte, M. Ilegems, and N. Grandjean. J. Appl. Phys. 99(083509), 2006.

[59] K. Nishizuka, M. Funato, Y. Kawakami, Sg. Fujita, Y. Narukawa, and T. Mukai. Appl. Phys. Lett. 85(3122), 2004.

[60] B. Neubert, P. Bruckner, F. Habel, F. Scholz, T. Riemann, J. Christen, M. Beer, and J. Zweck. Appl. Phys. Lett. 87(182111), 2005.

[61] R. Waltereit, O. Brandt, A. Trampert, H. T. Grahn, J. Menniger, M. Ramsteiner, M. Reiche, and K. H. Ploog. Nature 406(865), 2000.

[62] N. Akopian, G. Bahir, D. Gershoni, M. D. Craven, J. S. Speck, and S. P. DenBaars. Appl. Phys. Lett. 86(202104), 2005.

[63] K. Tachibana, T. Someya, S. Ishida, and Y. Arakawa, Phys. Stat. Sol. B 228(187), 2001.

[64] V. Perez-Solorzano. A. Groning, M. Jetter, T. Riemann, and J. Christen. Appl. Phys. Lett. 87(163121), 2005.

[65] M. Feneberg, F. Lipski, R. Sauer, K. Thonke, T.Wunderer, B. Neubert, P. Brückner, and F. Scholz. Appl. Phys. Lett. 89(171921), 2006.

[66] M. Funato, T. Kotani, T. Kondou, and Y. Kawakami, Y. Narukawa, and T. Mukai. Appl. Phys. Lett. 88(261920), 2006.

[67] Q. Li and G. T. Wang. Nano. Lett. 10(1554), 2010.

[68] K. Mayes, A. Yasan, R. McClintock, D. Shiell, S. R. Darvish, P. Kung, and M. Razeghi. Appl. Phys. Lett. 84(1046), 2004.

[69] T. Li, D. J. H. Lambert, M. M. Wong, C. J. Collins, B. Yang, A. L. Beck, U. Chowdhury, R. D. Dupuis, and J. C. Campbell. IEEE J. Quantum Electron. 37(538), 2001.

[70] S. Nakamura and G. Fasol. The Blue Laser Diode, Heidelberg: Springer-Verlag. 1997.

[71] S. Chichibu, T. Azuhata, T. Sota, and S. Nakarnura. Appl. Phys. Lett. 69(4188), 1996.

[72] H. Amano, T. Takeuchi, S. Sota, H. Sakai, and I. Akasaki, Muter. Res. Soc. Symp. Proc. 449(1143), 1997.

[73] T. Takeuchl, S. Sota, M. Katsuragawa, M. Komori, H. Takeuchi, H. Amano, and I. Akasala, Jpn. J. Appl. Phys. 36(L382), 1997.